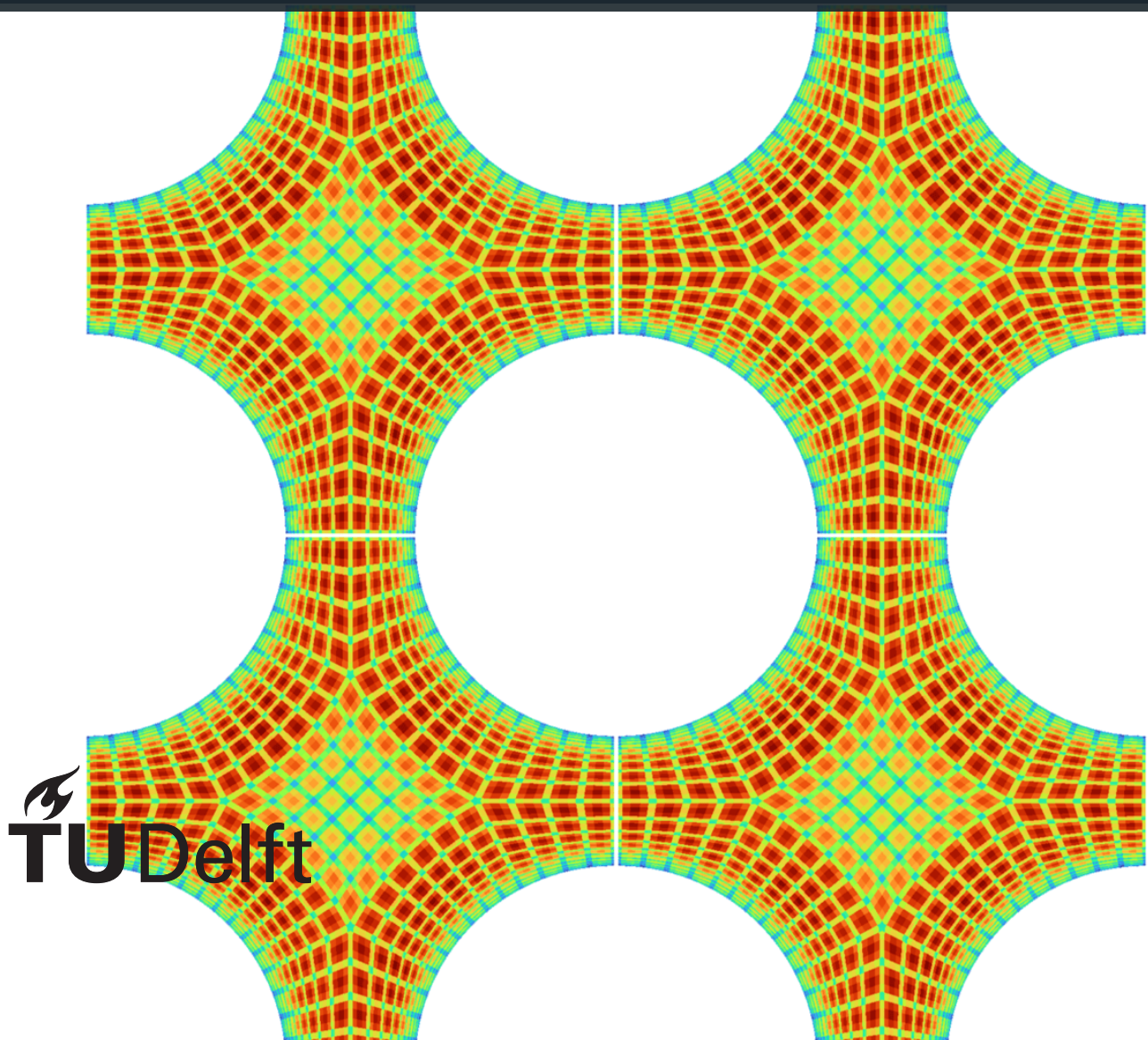


Investigation in flow and heat transport in pipe and PWR rod bundle geometries

A DNS investigation towards better engineering tools

Jacob Ashwin Abraham



<This page was intentionally left blank>

Investigation in flow and heat transport in pipe and PWR rod bundle geometries

A DNS investigation towards better engineering tools

Thesis report

by

Jacob Ashwin Abraham

to obtain the degree of Master of Science
at the Delft University of Technology
to be defended publicly on December 19th, 2024 at 14:00pm

Thesis committee:

Chair:	Dr. Alexander van Zuijlen (TU Delft)
Supervisors:	Dr. Marc Gerritsma (TU Delft) Dr. Akshat Mathur (NRG)
External examiner:	Dr. Deepesh Toshniwal (TU Delft)
Place:	Faculty of Aerospace Engineering, Delft
Project Duration:	March, 2024 - November, 2024
Student number:	5790042

An electronic version of this thesis is available at <http://repository.tudelft.nl/>.

Acknowledgements

The journey of my Master's thesis has been both challenging and rewarding, filled with moments of growth, learning, and perseverance. Reflecting on this transformative experience, I am deeply grateful to the many individuals and organizations who supported and guided me along the way.

First and foremost, I extend my heartfelt gratitude to NRG, where I had the privilege to conduct my research. I am particularly thankful to my daily supervisor, Dr. Akshat Mathur, for his unwavering support and constructive guidance. His open-minded and flexible approach allowed me to develop essential skills in time management and adaptability. Additionally, I acknowledge the PIONEER program for their generous funding and support, which made this research possible.

At TU Delft, I owe special thanks to my co-supervisor, Dr. Marc Gerritsma, for his invaluable mentorship and intellectual input throughout this process. Our regular meetings became a cornerstone of my thesis, where his theoretical insights and strategic advice helped me navigate complex challenges and approach problems from new perspectives. His encouragement during the initial, uncertain phases of my work was particularly impactful, inspiring me to remain focused and resilient.

Some difficulties arose during this journey, as running Direct Numerical Simulations (DNS) proved to be computationally expensive and time-consuming. Overcoming these challenges required patience, persistence, and the support of those around me. To my friends Sharan Pant, Sai Sharan Khandavilli, and Deepak Sogasu, thank you for your companionship, words of encouragement, and moments of joy that kept me grounded. I am also grateful to my childhood and bachelor friends, whose continued support and shared memories have been a source of positivity and strength.

Finally, to my parents and family, whose unconditional love, sacrifices, and prayers have always been my greatest source of strength: this achievement is as much yours as it is mine. Your belief in me has been a constant inspiration, and it is to you all that I dedicate this work with all my heart.

Jacob Ashwin Abraham
Alkmaar, December 2024



Copyright ©Jacob Ashwin Abraham, 2024
All rights reserved.

Abstract

This thesis investigates the flow and heat transport phenomena in a pipe and Pressurized Water Reactor (PWR) rod bundle geometries using high-fidelity Direct Numerical Simulation (DNS). These geometries are essential for nuclear reactor systems, where efficient heat transfer and stable flow patterns are vital to ensure operational safety, reliability, and performance. The study focuses on evaluating the limitations of traditional thermal-hydraulic modeling approaches and advancing the understanding of flow physics in complex geometries.

Since Computational Fluid Dynamics (CFD) simulations are computationally expensive, system codes such as RELAP5, TRACER, and SPECTRA (developed by NRG) are widely used in reactor safety and design analysis. These codes rely on conventional pipe flow correlations to approximate thermal-hydraulic behavior, which are not representative of the intricate flow patterns observed in rod bundle arrangements. Such geometries are characterized by secondary vortices, gap street vortices, and the coupling of these vortices across multiple planes, forming a complex rod bundle vortex network. This study addresses these challenges by comparing the flow and thermal characteristics of pipe and subchannel geometries to evaluate the validity and limitations of pipe-based correlations.

To identify the subchannel geometry that best represents a rod bundle arrangement, square and 2×2 subchannel configurations were selected for detailed investigation. These geometries were modeled with a pitch-to-diameter (P/D) ratio of 1.3263, typical of PWR fuel assemblies, and simulated at a Bulk Reynolds number (Re_b) of 5300. The square subchannel geometry represents a simplified cross-sectional domain, while the 2×2 subchannel configuration captures inter-subchannel interactions and the enhanced coupling effects seen in rod bundles. Using the Nek5000 spectral element solver, the simulations employed advanced numerical techniques, including spatial-temporal averaging through flow-through time (FTTs) metrics and further spatial averaging over unit cells, to achieve statistically converged results. Rigorous validation of pipe configuration with reference data ensured the accuracy of the computational framework.

The results highlight significant differences in turbulence structures and heat transfer performance between the pipe, square subchannel, and 2×2 subchannel configurations. While pipe correlations provide a baseline for comparison, they fail to capture the complex flow interactions observed in rod bundles. The 2×2 subchannel geometry emerges as a more accurate representation of rod bundle dynamics due to its ability to simulate enhanced inter-subchannel mixing and vortex coupling. These findings emphasize the importance of geometry-specific modeling in accurately predicting thermal-hydraulic behavior in nuclear reactors.

This work bridges the gap between simplified system codes and detailed physics-based modeling of rod bundle flows. The insights gained from this study provide a foundation for improving thermal-hydraulic predictions and advancing the design and safety of nuclear reactor systems. Future research will extend these findings to explore higher Reynolds numbers, diverse Prandtl numbers, wall effects, and alternative rod bundle configurations, further contributing to the development of advanced engineering tools for nuclear applications.

Contents

Acknowledgements	i
List of Figures	vi
List of Tables	ix
1 Introduction	1
1.1 Nuclear Reactor	1
1.2 Rod Bundle	3
1.3 Non-dimensional parameters	4
1.4 Heat transfer in a Pipe vs Subchannel	5
1.5 Flow Physics in Rod Bundle Subchannel	8
1.6 Research Formulation	12
2 Turbulence	13
2.1 Turbulent scales	13
2.2 Governing Equations	15
2.3 Tubulent Kinetic Energy and it's Budget terms	15
2.4 Temperature Heat Flux and its Budget Terms	16
2.5 Numerical simulation for Subchannel Domains	17
3 Comptational Model	19
3.1 Nek5000 - SEM solver	19
3.2 Computational Domain	20
3.3 Mesh	21
3.4 Temperature fields	24
3.5 Boundary Conditions	25
3.6 Initial Conditions	26
3.7 Post-Processing Approaches	26
4 Pipe	27
4.1 Resoluion	27
4.2 Convergence of statistical calculation	29
4.3 Validation	30
5 Subchannel	36
5.1 Flow and Heat Transfer Statistics Approach	36
5.2 Resolution	38
5.3 Square subchannel	38
5.4 2x2 subchannel	40
5.5 Comparison between Square and 2x2 Subchannel	43
5.6 Conclusion	53
6 Comparative Study	54
6.1 Comparison Approach	54
6.2 Higher Order Statistics	54
6.3 Velocity vectors coloured by temperature	58
6.4 Nusselts number	63
7 Conclusion and Future Scope	65
7.1 Conclusion	65
7.2 Recommendations	66
7.3 Future Scope	66

References **68**

A Appendix A **69**

 A.1 Pipe THF Budget terms 69

 A.2 Subchannel: Comparison of its THF budget 70

 A.3 Comparative study: Pipe and 2x2 Subchannel 70

List of Figures

1.1	PWR Nuclear Reactor [1]	2
1.2	Nuclear Reactor Growth Worldwide [4]	2
1.3	Rod Bundle [5]	3
1.4	Different rod bundle arrangements	3
1.5	rod bundle Geometry [6]	4
1.6	Illustration of the Tea Leaf Paradox [12]	8
1.7	Secondary flow in a rectangular duct corner [12]	9
1.8	Shear layer instability and vortex sheet formation [13]	9
1.9	Flow pulsations in the subchannel narrow gap visualized with a velocity contour [15]	10
2.1	Turbulent scales [26]	14
2.2	Energy Cascade $E(k)$ [27]	14
3.1	Comparison of different subchannel geometry	21
3.2	Base Mesh of Pipe case (N=1)	22
3.3	Base Mesh of Subchannel Cases (N=1)	23
3.4	Schematic representation of periodic boundary conditions for subchannel configurations	25
4.1	Comparative visualization of instantaneous velocity field distributions at varying polynomial orders ($t^* = 1203$).	28
4.2	Wall-normal distribution of normalized mean axial velocity (u^+) for varying polynomial orders	28
4.3	Wall-normal distribution of normalized turbulent kinetic energy (k^+) for varying polynomial orders	28
4.4	Distribution of cell size normalized by kolmogorov length scale ($\frac{\Delta}{\eta}$) for $N = 7$	29
4.5	Axial velocity (u_z) plotted against y^+ for different averaging periods.	30
4.6	Kinetic Energy plotted against y^+ for different averaging periods.	30
4.7	Axial velocity (u_z) plotted against y^+ for last averaging periods compared to reference [37].	31
4.8	Kinetic Energy plotted against y^+ for last averaging periods compared to reference [37].	31
4.9	Turbulent Kinetic Energy (TKE) Budget terms at an averaging period of 60 FTTs plotted against wall distance (y^+) compared to the reference [37].	31
4.10	Excess temperature (mean temperature) distribution for $Pr = 0.025$ at 60 FTT, plotted against wall distance (y^+).	33
4.11	Excess temperature (mean temperature) distribution for $Pr = 1$ at 60 FTT, plotted against wall distance (y^+).	33
4.12	Temperature fluctuations for $Pr = 0.025$ at 60 FTT, plotted against wall distance (y^+).	33
4.13	Temperature fluctuations for $Pr = 1$ at 60 FTT, plotted against wall distance (y^+).	33
4.14	Streamwise turbulent heat flux ($w'T'$) at 60 FTT plotted against wall distance (y^+).	34
4.15	Streamwise turbulent heat flux ($w'T'$) at 60 FTT plotted against wall distance (y^+).	34
4.16	Nusselt number as a function of Reynolds number. Dotted markers represent $Pr = 0.025$, while hollow markers represent $Pr = 1$. Red indicates the isothermal condition, and green indicates the isoflux condition.	35
5.1	Unit cell and Statistical approaches for a Subchannel domain	37
5.2	Distribution of cell size normalized by Kolmogorov length-scale ($\frac{\Delta}{\eta}$) for $N = 5$	37
5.3	Axial velocity (u_z) plotted using the circumferential method for different averaging periods	39
5.4	Velocity fluctuations along 3 axes plotted using the circumferential method for different averaging periods	39
5.5	Turbulent Kinetic Energy (TKE) Budget terms plotted using the circumferential method for different averaging periods	40

5.6	Axial velocity (u_z) plotted using the circumferential method for different FTT values.	41
5.7	Velocity fluctuations along three axes using the circumferential method for different FTT values.	41
5.8	Turbulent Kinetic Energy (TKE) budget terms at 10 FTT using the circumferential method	42
5.9	Axial velocity (u_z) comparison between configurations, plotted using the circumferential method at converged FTT.	44
5.10	Wall shear stress (τ_w) distribution comparison, plotted using the angle method at converged FTT.	44
5.11	Normal stress distributions as a function of wall distance (y^+) at converged FTT for both configurations.	44
5.12	Reynolds stress distributions as a function of wall distance (y^+) at converged FTT for both configurations.	44
5.13	Turbulent Kinetic Energy (TKE) budget distributions as a function of wall distance (y^+) at converged FTT for both configurations.	45
5.14	Mean temperature distribution for $Pr = 0.025$	46
5.15	Mean temperature distribution for $Pr = 1$	46
5.16	Temperature fluctuations for $Pr = 0.025$	47
5.17	Temperature fluctuations for $Pr = 1$	47
5.18	Turbulent heat flux for $Pr = 0.025$	48
5.19	Turbulent heat flux for $Pr = 1$	48
5.20	Time-averaged autocorrelation of x-velocity (u') fluctuations in the X normal plane of the square subchannel.	49
5.21	Time-averaged autocorrelation of x-velocity (u') fluctuations in the Y normal plane of the square subchannel.	49
5.22	Time-averaged autocorrelation of y-velocity (v') fluctuations in the X normal plane of the square subchannel.	50
5.23	Time-averaged autocorrelation of y-velocity (v') fluctuations in the Y normal plane of the square subchannel.	50
5.24	Time-averaged autocorrelation of z-velocity (w') fluctuations in the X normal plane of the square subchannel.	50
5.25	Time-averaged autocorrelation of z-velocity (w') fluctuations in the Y normal plane of the square subchannel.	50
5.26	Time-averaged autocorrelation of x-velocity (u') fluctuations in the X normal plane of the 2x2 subchannel.	51
5.27	Time-averaged autocorrelation of x-velocity (u') fluctuations in the Y normal plane of the 2x2 subchannel.	51
5.28	Time-averaged autocorrelation of y-velocity (v') fluctuations in the X normal plane of the 2x2 subchannel.	51
5.29	Time-averaged autocorrelation of y-velocity (v') fluctuations in the Y normal plane of the 2x2 subchannel.	51
5.30	Time-averaged autocorrelation of z-velocity (w') fluctuations in the X normal plane of the 2x2 subchannel.	52
5.31	Time-averaged autocorrelation of z-velocity (w') fluctuations in the Y normal plane of the 2x2 subchannel.	52
6.1	Radial distance (R) in the pipe configuration	55
6.2	Wall-Normal Distance (L_3) in the single subchannel configuration	55
6.3	Normalized Axial Velocity Distribution Comparing Pipe and 2x2 Subchannel Flow Configurations	55
6.4	Turbulent Kinetic Energy Profiles Revealing Geometric Flow Variations	55
6.5	Comprehensive Turbulent Kinetic Energy Budget Analysis	56
6.6	Mean Temperature Distribution for Low Prandtl Number Isothermal Condition	57
6.7	Mean Temperature Distribution for Unity Prandtl Number	57
6.8	Temperature Fluctuation Intensity for Low Prandtl Number	57
6.9	Temperature Fluctuation Intensity for Unity Prandtl Number	57
6.10	Streamwise Turbulent Heat Flux for Low Prandtl Number	58

6.11 Streamwise Turbulent Heat Flux for Unity Prandtl Number	58
6.12 Instantaneous velocity vectors in pipe flow colored by temperature, illustrating turbulent heat transport.	59
6.13 Averaged velocity vectors in pipe flow colored by temperature, illustrating turbulent heat transport.	60
6.14 Instantaneous velocity vectors in 2x2 subchannel flow colored by temperature, illustrating turbulent heat transport.	61
6.15 Averaged velocity vectors in 2x2 subchannel flow colored by temperature, illustrating turbulent heat transport.	62
6.16 Nusselt number (Nu) for Prandtl number $Pr = 1$ compared with Reynolds number (Re) between pipe and 2x2 subchannel cases.	63
6.17 Nusselt number (Nu) for Prandtl number $Pr = 0.025$ compared with Reynolds number (Re) between pipe and 2x2 subchannel cases.	63
A.1 THF Budget terms for scalar Temperature T_1 at 60 FTT plotted against wall distance (y^+).	69
A.2 THF Budget terms for scalar Temperature T_2 at 60 FTT plotted against wall distance (y^+).	69
A.3 THF Budget terms for scalar Temperature T_3 at 60 FTT plotted against wall distance (y^+).	69
A.4 THF Budget terms for scalar Temperature T_4 at 60 FTT plotted against wall distance (y^+).	69
A.5 Thermal Heat Flux (THF) budget for scalar temperature T_1 , comparing square and 2x2 subchannel cases, plotted against distance.	70
A.6 Thermal Heat Flux (THF) budget for scalar temperature T_2 , comparing square and 2x2 subchannel cases, plotted against distance.	70
A.7 Thermal Heat Flux (THF) budget for scalar temperature T_3 , comparing square and 2x2 subchannel cases, plotted against distance.	70
A.8 Thermal Heat Flux (THF) budget for scalar temperature T_4 , comparing square and 2x2 subchannel cases, plotted against distance.	70
A.9 Thermal Heat Flux (THF) budget for scalar temperature T_1 , comparing pipe and 2x2 subchannel cases, plotted against distance.	70
A.10 THF budget for scalar temperature T_2 , comparing pipe and 2x2 subchannel cases, plotted against distance.	70
A.11 Thermal Heat Flux (THF) budget for scalar temperature T_3 , comparing pipe and 2x2 subchannel cases, plotted against distance.	71
A.12 THF budget for scalar temperature T_4 , comparing pipe and 2x2 subchannel cases, plotted against distance.	71

List of Tables

3.1	Numerical schemes and parameters in Nek5000	20
3.2	Subchannel Geometry Parameters: Original and Modified Specifications	21
3.3	Mesh Specifications and Element Distribution for Pipe Geometry	22
3.4	Grid resolution parameters comparing present DNS with reference data from El Khoury et al.2013. Values are presented as minimum and maximum in wall units.	23
3.5	Mesh Specifications and Element Distribution for Subchannel Cases	23
3.6	Grid resolution parameters for the 2x2 subchannel (N = 5) case. Values are presented as minimum and maximum in wall units.	24
3.7	Scalar Quantities Defined by Prandtl Number and Boundary Conditions	24
4.1	Relative L^2 norm errors for velocity statistics compared to the reference data [37]	29
4.2	Flow-through times (FTTs) and corresponding normalized time scales	29
5.1	Flow-through times (FTTs) and corresponding normalized time scales	38
5.2	Relative L^2 norm error analysis at 35FTT	40
5.3	Flow-through times (FTTs) and corresponding normalized time scales	41
5.4	Relative L^2 norm error analysis at 10 FTT	42
5.5	Auto correlation parameters	50

Introduction

This chapter examines the fundamental principles and significance of Pressurized Water Reactors (PWRs) in nuclear energy generation. The discussion focuses on two key aspects:

1. PWR Functionality and Geometries

- An analysis of the operational mechanisms and thermodynamic cycles underpinning PWR systems, highlighting their importance in contemporary nuclear power generation.
- A detailed exploration of fuel assembly configurations (rod bundle geometries), emphasizing their influence on coolant flow patterns and heat transfer characteristics.

2. Turbulent Mixing Phenomena in Rod Bundles

- An in-depth investigation of complex flow behaviours within rod bundles, including cross-flow mixing, secondary flows, and their implications for reactor safety and efficiency.
- Elucidation of key physical phenomena in subchannel flow, such as Prandtl's second kind of secondary flows and the gap vortex street, establishing a critical foundation for the subsequent evaluation of Direct Numerical Simulation (DNS) in this context.

Additionally, this chapter delineates the specific research questions that will be addressed in subsequent chapters, providing a framework for the thesis's investigative trajectory in PWR thermal-hydraulics. Through this exploration, we aim to provide a robust theoretical framework for interpreting DNS results in subchannel configurations, enhancing our understanding of complex flow behaviors in nuclear reactor core geometries.

1.1. Nuclear Reactor

A nuclear reactor is a highly engineered system designed to maintain a controlled nuclear fission chain reaction, converting nuclear energy into thermal energy for power generation. Reactors are central to the production of electricity in nuclear power plants, where they serve as the heart of the system that drives steam turbines to generate electricity. Various types of nuclear reactors have been developed, with the most common being Pressurized Water Reactors (PWR), Boiling Water Reactors (BWR), and Fast Breeder Reactors (FBR), each offering different approaches to controlling the nuclear reaction and handling heat removal. The evolution of these technologies can be categorized into four main generations, each reflecting advancements in safety, efficiency, and sustainability. From the early Generation I prototypes to the more sophisticated Generation IV designs, continuous improvements have been made to increase both reactor longevity and fuel utilization. PWRs, developed in the Generation II phase, have emerged as the dominant reactor type worldwide due to their inherent safety features, stability under varying conditions, and well-established commercial design. These reactors are crucial in the global nuclear energy mix, contributing to reliable, low-carbon electricity production.

A Pressurized Water Reactor (PWR) operates on a well-established and reliable principle: water is kept under high pressure to prevent it from boiling, even at the elevated temperatures produced by nuclear fission within the reactor core, as illustrated in Figure 1.1. The reactor vessel houses enriched uranium fuel, where nuclear fission occurs, releasing significant heat. This heat is absorbed by water circulating through the core under high pressure, maintaining it in liquid form. The heated water then passes through a heat exchanger, known as a steam generator, transferring its thermal energy to a secondary loop.

This secondary loop, in turn, generates steam that drives turbines, producing electricity. Separating the radioactive primary loop from the secondary loop enhances safety by containing radiation within the primary circuit, a critical feature of PWRs. Globally, the reactor vessel typically operates at pressures of 15-16 MPa and temperatures exceeding 300°C, ensuring energy transfer efficiency.

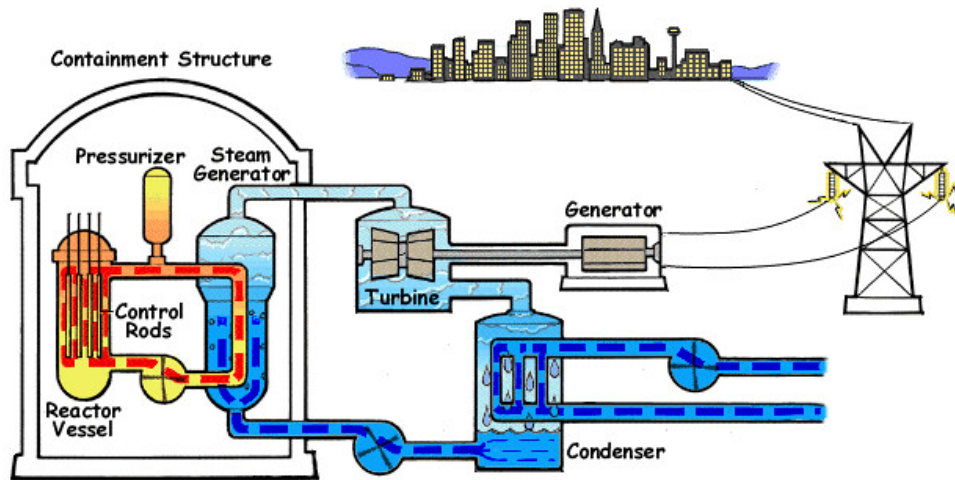


Figure 1.1: PWR Nuclear Reactor [1]

PWRs dominate the nuclear landscape due to their proven safety mechanisms, reliability, and economic efficiency. With approximately 300 out of 450 operational nuclear reactors worldwide ([2][3]) being PWRs, they represent about 70% of the global nuclear reactor fleet. This widespread adoption stems from their highly stable operation, as the pressurized water serves not only as a coolant but also as a moderator, maintaining controlled reactivity. In terms of capacity, PWRs collectively contribute over 200 gigawatts (GW) of electricity generation worldwide, significantly bolstering the energy mix.

As illustrated in Figure 1.2, the growth of nuclear generation capacity varies significantly across different regions. The graph shows that West & Central Europe and North America have historically led in nuclear power generation, with Asia showing rapid growth in recent decades. This trend underscores the global expansion of nuclear energy, with PWRs playing a crucial role in this growth.

Additionally, the mature nature of PWR technology, combined with streamlined fuel management processes and established regulatory frameworks, makes PWRs an attractive and cost-effective option for both developed and developing countries, driving continued investment in this reactor type. Their flexibility and robust safety systems, such as multiple redundant cooling mechanisms, ensure safe operations even under extreme conditions, further solidifying their status as the most preferred reactor design globally.

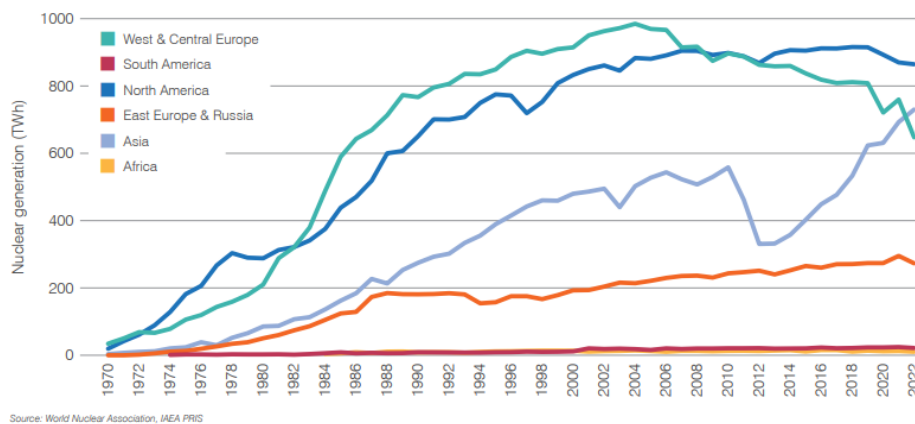


Figure 1.2: Nuclear Reactor Growth Worldwide [4]

1.2. Rod Bundle

Fuel rod bundles constitute a critical component of Pressurized Water Reactors (PWRs). These bundles typically adopt one of three primary geometric configurations: triangular, square, or hexagonal arrays (Figure 1.3).

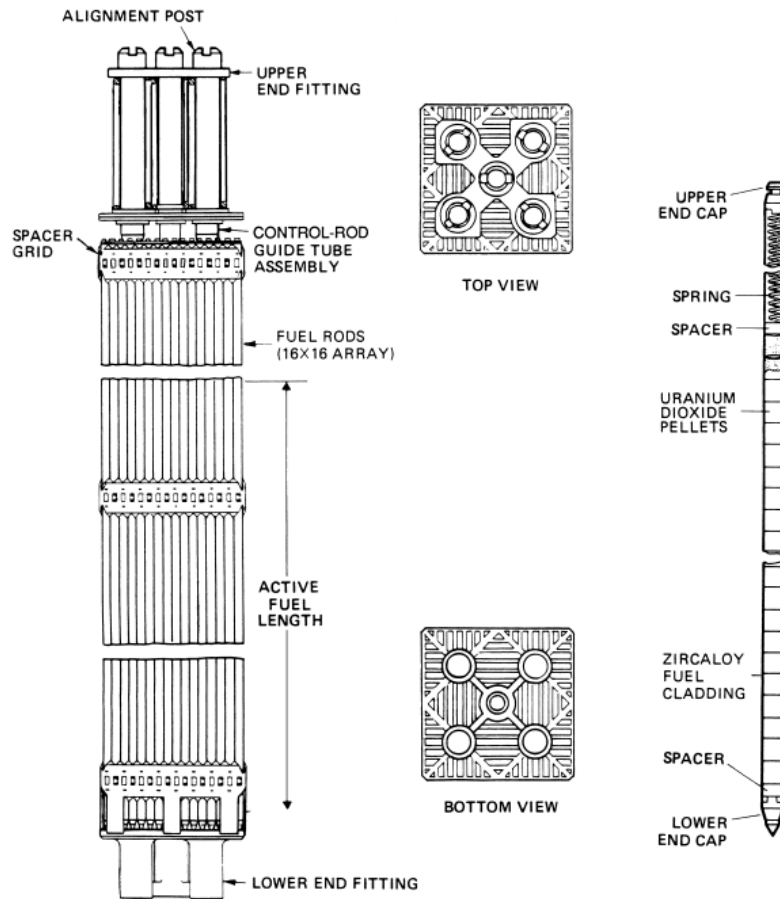


Figure 1.3: Rod Bundle [5]

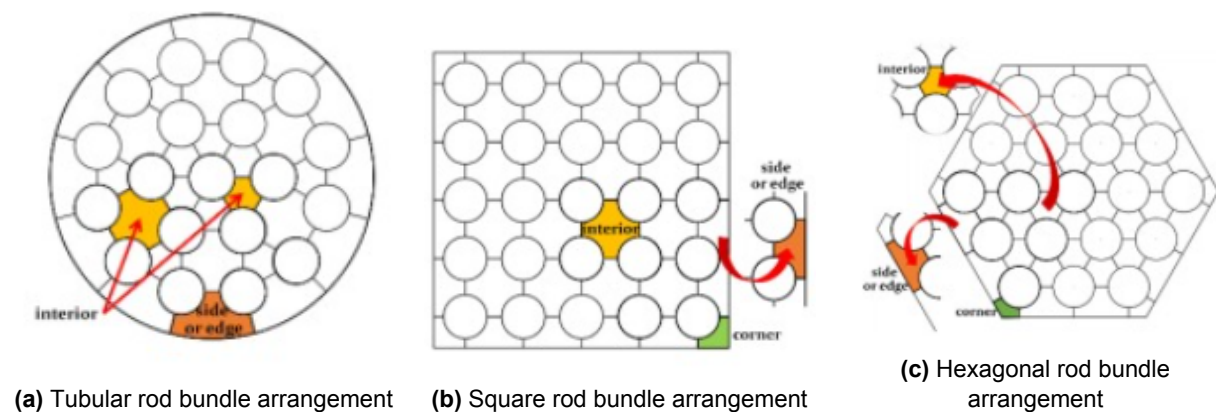


Figure 1.4: Different rod bundle arrangements

Two key design parameters, defining the spacing between adjacent rods (pitch-to-diameter ratio, P/D)

and the proximity of peripheral rods to the channel wall (wall-to-diameter ratio, W/D), characterize these arrangements, as shown in Figure 1.5.

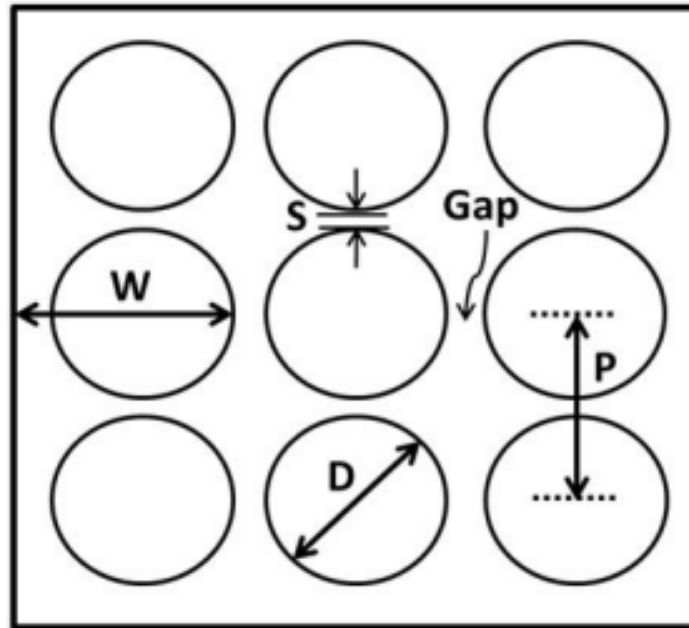


Figure 1.5: rod bundle Geometry [6]

The hydraulic diameter, D_h , is a crucial parameter used in the Reynolds number calculation for non-circular channel shapes, which is an important design factor for subchannel configurations in nuclear reactor systems. The hydraulic diameter is defined as:

$$D_h = \frac{4 \times \text{Cross-sectional Area}}{\text{Wetted Perimeter}} \quad (1.1)$$

The hydraulic diameter provides a characteristic length scale that accounts for the non-circular geometry of the flow channel.

Rod bundles in PWRs are generally tightly packed, with lower P/D ratios indicating higher rod densities. This compact arrangement engenders a complex fluid domain, yielding flow characteristics distinct from those observed in simpler pipe or channel flows, a known phenomenon called "Secondary Flows".

The unique flow physics within these subchannels has been a focal point of thermal-hydraulics research for over two decades, yet a comprehensive understanding remains elusive. Recent studies have identified large-scale swirling coherent structures and transverse flow pulsations in the rod-rod and rod-wall gap regions, a phenomenon termed "Gap Vortex Street". These flow structures promote enhanced turbulent mixing and localized temperature reduction, potentially improving heat transfer characteristics.

Understanding and controlling the flow physics in these subchannel geometries is crucial for optimizing heat transfer and ensuring the safe and efficient operation of PWRs. This remains an active area of research, with significant implications for nuclear reactor design and performance.

1.3. Non-dimensional parameters

The Reynolds number (Re) provides fundamental insights into the flow characteristics and fluid behaviour, while the Prandtl number (Pr) and Nusselt number (Nu) are essential parameters that characterize heat transfer capabilities and thermal boundary layer behaviour in fluids.

1.3.1. Reynolds number

The Reynolds number (Re) is a dimensionless parameter that represents the ratio of inertial forces to viscous forces in a fluid. It is defined as:

$$\text{Re} = \frac{\rho u D_h}{\mu} \quad (1.2)$$

Where:

- ρ is the fluid density,
- u is the fluid velocity,
- D_h is the hydraulic diameter,
- μ is the dynamic viscosity.

The Reynolds number is essential in our study as it characterizes the flow behaviour and provides insights into the fluid dynamics within both the tube and PWR sub-channel geometries.

1.3.2. Prandtl number

The Prandtl number (Pr) is a dimensionless parameter that represents the ratio of momentum diffusivity to thermal diffusivity in a fluid. It is defined as:

$$\text{Pr} = \frac{\mu C_p}{k} \quad (1.3)$$

Where:

- μ is the dynamic viscosity,
- C_p is the specific heat capacity,
- k is the thermal conductivity of the fluid.

The Prandtl number is essential in our study because it helps characterize the thermal behaviour of the coolant in both the tube and PWR sub-channel geometries. It influences the relative thickness of the momentum and thermal boundary layers, which in turn affects heat transfer rates.

1.3.3. Nusselt Number

The Nusselt number (Nu) is another crucial dimensionless parameter in heat transfer analysis. It represents the ratio of convective to conductive heat transfer across a boundary and is defined as:

$$\text{Nu} = \frac{hL}{k} \quad (1.4)$$

Where:

- h is the convective heat transfer coefficient,
- L is the characteristic length,
- k is the thermal conductivity of the fluid.

In our study, the Nusselt number will be a key focus as it directly quantifies the enhancement of heat transfer through a fluid layer as a result of convection relative to conduction across the same fluid layer.

1.4. Heat transfer in a Pipe vs Subchannel

Flows within the complex geometry of nuclear reactor rod bundles exhibit unique characteristics that significantly differ from simpler channel or pipe flows. The tightly packed arrangement of fuel rods introduces narrow gaps, leading to strong, transverse, large-scale motions across the gaps between adjacent rods and between a rod and the containment wall. This inter-subchannel mixing greatly enhances the exchange of momentum and energy, ultimately impacting heat transfer performance. These flow behaviours are rarely observed in conventional pipe flows, underscoring the distinct hydrodynamic and thermal conditions present in reactor assemblies.

The geometry of heat transfer surfaces in nuclear reactors thus plays a crucial role in determining thermal behaviour. While idealized pipe geometries are often used for empirical correlations, they fail to capture the intricate flow structures within actual rod bundle configurations, where large-scale transverse flows and inter-subchannel mixing are prominent. Consequently, standard one-dimensional subchannel codes based on simplified assumptions may not fully account for the complex flow dynamics in rod bundles. To accurately model and optimize reactor heat transfer, it is essential to adopt computational and experimental approaches that address these specific geometric effects.

1.4.1. Conventional Correlations vs. Complex Geometries

Conventional correlations, such as the Dittus-Boelter and Gnielinski correlations, were developed based on experiments conducted with simple pipe geometries. These correlations have been widely used in thermal-hydraulic system codes to predict heat transfer in various systems, including nuclear reactors. However, their applicability to more complex geometries, such as those found in reactor subchannels, has been a subject of ongoing research and debate.

Subchannels in a nuclear reactor fuel assembly typically have a more complex cross-sectional shape compared to circular pipes. They are often characterized by a non-circular flow area bounded by multiple fuel rods. This geometry creates unique flow patterns and turbulence structures that can significantly affect heat transfer.

Dittus-Boelter Correlation

For turbulent flow in tubes and subchannels, the Dittus-Boelter correlation is a widely used empirical correlation for calculating the Nusselt number. It is expressed as:

$$\text{Nu} = 0.023\text{Re}^{0.8}\text{Pr}^n \quad (1.5)$$

Where $n = 0.4$ for heating and $n = 0.3$ for cooling. This correlation provides a straightforward method for determining the Nusselt number in both tube and PWR subchannel geometries, enabling the calculation of convective heat transfer coefficients for simple flow configurations.

Gnielinski Correlation

The Gnielinski correlation offers improved accuracy over a wider range of Reynolds numbers for tube and subchannel flows. It is given by:

$$\text{Nu} = \frac{(f_D/8)(\text{Re} - 1000)\text{Pr}}{1 + 12.7(f_D/8)^{0.5}(\text{Pr}^{2/3} - 1)} \quad (1.6)$$

Where f_D is the Darcy friction factor, calculated as:

$$f_D = [0.79 \ln(\text{Re}) - 1.64]^{-2} \quad (1.7)$$

This correlation provides more reliable predictions of Nusselt numbers in tube geometries, particularly in the transitional regime and for cases with significant property variations.

Kazimi-Carelli Correlation

For liquid metal flows with Péclet numbers less than or equal to 150 and specifically developed for low Prandtl number fluids ($\text{Pr} = 0.025$) such as liquid metals, the Kazimi-Carelli correlation provides an extension to standard heat transfer correlations:

$$\text{Nu} = 4.496 \left[-16.15 + 24.96 \left(\frac{P}{D} \right) - 8.55 \left(\frac{P}{D} \right)^2 \right] \quad (1.8)$$

Where P/D represents the pitch-to-diameter ratio of the flow geometry. This correlation accounts for the unique heat transfer characteristics of liquid metals in nuclear applications.

1.4.2. Enhanced Heat Transfer in Subchannels

Recent studies have indicated that heat transfer characteristics in subchannel geometries can differ substantially from those in pipe geometries. In particular, some research has suggested that subchannels may exhibit up to 30% [7] higher heat transfer rates compared to pipes under similar flow conditions. This enhanced heat transfer can be attributed to several factors:

- **Flow distribution:** The non-uniform flow distribution in subchannels can lead to increased turbulence and mixing, promoting heat transfer.
- **Secondary flows:** The complex geometry of subchannels can induce secondary flows, which enhance fluid mixing and heat transfer.
- **Surface area effects:** The ratio of heated surface area to flow area in subchannels may differ from that in pipes, affecting overall heat transfer efficiency.
- **Turbulence enhancement:** The presence of spacer grids and other structural elements in fuel assemblies can increase turbulence mixing, further enhancing heat transfer.

1.4.3. Implications for Reactor Safety and Design

The discrepancy between pipe-based correlations and actual subchannel behaviour has important implications for reactor safety analysis and design. Using pipe-based correlations may lead to conservative estimates of heat transfer in some cases, potentially resulting in overly restrictive operational limits. On the other hand, it could also lead to underestimation of heat transfer in certain scenarios, which could be a safety concern.

1.5. Flow Physics in Rod Bundle Subchannel

This section explores two fundamental physical phenomena that significantly influence the thermal-hydraulic behaviour in subchannel flows. First, we examine Prandtl's second kind of secondary flows, turbulence-driven vortical structures that emerge in non-circular channels and impact heat and momentum transfer. These flows, first observed by Nikuradse [8] in rectangular ducts, are critical for understanding the complex flow patterns in subchannel geometries. Second, we investigate the gap vortex street phenomenon, a flow instability mechanism that develops due to sharp shear layers at interfaces in subchannel configurations. Through detailed analysis of these phenomena, we establish a foundation for interpreting flow behaviour in nuclear reactor subchannels and evaluating Direct Numerical Simulation (DNS) results in these geometries.

1.5.1. Secondary flow

Secondary flow is a crucial phenomenon in fluid dynamics, playing a pivotal role in understanding the physical mechanisms occurring in non-circular channel flows, particularly in subchannel flows, as investigated in this thesis. During his experimental studies on flow physics in rectangular ducts, Nikuradse observed that the mean axial flow formed bulges near the corners [8]. Prandtl later attributed these corner bulges to the presence of what would become known as secondary flows of the second kind [9]. This theoretical explanation by Prandtl was subsequently validated through Nikuradse's experimental investigations, confirming the existence of secondary flows in rectangular duct flows. The quantitative characterization of these secondary flows was achieved three decades later, revealing velocities not exceeding 1-2% of the mean axial flow [10].

One of the earliest and most accessible manifestations of secondary flows is the phenomenon known as the "Tea Leaf Paradox," first observed by Albert Einstein [11]. When a cup of tea containing tea leaves is stirred, the leaves tend to concentrate at the centre of the cup's bottom, contrary to the intuitive expectation that centrifugal forces would push them towards the walls (Figure 1.6). This paradox was elucidated in detail by Nikolay Nikitin [12].



Figure 1.6: Illustration of the Tea Leaf Paradox [12]

To understand the mechanism, consider an inner corner of Nikuradse's rectangular duct, which can be decomposed into two flat plate geometries. The velocity perturbations move transversely along the mean flow near the wall. When these flat plates are combined to form an inner corner, the velocity perturbations create a curvilinear shape pointing towards the corner (Figure 1.7). This configuration results in a centrifugal force balanced by a pressure gradient. The increased pressure near the corner, coupled with zero velocity perturbation at the wall, is counterbalanced by fluid movement along the walls, where energy is dissipated due to wall friction. This quasi-stable structure is now known as Prandtl's secondary flow of the second kind.

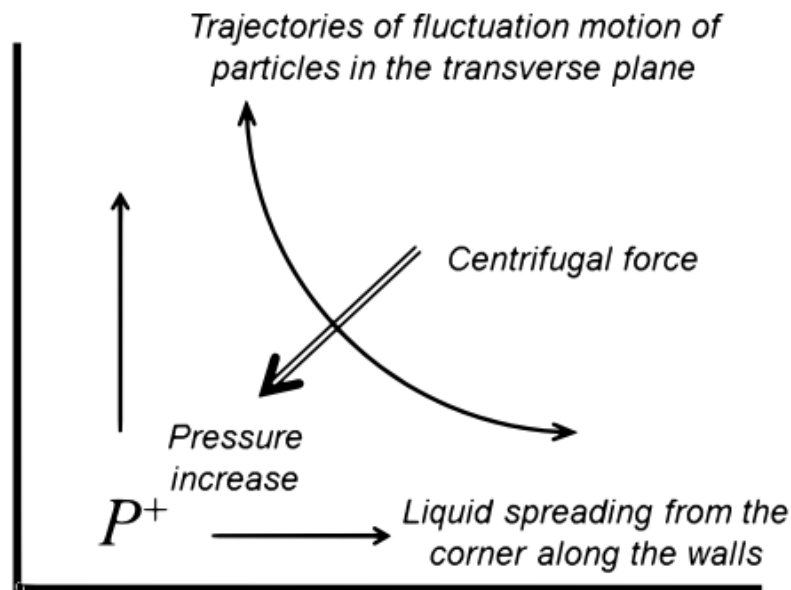


Figure 1.7: Secondary flow in a rectangular duct corner [12]

1.5.2. Gap vortex street

Over the past two decades, substantial research has focused on the complex flow structures in subchannel geometries, particularly within nuclear reactor rod bundles. These configurations exhibit distinct large-scale motions driven by an inherent instability mechanism linked to the narrow gaps between subchannels. Such geometries produce an inflectional cross-sectional velocity profile, which fosters hydrodynamic instability.

Hydrodynamic instability in these systems is characterized by the amplification of perturbations in the flow, resulting in coherent large-scale motions. While this instability shares similarities with other flow instabilities, such as those in boundary layers and wakes, it is distinct due to the unique geometry of the subchannel. The inflectional velocity profile within rod bundles renders the flow prone to instabilities akin to classic shear flows.

A prominent example of this is the Kelvin-Helmholtz instability, which arises at shear layers, such as those at the interfaces between subchannels. Vortical structures are generated when there is a velocity differential across these interfaces, evolving into organized vortex streets. These vortex streets significantly enhance cross-channel mixing, thus influencing the overall flow dynamics. Understanding such instabilities is crucial for accurately modelling large-scale motions and inter-subchannel interactions in subchannel flow studies.

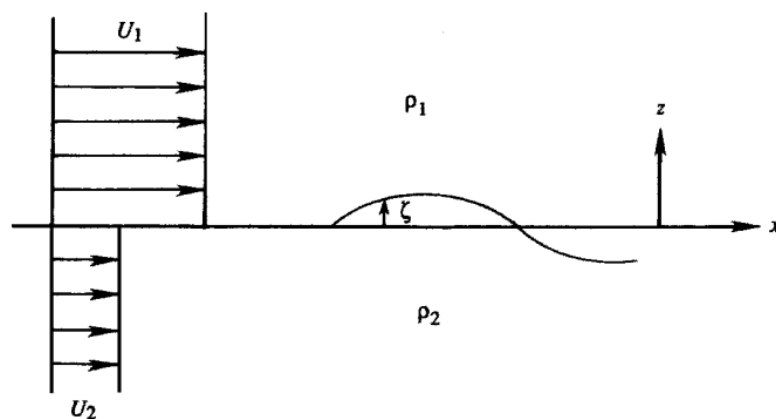


Figure 1.8: Shear layer instability and vortex sheet formation [13]

A linear stability analysis of an inviscid fluid with the velocity profile shown in Figure 1.8 reveals an unstable mode when $U_1 \neq U_2$ (Kundu and Cohen [13]), leading to the formation of a vortex sheet, as depicted in the figure.

In subchannel geometries, shear layer instabilities, particularly *gap instability*, drive the formation of large vortical structures in the gap regions. While extensively studied, the mechanisms underlying these instabilities remain unclear. One hypothesis suggests the involvement of Prandtl's secondary flows of the third kind, which are generated by turbulence anisotropy in non-circular ducts. This mechanism, though relevant, is not discussed in detail here.

The von Kármán vortex street, a well-known phenomenon of periodic vortex shedding, provides an analogy for understanding vortex dynamics in subchannels. Although a detailed exploration of von Kármán instability is beyond the scope of this study, it is relevant in the case of moving fuel rods, a common condition in nuclear reactors. This is mainly due to the production of large vortical coherent structures, which induce vibrations because of Fluid-Structure Interaction (FSI). The presence of these vortices can contribute to significant vibrations in the rods, which are crucial for understanding reactor performance and safety under operational conditions.

Flow pulsations is a term used in accordance with the nomenclature set by Tavoularis [14], describing the oscillatory nature of the flow velocity in gap regions. However, these pulsations are simply a symptom of the flow's state and do not offer insight into the structure of the velocity field. The figure 1.9 below showcases the sinusoidal-like shape velocity magnitude contours in the gap region, representing the flow pulsation observed.

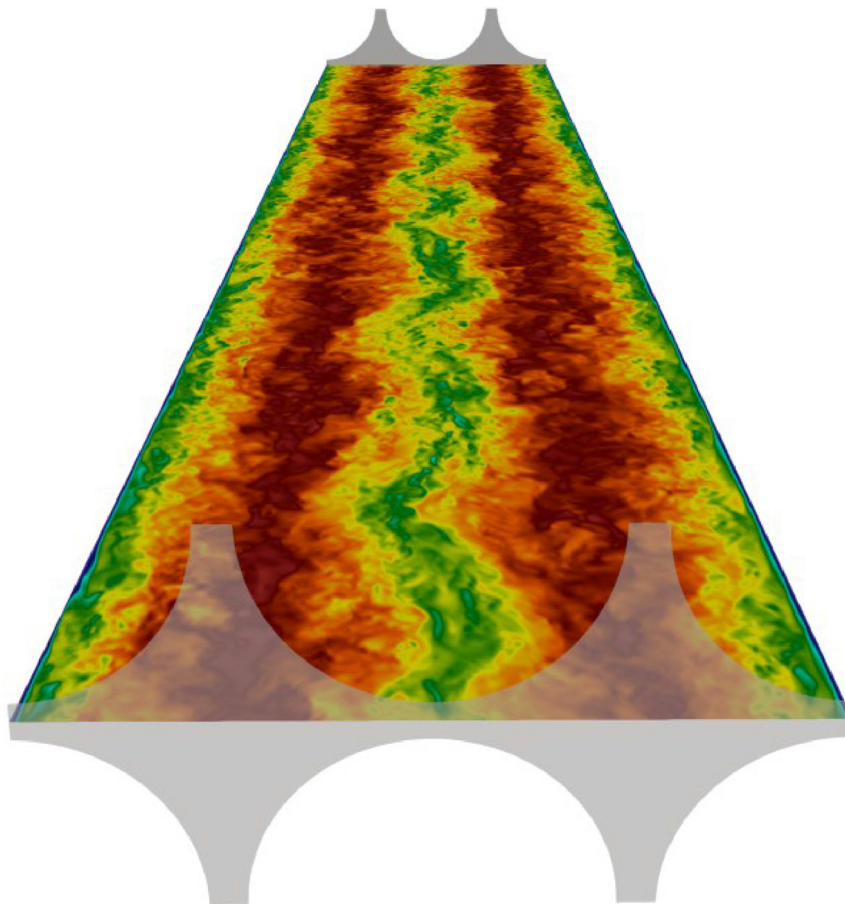


Figure 1.9: Flow pulsations in the subchannel narrow gap visualized with a velocity contour [15]

The term *gap vortex street* more accurately captures the interactions between counter-rotating vortices formed on either side of the gap. In rod bundles, the coupling of these vortex streets across multiple gaps

forms the *rod bundle vortex network*, an area of ongoing research. The complexity of these interactions, which depend on the size and shape of the gaps, presents challenges in understanding the flow physics.

The combination of hydrodynamic instabilities and secondary flows, particularly Prandtl's secondary flows of the second and third kinds, is central to these phenomena. However, the detailed mechanisms behind these interactions remain uncertain and are not within the scope of the present study.

1.5.3. Literature study on rod bundle

Meyer [16] provides a comprehensive review of experimental and numerical research on large-scale swirling structures in rod-bundle flows, commonly observed in nuclear reactor cores and heat exchangers. While early studies in the 1970s and 1980s attributed high momentum transfer in gap regions to secondary flows, recent research demonstrates these flows contribute minimally (1-2%) to overall flow dynamics. The formation of quasi-periodic vortices in the gap region is primarily attributed to the Kelvin-Helmholtz instability, driven by velocity differentials between high-speed core flow and slower gap flow.

Meyer's analysis [16] emphasizes the significance of gap-spacing (P/D or W/D) in flow behavior, where reduced spacing correlates with increased turbulence intensities. Advanced computational methodologies, including Direct Numerical Simulations (DNS), Large Eddy Simulations (LES), or anisotropic Unsteady Reynolds-Averaged Navier-Stokes (URANS) models, are essential for accurately capturing these flow characteristics and analyzing the complex interaction between turbulence, shear layers, and coherent structures.

Gosset and Tavoularis [17] first identified coherent structures in laminar flow within the narrow gap region, observing that span-wise velocity profiles exhibited characteristics of low-speed boundary layer streaks rather than inflectional profiles typical of Kelvin-Helmholtz instability. Their observations revealed similarities to von Kármán vortex streets common in wake flows. Subsequent investigations by Merzari et al. [18] and Piot and Tavoularis [19] revealed an additional instability mechanism in rod-bundle flows, characterized by inflectional points on both sides of the gap, indicating Kelvin-Helmholtz-type instability.

Meyer [16] further elucidates the exceptional stability of vortical structures in rod-bundle flows, contrasting with typical growth-decay patterns observed in other instability mechanisms. Derksen [20] presents a comprehensive schematic of these vortical structures and associated cross-flow regions in Figure 3.4, highlighting their critical role in overall flow dynamics and large-scale, quasi-periodic coherent structures.

Meyer and Rehme [21] investigated vortex shedding in compound rectangular channels, demonstrating the formation of alternating, counter-rotating vortices. This shedding mechanism, analogous to the Kelvin-Helmholtz instability, is driven by velocity shear between inter-cylinder gaps and subchannels, resulting in substantial coherent structures.

In densely packed rod bundles, Baratto [22] and Chang and Tavoularis [23] demonstrated complex vortex street interactions. Tavoularis [24] introduced the concept of a "rod bundle vortex network," describing the intricate coupling of vortex sheets from adjacent gaps. This phenomenon remains an active area of research due to its significant impact on flow dynamics.

De Ridder [25] advanced the field through computational fluid dynamics (CFD) simulations of gap vortex streets and their interactions with rod bundles, providing crucial insights into fluid-structure coupling mechanisms. However, a detailed understanding of flow instability mechanisms and vortex interactions continues to present significant research challenges.

1.6. Research Formulation

As described in the above section, the discrepancy raises important questions about the accuracy and applicability of traditional heat transfer correlations developed based on pipe experiments in real-world reactor conditions. The potential uncertainties arising from this modelling assumption warrant further investigation, as does the possibility of improving these correlations for more accurate predictions.

Research Objective

The primary objective of this research project is to conduct a comparative study of heat transfer characteristics between a pipe and a typical PWR rod bundle. This will provide insights into current correlations' limitations and may suggest improvements for more accurate modelling of heat transfer in nuclear fuel assemblies.

Research Question 1

How does the geometric configuration of nuclear fuel assembly flow channels (subchannel and pipe) influence thermal-hydraulic heat transfer characteristics, and what are the underlying mechanisms driving these geometrically-induced variations?

Sub Research Question 1

To what extent do different geometrical representations (single subchannel and 2x2 subchannel) diverge in capturing the fundamental heat transfer mechanisms?

Sub Research Question 2

How do boundary conditions and thermal-hydraulic properties interact with geometric variations to modulate heat transfer performance?

2

Turbulence

This chapter delves into the complex realm of turbulence, a fundamental concept in fluid dynamics with significant implications for nuclear reactor thermal-hydraulics. The discussion encompasses three primary areas:

- **Governing equations:** An examination of the fundamental equations describing fluid flow and heat transfer, including the continuity equation, Navier-Stokes equations, and scalar conservation equation. The chapter presents both dimensional and normalized forms of these equations, laying the groundwork for Direct Numerical Simulation (DNS) studies.
- **Turbulent scales:** An exploration of the energy cascade concept, from large-scale eddies to Kolmogorov microscales. This section elucidates the multi-scale nature of turbulence and its implications for energy transfer and dissipation in fluid flows.
- **Evolution of turbulence modeling:** A historical perspective on the development of turbulence modeling techniques in subchannel domains, progressing from early Reynolds-Averaged Navier-Stokes (RANS) models to more advanced approaches like Unsteady RANS (URANS) and Large Eddy Simulation (LES).

Additionally, this chapter sets the stage for understanding the challenges and advancements in modeling turbulent flows within nuclear reactor geometries, particularly in subchannel domains with varying pitch-to-diameter ratios and flow conditions. It provides a foundation for the subsequent chapters' more detailed investigations into specific aspects of turbulent flow behavior in nuclear thermal-hydraulic.

2.1. Turbulent scales

Turbulence is characterized by fluid motion that is chaotic, random, and unsteady in nature. Turbulent flows are generally described in terms of eddies, ranging from large-scale eddies that are chaotic and anisotropic to small eddies where viscous forces dominate and energy is dissipated as heat. A key characteristic of turbulence is its ability to enhance mixing and transport of momentum compared to laminar flow. This advantage is applied in numerous industrial applications, particularly in nuclear reactors, where enhanced mixing and transport optimize heat transfer.

The concept of turbulent eddy scales is illustrated through the energy cascade, first proposed by Richardson in 1922, illustrated in figure 2.1. As Richardson poetically described:

"Big whorls have little whorls,
Which feed on their velocity;
And little whorls have lesser whorls,
And so on to viscosity
(in the molecular sense)."

Kinetic energy enters turbulence through production at the largest scales. Energy is then transferred to smaller scales (inviscid cascade) until it dissipates due to viscous forces, shown in Figure 2.2. These smaller scales are defined by Kolmogorov's scales. The largest eddy is characterized by size l_0 with a characteristic velocity scale of u_0 and timescale of t_0 . The rate of dissipation (ϵ) is determined by the transfer of energy from kinetic to internal heat. This process is called the energy cascade. The eddies

have an energy order of u_0^2 , and dissipation (ϵ) scales as u_0^3/l_0 , which is equal to the production that occurs at larger scales.

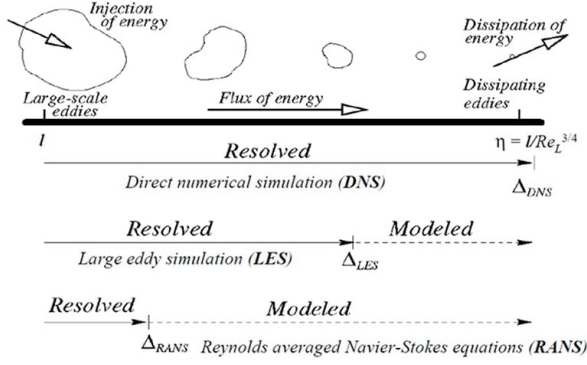


Figure 2.1: Turbulent scales [26]

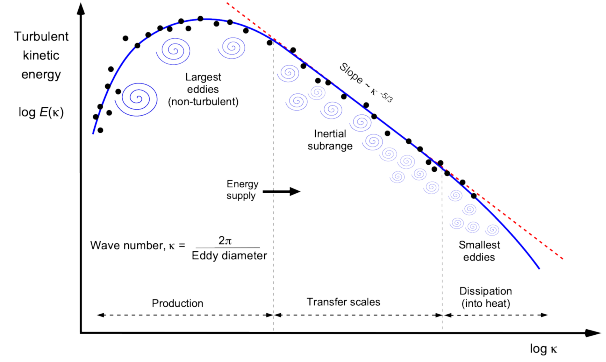


Figure 2.2: Energy Cascade $E(k)$ [27]

Kolmogorov scales are defined as η , u_η , and τ_η , representing length, velocity, and timescale for the smallest eddy, respectively. If ν is kinematic viscosity, then Kolmogorov's scales can be defined as:

$$\eta = (\nu^3/\epsilon)^{1/4} \quad (2.1)$$

$$u_\eta = (\nu\epsilon)^{1/4} \quad (2.2)$$

$$\tau_\eta = (\nu/\epsilon)^{1/2} \quad (2.3)$$

From Kolmogorov's first similarity hypothesis, the Reynolds number at these scales is always unity:

$$Re_\eta = \frac{\eta u_\eta}{\nu} = 1 \quad (2.4)$$

The ratios of the smallest Kolmogorov scales to the largest scales are given as:

$$\eta/l_0 \sim Re^{-3/4} \quad (2.5)$$

$$u_\eta/u_0 \sim Re^{-1/4} \quad (2.6)$$

$$\tau_\eta/\tau_0 \sim Re^{-1/2} \quad (2.7)$$

2.1.1. Kolmogorov Condition

The Kolmogorov length and time scales are essential criteria in mesh resolution studies to ensure that all relevant scales in turbulent flow are adequately resolved in both space and time. This criterion, as proposed by Pope [28], ensures that the mesh is sufficiently refined to capture the smallest eddies within the turbulence spectrum. The condition is expressed as:

$$\frac{\Delta}{\eta} \leq \pi \quad (2.8)$$

where Δ is (Cell Size) and η is Kolomrgov length scale. This condition ensures that the computational grid is refined enough to resolve the smallest turbulent structures, thereby capturing the full range of scales present in the flow.

2.2. Governing Equations

The continuity equation for an incompressible fluid is given by

$$\nabla \cdot \mathbf{u} = 0 \quad (2.9)$$

The momentum conservation is described by the Navier-Stokes equations. The equation for an incompressible Newtonian fluid is given by

$$\rho \frac{\partial \mathbf{u}}{\partial t} + \rho \mathbf{u} \cdot \nabla \mathbf{u} = -\nabla p + \mu \nabla^2 \mathbf{u} \quad (2.10)$$

The conservation equation for a passive scalar T is described by

$$\rho C_p \frac{\partial T}{\partial t} + \rho C_p \mathbf{u} \cdot \nabla T = k \nabla^2 T \quad (2.11)$$

The governing equations for Direct Numerical Simulation (DNS) are normalized using characteristic scales to obtain dimensionless forms. The normalization parameters are defined as follows:

$$u^* = \frac{u}{U_b} \quad t^* = \frac{t U_b}{D} \quad x^* = \frac{x}{D} \quad p^* = \frac{p}{\rho U_b^2} \quad T^* = \frac{T - T_0}{\delta T}$$

where U_b is the bulk velocity, D is the characteristic length, ρ is the fluid density, T_0 is a reference temperature, and δT is a characteristic temperature difference.

After normalizing the known parameters as given above, the new governing equations for Direct Numerical Simulation (DNS) are:

$$\nabla \cdot \mathbf{u}^* = 0 \quad (2.12)$$

$$\frac{\partial \mathbf{u}^*}{\partial t^*} + \mathbf{u}^* \cdot \nabla \mathbf{u}^* = -\nabla p^* + \frac{1}{Re} \nabla^2 \mathbf{u}^* \quad (2.13)$$

$$\frac{\partial T^*}{\partial t^*} + \mathbf{u}^* \cdot \nabla T^* = \frac{1}{Re Pr} \nabla^2 T^* \quad (2.14)$$

Equation (2.12) represents the normalized continuity equation, (2.13) is the normalized momentum equation, and (2.14) is the normalized energy equation. In these equations, Re is the Reynolds number and Pr is the Prandtl number, which emerge as the governing dimensionless parameters of the system.

These normalized equations form the basis for the DNS simulations, allowing for a more generalized analysis of the flow and heat transfer characteristics independent of specific physical dimensions.

2.3. Tubulent Kinetic Energy and it's Budget terms

Turbulent kinetic energy is a quantitative measure of the intensity of turbulence. The kinetic energy in classical mechanics is defined from Newton's second law of motion, and the equation is as follows:

$$KE = \frac{1}{2} m v^2 \quad (2.15)$$

where ' m ' represents the mass of the object and ' v ' represents the velocity of the object.

In turbulence, kinetic energy follows the same formula and is defined as the sum of the root mean square of each velocity fluctuation component. Since most quantities in turbulence are generally represented as independent of mass, kinetic energy in turbulence is represented as follows:

$$k = \frac{1}{2} (\overline{u'^2} + \overline{v'^2} + \overline{w'^2}) \quad (2.16)$$

where u' represents the velocity fluctuation, and the three components signify the direction of each velocity vector.

The transport equations for the Reynolds stresses are derived from the Navier-Stokes equations by ensemble averaging the equations, then deriving equations for the fluctuating stresses and ensemble averaging these equations. For incompressible turbulent flow, the transport equation is given by:

$$\frac{\partial k}{\partial t} + u_j \frac{\partial k}{\partial x_j} = -\overline{u'_i u'_j} \frac{\partial \bar{u}_i}{\partial x_j} - \nu \frac{\partial u'_i \partial u'_i}{\partial x_j \partial x_j} - \frac{\partial}{\partial x_j} \left[\frac{1}{2} \overline{u'_j p'} - \nu \frac{\partial k}{\partial x_j} + \frac{1}{2} \overline{u'_i u'_i u'_j} \right] \quad (2.17)$$

$$\frac{\partial k}{\partial t} + C_k = P_k - \epsilon_k + \pi_k + D_k + \tau_k \quad (2.18)$$

Where the terms on the left-hand side of the equation represent the time-rate of change and the advection (C_k) of k ; while the terms on the right-hand side represent production (P_k), dissipation (ϵ_k), pressure-diffusion (π_k), viscous diffusion (D_k) and turbulent diffusion (τ_k) of k .

The terms on the right-hand side of the above equation are defined as follows:

$P_k = -\overline{u'_i u'_j} \frac{\partial \bar{u}_i}{\partial x_j}$	Production rate
$\epsilon_k = \nu \frac{\partial u'_i \partial u'_i}{\partial x_j \partial x_j}$	Dissipation rate
$T_k = -\frac{1}{2} \overline{u'_i u'_i u'_j}$	Turbulent transport rate
$D_k = \nu \frac{\partial k}{\partial x_j}$	Viscous diffusion rate
$\Pi_k = -\frac{1}{2} \overline{u'_j p'}$	Velocity pressure-gradient term

We can obtain the equation in dimensionless form by multiplying the above equation by (ν/u_τ^4) (the wall-shear velocity, $u_\tau = \sqrt{\nu U_{,y}|_{wall}}$, and the kinematic viscosity, ν),

$$\frac{\partial k^+}{\partial t^+} + C_k^+ = P_k^+ - \epsilon_k^+ + \pi_k^+ + D_k^+ + \tau_k^+ \quad (2.19)$$

Here, the (+) superscript denotes inner- or wall-scaling.

2.4. Temperature Heat Flux and its Budget Terms

The transport equation for the thermal fluctuations can be expressed as:

$$\frac{\partial \overline{u'_i T'}}{\partial t} + u_j \frac{\partial \overline{u'_i T'}}{\partial x_j} = - \left(\overline{u'_i T'} \frac{\partial \bar{u}_i}{\partial x_j} + \overline{u'_j u'_i} \frac{\partial \bar{T}}{\partial x_j} \right) - (\nu + \alpha) \frac{\partial \overline{u'_i T'}}{\partial x_j} - \frac{1}{\rho} \overline{T'} \frac{\partial p'}{\partial x_j} - \frac{\partial \overline{u'_i u'_j T'}}{\partial x_j}, \quad (2.20)$$

$$+ \frac{\partial}{\partial x_j} \left[\nu \frac{\partial \overline{u'_i T'}}{\partial x_j} + \alpha \frac{\partial \overline{T' u'_i}}{\partial x_j} \right]$$

$$\frac{\partial \overline{u'_i T'}}{\partial t} + C_{i\theta} = P_{i\theta} - \epsilon_{i\theta} + \pi_{i\theta} + \tau_{i\theta} + D_{i\theta}. \quad (2.21)$$

Where the terms on the left-hand side of the equation represent the time-rate of change and the advection ($C_{i\theta}$) of Temperature Heat Flux (THF); while the terms on the right-hand side represent production ($P_{i\theta}$),

dissipation ($\epsilon_{i\theta}$), temperature-pressure-gradient-correlation ($\pi_{i\theta}$), turbulent diffusion ($\tau_{i\theta}$), and viscous diffusion ($D_{i\theta}$) of THF.

The terms on the right-hand side of the above equation are defined as follows:

$$\begin{aligned}
 P_{i\theta} &= - \left(\overline{u'_i T'} \frac{\partial \bar{u}_i}{\partial x_j} + \overline{u'_j u'_i} \frac{\partial \bar{T}}{\partial x_j} \right) && \text{Production rate} \\
 \epsilon_{i\theta} &= - (\nu + \alpha) \frac{\partial \overline{u'_i T'}}{\partial x_j} && \text{Dissipation rate} \\
 \tau_{i\theta} &= - \frac{\partial \overline{u'_i u'_j T'}}{\partial x_j} && \text{Turbulent Diffusion rate} \\
 D_{i\theta} &= \frac{\partial}{\partial x_j} \left[\nu \frac{\partial \overline{u'_i T'}}{\partial x_j} + \alpha \frac{\partial \overline{T'} u'_i}{\partial x_j} \right] && \text{Viscous diffusion rate} \\
 \pi_{i\theta} &= - \frac{1}{\rho} \overline{T' \frac{\partial p'}{\partial x_j}} && \text{Temperature-pressure-gradient term}
 \end{aligned}$$

The dimensionless form may be obtained by multiplying the above equation by $(\nu/u_\tau^3 T_\tau)$ gives:

$$\frac{\partial \overline{u'_i T'}^+}{\partial t^+} + C_{i\theta}^+ = P_{i\theta}^+ - \epsilon_{i\theta}^+ + \pi_{i\theta}^+ + \tau_{i\theta}^+ + D_{i\theta}^+. \quad (2.22)$$

2.5. Numerical simulation for Subchannel Domains

Modeling turbulent flows presents significant challenges in fluid dynamics research due to their inherently chaotic and random nature. The study of turbulence in subchannel domains is particularly crucial in nuclear thermal-hydraulics, where simulation fidelity directly impacts prediction accuracy. This section examines the evolution of turbulence modeling approaches in subchannel geometries, focusing on their capabilities across varying pitch-to-diameter ratios and Reynolds numbers under diverse boundary conditions.

2.5.1. Early Benchmarks and RANS Models

Smith and Johnson [29] established fundamental relationships between mesh refinement, turbulence models, and numerical schemes in their benchmark study. Their analysis demonstrated that Reynolds-Averaged Navier-Stokes (RANS) models could predict pulsation flow under specific conditions, though with notable limitations.

In a subsequent investigation, Bieder and Anderson [30] explored these limitations through investigations of isotropic and anisotropic turbulence. While RANS models achieved acceptable accuracy in isotropic turbulence prediction, they exhibited significant deficiencies when modeling anisotropic turbulence beyond ten hydraulic diameters downstream, highlighting the need for more sophisticated modeling approaches.

2.5.2. Advancements with URANS

Merzari and Ninokata [18] validated Unsteady RANS (URANS) simulations for staggered pin arrangements through comparisons with large eddy simulation (LES) data and experimental measurements. Their work demonstrated URANS's potential to balance computational efficiency with accuracy in specific subchannel configurations.

Building on these findings, Podila and Rao [31] utilized data from the OECD/NEA-organized CFD benchmarking exercise to evaluate URANS performance in a 5x5 square bundle rod arrangement. Their results revealed accurate predictions of flow velocity distributions while consistently underestimating turbulence intensity, illustrating both the capabilities and limitations of URANS modelling.

2.5.3. Large Eddy Simulation (LES) Approaches

Tiselj and Mikuz [32] advanced subchannel turbulence analysis through their investigation of a 5x5 rod bundle using the Wall-Adapting Local Eddy-viscosity (WALE) model in OpenFOAM. While their study showed improvements over RANS and URANS in mean velocity flow prediction, the WALE model demonstrated limitations in capturing second-order turbulence statistics when compared with MATiS-H experimental measurements.

Lakehal [33] conducted high-resolution LES studies in single subchannel domains, achieving first-order turbulence statistics comparable to pipe DNS results. Their investigation revealed distinct Reynolds number characteristics between gap regions and domain cores. However, the absence of second-order statistical validation indicates a crucial gap in current modeling capabilities.

2.5.4. The Path Forward: DNS and Beyond

Current research trends indicate that while RANS, URANS, and LES models have contributed significantly to subchannel turbulence understanding, they remain insufficient for fully characterizing these complex, multi-scale flows. This limitation has motivated increased interest in Direct Numerical Simulation (DNS) methodologies.

Contemporary investigations have expanded to include surface roughness effects, fluid-structure interaction (FSI), and spacer grid impacts. Despite these advances, fundamental questions regarding physical and heat transfer characteristics within simplified subchannel domains persist, necessitating continued investigation through refined analytical approaches.

Computational Model

This chapter presents the comprehensive computational methodology for investigating thermal-hydraulic phenomena in nuclear reactor geometries. The discussion focuses on five primary areas:

- **Nek5000 Spectral Element Solver:** Explores the high-fidelity computational fluid dynamics code with its unique spectral element method combining geometric flexibility and high-order accuracy.
- **Computational Domains:** Analyzes three numerical domains: Pipe, Square Subchannel, and 2×2 Subchannel, highlighting strategic geometric modeling approaches aligned with PWR design standards.
- **Mesh Generation and Resolution:** Examines computational mesh design, emphasizing near-wall resolution and grid refinement techniques to capture boundary layer physics accurately.
- **Temperature Field Modeling:** Investigates scalar transport through variation of Prandtl numbers and boundary condition types to comprehensively characterize heat transfer behavior.
- **Boundary and Initial Conditions:** Details computational boundary strategies and pseudo-random perturbation techniques to trigger turbulent transition while maintaining flow continuity.

By synthesizing advanced numerical techniques, precise geometric modeling, and solver implementations, this chapter establishes a robust computational framework for high-fidelity thermal-hydraulic investigations. The methodology provides unprecedented insights into fluid dynamics within nuclear reactor subchannel geometries, bridging fundamental research with practical thermal-hydraulic design considerations.

3.1. Nek5000 - SEM solver

Nek5000 is a spectral element code developed at Argonne National Laboratory [34], designed explicitly for high-fidelity computational fluid dynamics simulations. The code employs a spectral element method (SEM), which combines the geometric flexibility of finite elements with the high-order accuracy of spectral methods.

The spatial discretization in Nek5000 is handled through the decomposition of the computational domain into hexahedral elements, within which the solution is represented by high-order Lagrange polynomials based on Gauss-Lobatto-Legendre (GLL) quadrature points. For temporal discretization, the code implements a semi-implicit time-stepping scheme, treating the nonlinear convective terms explicitly through an n th-order extrapolation and back difference formula (EXT n -BDF n) while handling the viscous and pressure terms implicitly. Additionally, the code employs an Operator Integration Factor Splitting (OIFS) method that provides an alternative approach to solving the Navier-Stokes equations by decoupling the linear and nonlinear terms. This method significantly reduces the time-stepping constraints while maintaining solution stability, allowing for timesteps approximately 5-10 times larger than those permitted by traditional CFL criteria without compromising accuracy.

3.1.1. Present Simulation

This study encompasses a comprehensive investigation across three meticulously constructed numerical domains: the canonical "Pipe" configuration, the "Square Subchannel" geometry, and the "2×2 Subchannel" architecture. The Pipe case serves a multifaceted purpose, it provides a comprehensive platform for

comparative analysis of flow and heat transfer characteristics, leveraging the well-established Nusselt number correlations that form the cornerstone of Pressurized Water Reactor (PWR) thermal-hydraulic design and optimization. Concurrently, the pipe configuration enables rigorous validation of numerical schemes, simulation parameters and convergence methodologies through direct comparison with available Direct Numerical Simulation (DNS) reference data.

Following this validation, simulations will be performed using Nek5000 as a tool to solve incompressible Navier-Stokes equations as mentioned in section 2.2 for the Square Subchannel and 2x2 Subchannel configurations, and later investigated with Pipe geometry.

The pipe case simulation employs an O-grid mesh, utilizing a third-order Backwards differentiation formula (BDF3) for temporal discretization. The case maintains numerical stability through a CFL constraint of less than 0.5. The square subchannel case implements identical solver parameters as the pipe case, employing the BDF3 time integration scheme while adhering to the same CFL criterion. The 2x2 subchannel configuration utilizes a second-order BDF scheme with $CFL < 1$, primarily to speed up with minimal reduction in data quality. Additionally, the 2x2 subchannel implements the Operator-Integration-Factor Splitting (OIFS) method, which offers enhanced numerical efficiency by decoupling the linear and nonlinear terms. This implementation permits larger timestep sizes, approximately 5-10 times that of traditional CFL criteria, without compromising solution accuracy. The discretization schemes and solver parameters for the subchannel and Pipe DNS are configured as follows:

Feature	Specification
<i>Temporal Discretization</i>	2nd - 3rd-order Backwards Differentiation (BDF2/BDF3) Variable timestep with target CFL = 0.5-1.0
<i>Spatial Discretization</i>	Dealiasing: Enabled (3/2 rule)
<i>Solver Parameters</i>	Pressure preconditioner: Semi-geometrical multigrid (HYPRE)
<i>Solver Tolerances</i>	Pressure tolerance: (1×10^{-6}) Velocity tolerance: (1×10^{-7})

Table 3.1: Numerical schemes and parameters in Nek5000

The pressure solver uses a semi-geometrical multigrid preconditioner from the HYPRE library while maintaining strict tolerances for both pressure and velocity solutions.

3.2. Computational Domain

The implementation of accurate Direct Numerical Simulation (DNS) requires meticulous attention to the initial case setup and geometry definition. While the geometries considered in this study are relatively straightforward, necessitating only a few key parameters, the computational intensity and time-consuming nature of DNS simulations make it imperative to establish precise initial conditions. Any inadequacies or oversights in the preliminary setup can propagate through the simulation, potentially compromising the accuracy of results and proving challenging to rectify in subsequent stages.

3.2.1. Pipe

The diameter (D) was normalized to unity for the pipe configuration, with the axial length extending to $12.5D$ (approximately $4\pi D$ [35]). This length is reported to be sufficient to resolve the large-scale turbulent scales at the presently investigated Reynolds number.

3.2.2. Subchannel

The geometric configuration under investigation is a rectangular bundle rod arrangement prevalent in contemporary nuclear reactor cores. As elaborated in Section 1.2, these arrangements are characterized by various geometric configurations and critical design parameters, including P/D and W/D ratios. This investigation focuses specifically on the bundle rod core, excluding wall effects.

The study adopts industrial-standard specifications [36] with a P/D ratio of 1.3263, incorporating a fuel rod diameter (D) of 9.5mm and a fuel rod pitch (P) of 12.6mm typical of a PWR. This standardization facilitates future experimental validation without necessitating geometric modifications. The geometry and flow parameters were subsequently normalized to a hydraulic diameter (D_h) of unity, with the modified specifications detailed in Table 3.2.

Parameters	Original Case	Modified Case
Fuel rod diameter, D	9.5 mm	0.8066 m
Fuel rod pitch, P	12.6 mm	1.0698 m
P/D ratio	1.3263	1.3263
Hydraulic diameter, D_h	11.78 mm	1.00 m

Table 3.2: Subchannel Geometry Parameters: Original and Modified Specifications

In a departure from conventional methodologies that typically focus on the interior subchannel domain bounded by quadrants of four adjacent rods, this study adopts a distinctive approach for the single subchannel case. The computational domain encompasses the region surrounding a single rod rather than the traditional approach of modeling the interstitial space between four partial rods. While both approaches should theoretically yield identical results under ideal conditions, our chosen geometry allows for a more focused examination of the flow characteristics in the immediate vicinity of a single fuel rod.

The 2×2 subchannel configuration extends the single subchannel model to include four interconnected traditional interior subchannels. This expanded domain captures the flow characteristics around a central rod while accounting for the influence of eight neighbouring rods, enabling a more comprehensive analysis of inter-subchannel mixing phenomena.

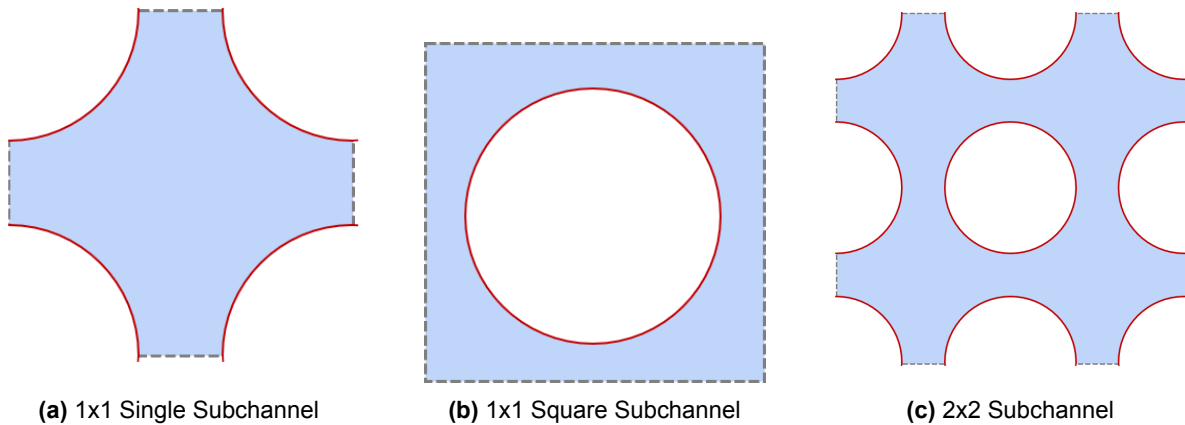


Figure 3.1: Comparison of different subchannel geometry

Both configurations were analyzed at Bulk Reynolds number (Re_b) 5300 (friction Reynolds number (Re_τ) \sim 380) and extend axially to $48D_h$ to adequately capture the gap vortex street phenomena. The investigation is deliberately constrained to a single P/D ratio and Reynolds number for both geometric cases, facilitating direct comparisons and allowing for a deep dive into the specific flow regime of interest. This focused approach establishes a robust baseline for future studies that may incorporate additional variables or explore a broader range of operating conditions.

3.3. Mesh

In the present work, computational meshes have been designed using the pre-processing software GAMBIT version 2.4.6. The resulting meshes are converted to Nek5000 format using an in-house utility.

3.3.1. Pipe

The fundamental mesh architecture comprises four equi-angularly distributed blocks along the pipe circumference, complemented by a central core block. The structured mesh generation methodology employed a boundary-first approach, initiating from the pipe's peripheral geometry and progressing inward. This approach ensures superior control over near-wall mesh characteristics, which is crucial for the accurate resolution of boundary layer phenomena.

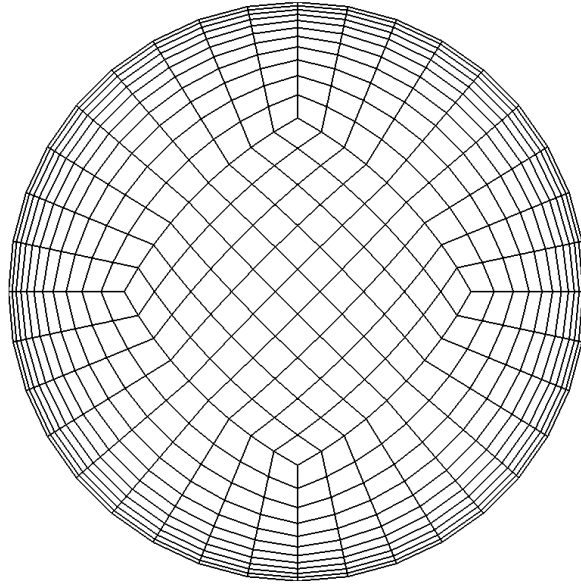


Figure 3.2: Base Mesh of Pipe case (N=1)

To ensure accurate resolution of the near-wall flow physics, careful consideration was given to the dimensionless wall distance (y^+) during the mesh design. The parameters used to define the mesh for the pipe configuration for polynomial order of 7 are provided in the table below:

Parameters	Pipe
Elements (cross-section)	477
Number of layers	107
Total number of elements	51,039
Number of GLL points (N = 7)	26.13×10^6

Table 3.3: Mesh Specifications and Element Distribution for Pipe Geometry

The grid resolution was validated through a comparative analysis of cell dimension ratios, specifically between the smallest and largest cells in the domain, following the methodology established by El Khoury and Philipp Schlatter [37]. Table 3.4 compares the grid resolution parameters in wall units between the present study and the reference data. These parameters, particularly for a $Re_\tau \sim 180$ pipe flow, were carefully selected to capture the required resolution in both the near-wall and bulk regions.

The non-dimensional grid spacing parameters (Δz^+ , Δr^+ , $\Delta\theta_w^+$, $\Delta\theta_b^+$) were evaluated using local wall units, defined as:

$$\Delta z^+ = \frac{\Delta z u_\tau}{\nu} \quad (3.1)$$

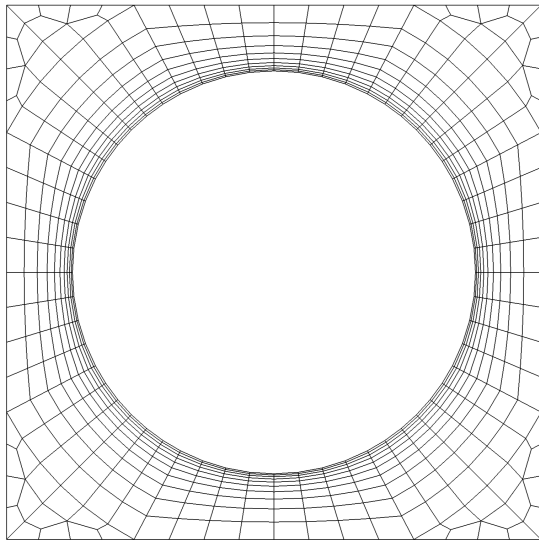
where u_τ represents the friction velocity and ν denotes the kinematic viscosity.

Parameter	Present DNS		Reference DNS	
	Min	Max	Min	Max
Streamwise spacing (Δz^+)	2.7	8.9	3.03	9.91
Radial spacing (Δr^+)	0.14	3.6	0.14	4.44
Azimuthal spacing at wall ($\Delta \theta_w^+$)	2.0	6.6	1.5	4.9
Azimuthal spacing in bulk ($\Delta \theta_b^+$)	1.1	3.6		

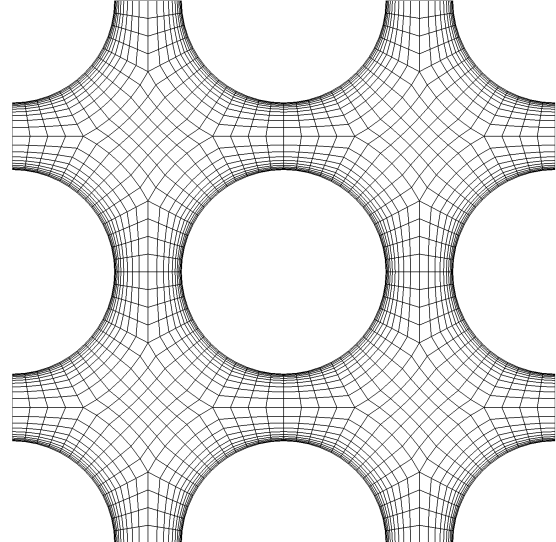
Table 3.4: Grid resolution parameters comparing present DNS with reference data from El Khoury et al.2013. Values are presented as minimum and maximum in wall units.

3.3.2. Subchannel

The mesh for the subchannel cases was generated using a similar approach to the pipe case but with modifications to account for the different geometrical configurations. The fundamental mesh architecture comprises structured blocks that conform to the subchannel geometry, ensuring accurate resolution of the flow physics.



(a) Square Subchannel



(b) 2x2 Subchannel

Figure 3.3: Base Mesh of Subchannel Cases (N=1)

For the subchannel cases, the dimensionless wall distance (y^+) was also carefully considered in the mesh design to accurately resolve the near-wall flow physics. The parameters used to define the mesh for the subchannel cases for polynomial order of 5 are provided in the table below:

Parameters	Square subchannel	2x2 subchannel
Elements (cross-section)	616	2384
Number of layers	439	439
Total number of elements	270,424	1,046,576
Number of GLL points (N = 5)	58.41×10^6	226.06×10^6

Table 3.5: Mesh Specifications and Element Distribution for Subchannel Cases

The spatial discretization characteristics are quantified through dimensionless cell-size ratios, encom-

passing the entire computational domain from minimum to maximum cell dimensions, as presented in Table 3.6. This methodological approach strictly adheres to the framework established by El Khoury and Philipp Schlatter [37] study for pipe flow configurations. The grid resolution parameters were meticulously optimized Reynolds number, ensuring adequate spatial resolution in both the viscous sublayer and bulk flow regions of the subchannel geometry.

The wall-unit calculations were performed for a 2×2 subchannel configuration, which exhibits analogous near-wall characteristics to the square subchannel case due to geometric similarities in the wall-adjacent regions. This equivalence in local flow physics justifies the extension of the resolution criteria from the reference pipe flow to the present subchannel analysis.

Parameter	Subchannel (N = 5)	
	Min	Max
Streamwise spacing (Δz^+)	4.9	12.0
Radial spacing (Δr^+)	0.17	5.56
Azimuthal spacing at wall ($\Delta \theta_w^+$)	2.0	4.9
Azimuthal spacing in bulk ($\Delta \theta_b^+$)	3.0	7.2

Table 3.6: Grid resolution parameters for the 2x2 subchannel (N = 5) case. Values are presented as minimum and maximum in wall units.

These structured mesh configurations, along with the careful consideration of the near-wall mesh characteristics, ensure the accurate resolution of the complex flow phenomena within the subchannel geometries.

3.4. Temperature fields

Temperature fields were introduced in the model to capture heat transfer characteristics. Two Prandtl numbers (Pr) were chosen to represent different fluid properties: $Pr = 1$, typical for water, and $Pr = 0.025$ at PWR conditions, representative of liquid metals. The thermal diffusivity (α) for each Prandtl number was computed based on the following relationship:

$$\alpha = \frac{\nu}{Pr} \quad (3.2)$$

where ν is the kinematic viscosity. The resulting thermal diffusivity values are presented in Table 3.7.

To evaluate different scalar qualities and their influence on heat transfer, two types of lateral surface boundary conditions were applied for each Prandtl number: Dirichlet (iso-temperature) and Neumann (iso-heat flux). This configuration created four distinct scalar fields (T_1 to T_4), each defined by a unique combination of Prandtl number and boundary condition. These four scalars allow a comprehensive analysis of heat transfer under varied conditions, enabling insights into both temperature-driven (Dirichlet) and flux-driven (Neumann) behaviour across different Prandtl numbers. The details of each scalar quantity are summarized in Table 3.7.

Scalar	Prandtl Number (Pr)	Boundary Condition	Thermal Diffusivity ($\alpha = 1/RePr$)
T_1	0.025	Dirichlet	7.55×10^{-3}
T_2	1	Dirichlet	1.89×10^{-4}
T_3	0.025	Neumann	7.55×10^{-3}
T_4	1	Neumann	1.89×10^{-4}

Table 3.7: Scalar Quantities Defined by Prandtl Number and Boundary Conditions

This approach enables an examination of passive scalar transport under both fluid types, highlighting the effects of different thermal diffusivities and boundary conditions on the flow and heat transfer behaviour within the simulation.

3.5. Boundary Conditions

The specification of boundary conditions for pipe flow configurations presents a more straightforward case compared to subchannel geometries. In cylindrical pipe domains, the lateral surface area is characterized by temperature-controlled boundary conditions, implementing either Dirichlet or Neumann conditions. The Dirichlet condition prescribes a constant temperature distribution ($T = T_{\text{wall}}$) along the wall surface, while the Neumann condition specifies a constant heat flux ($q'' = \text{constant}$) normal to the wall. To simulate infinite-length conditions, periodic boundary conditions are imposed at the inlet and outlet surfaces, establishing:

$$\phi(x, y, 0) = \phi(x, y, L) \quad (3.3)$$

where ϕ represents any flow variable (velocity, temperature, or pressure), and L , denotes the axial length of the computational domain.

For subchannel configurations, the boundary conditions maintain similar fundamental principles while incorporating additional complexity. The surfaces adjacent to the fuel pin/rod implement temperature-controlled conditions, either through Dirichlet ($T = T_{\text{pin}}$) or Neumann ($q''_{\text{pin}} = \text{constant}$) specifications. The axial periodicity remains consistent with the pipe case, employing Equation 3.3 to simulate infinite-length behaviour.

A distinguishing feature of subchannel analyses lies in the treatment of lateral boundaries. For square subchannel geometries, periodic conditions are imposed on all four lateral walls, establishing:

$$\phi(0, y, z) = \phi(W, y, z) \quad (3.4)$$

$$\phi(x, 0, z) = \phi(x, H, z) \quad (3.5)$$

where W and H represent the width and height of the subchannel cross-section, respectively. This formulation ensures the continuity of flow variables across computational boundaries, effectively modelling the repeating nature of subchannel arrangements in nuclear fuel assemblies (Figure 3.4a).

The boundary condition implementation for 2×2 subchannel configurations, which represents an interior subchannel domain, the periodic conditions are established exclusively at the interior subchannel gaps, as illustrated in Figure 3.4b. This modification more accurately represents the local flow coupling between adjacent subchannels while maintaining the physical integrity of the rod bundle arrangement.

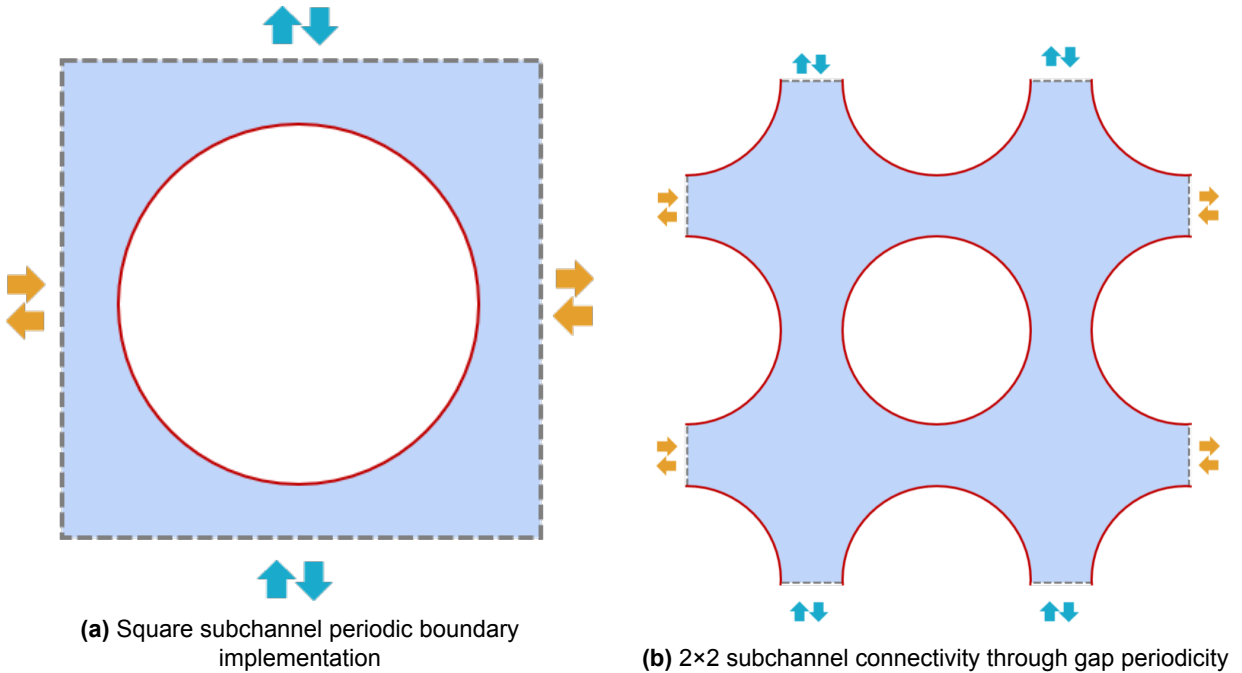


Figure 3.4: Schematic representation of periodic boundary conditions for subchannel configurations

The implementation of these boundary conditions facilitates accurate numerical simulation of both isolated and coupled subchannel flows, providing a framework for detailed thermal-hydraulic analysis of nuclear fuel assemblies.

3.6. Initial Conditions

For both pipe and subchannel configurations, random perturbations are introduced through a set of trigonometric functions in the Nek5000 user script. These functions, while deterministic in form, create pseudo-random disturbances in the flow field due to their interacting periodic components.

The streamwise velocity component (u_z) combines a near-wall turbulent profile approximation ($1 - y^8$) with periodic perturbations:

$$u_z = \frac{9}{8}(1 - y^8) - 10.0\pi \cos(z) \sin(\pi y) \sin(x) \quad (3.6)$$

The cross-stream velocities (u_x, u_y) are defined as:

$$u_x = 5.0\pi \cos(z) \sin(z) \sin(\pi y) \quad (3.7)$$

$$u_y = 5.0 \cdot 0.1(1 + \cos(\pi y)) \sin(x) \quad (3.8)$$

3.7. Post-Processing Approaches

This section details the post-processing methodologies implemented to extract and analyze the results. Three-dimensional field data was first averaged spatially and temporally to produce a two-dimensional field for ease of data extraction and visualization. Temporal averaging was conducted using flow-through time (FTT) metrics, as defined in Section 4.2, ensuring statistical convergence of the data.

For the pipe configuration, azimuthal averaging was applied to the two-dimensional averaged field data to further reduce it to a one-dimensional profile, effectively capturing radial variations along the pipe length. Similarly, for the square subchannel and 2×2 subchannel configurations, data was averaged across a single unit cell, as explained in Section 5.1, to obtain representative one-dimensional profiles of flow and heat transfer characteristics.

These post-processing methodologies facilitated a direct comparison between the square subchannel and 2×2 subchannel geometries, as well as a comprehensive comparison between the pipe and subchannel configurations.

4

Pipe

This chapter presents a comprehensive analysis of turbulent pipe flow through high-fidelity Direct Numerical Simulation (DNS), exploring critical aspects of flow resolution, statistical convergence, and thermal transport characteristics. The investigation focuses on unraveling the complex dynamics of pipe flow with particular emphasis on:

- Polynomial order resolution and its impact on turbulent flow representation
- Temporal convergence of statistical calculations for velocity and temperature fields
- Validation against established DNS databases for pipe flow
- Detailed examination of turbulent kinetic energy and heat transfer mechanisms
- Exploration of thermal boundary conditions and their influence on flow characteristics
- Comprehensive analysis of Nusselt number behavior across different Prandtl numbers

By systematically addressing these elements, the study aims to provide nuanced insights into turbulent pipe flow dynamics, with fundamental contributions to understanding scalar transport and fluid mechanics in complex thermal systems. The methodology leverages high-resolution spectral element methods to rigorously investigate the fundamental physics of turbulent flow, offering a detailed characterization of flow and scalar transport mechanisms that extends the current understanding of turbulent heat transfer phenomena.

4.1. Resoluion

This investigation analyzes the influence of polynomial order on solution fidelity within the context of Direct Numerical Simulation (DNS), following the methodological framework established by Ninokata [38].

Three polynomial orders were investigated: $N = 3$, 5, and 7, representing low, medium, and high-order approximations, respectively. The upper bound of $N = 7$ was established based on computational cost considerations, as higher-order approximations proved prohibitively expensive for the available computational resources.

Figure 4.1 presents instantaneous velocity field distributions across the pipe cross-section for varying polynomial orders:

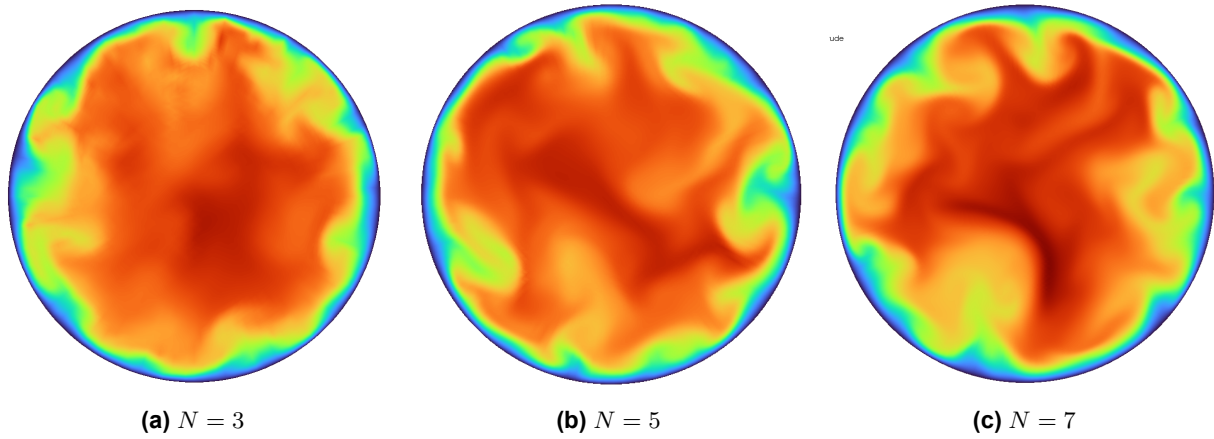


Figure 4.1: Comparative visualization of instantaneous velocity field distributions at varying polynomial orders ($t^* = 1203$).

To quantitatively assess the capacity of different polynomial orders to resolve small-scale turbulent structures, both first and second-order velocity statistics were analyzed. The normalized axial velocity profiles ($u^+ = u/u_\tau$) demonstrated remarkable consistency across all polynomial orders, with relative L^2 norm errors below 0.25% when compared to the reference data provided by [37], as illustrated in Figure 4.2.

The second-order statistics, specifically the normalized turbulent kinetic energy ($k^+ = k/u_\tau^2$) profiles versus wall-normal distance (y^+), revealed subtle but important differences between polynomial orders. While $N = 5$ and $N = 7$ demonstrated virtually identical results, $N = 3$ exhibited minor deviations, though these differences were so small as to be indiscernible in the plot, remaining below 1% in terms of L^2 norm relative error, as shown in Figure 4.3.

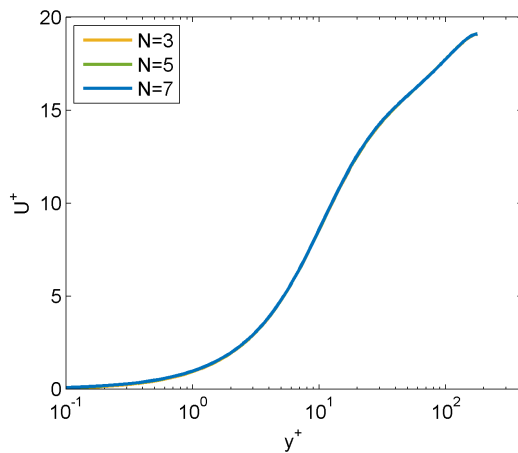


Figure 4.2: Wall-normal distribution of normalized mean axial velocity (u^+) for varying polynomial orders

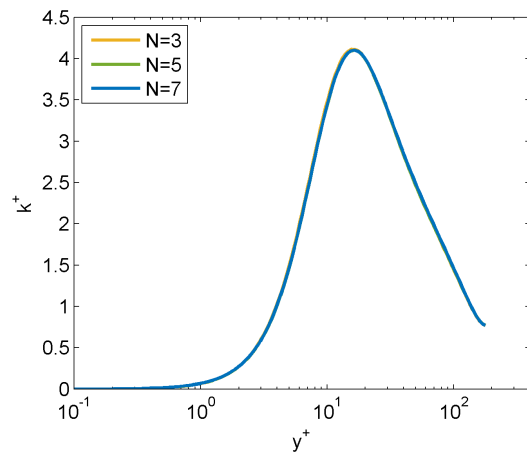


Figure 4.3: Wall-normal distribution of normalized turbulent kinetic energy (k^+) for varying polynomial orders

While all polynomial orders demonstrated satisfactory resolution characteristics, $N = 7$ exhibited superior performance in resolving the Kolmogorov microscales. Figure 4.4 presents the Kolmogorov length-scales from the resolved turbulent kinetic energy dissipation rate for $N = 7$. The resolution satisfies Pope's criterion [28], which stipulates that the grid spacing must be of order $O(\eta)$, where η represents the local Kolmogorov length scale:

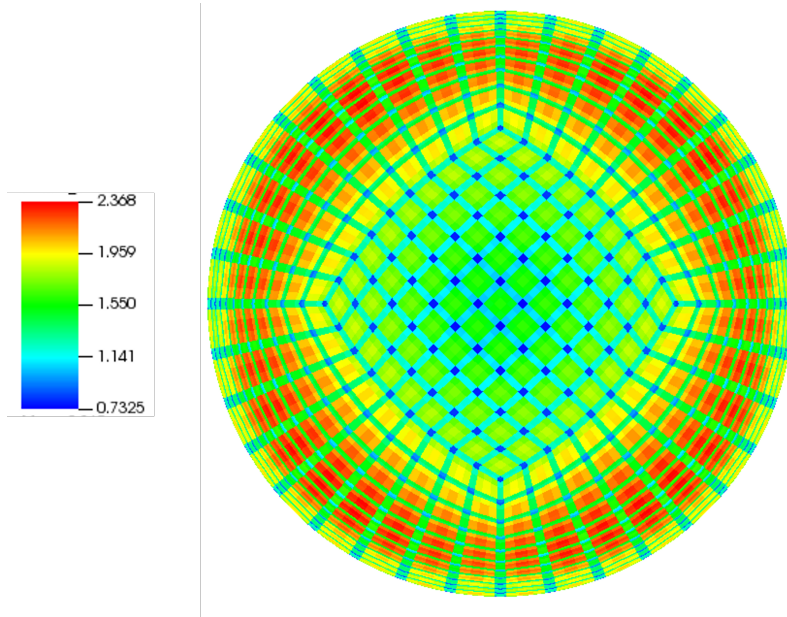


Figure 4.4: Distribution of cell size normalized by kolmogorov length scale ($\frac{\Delta}{\eta}$) for $N = 7$

A quantitative summary of the resolution study is presented in Table 4.1, which demonstrates the relative L^2 norm errors for different polynomial orders with respect to the highest-order case ($N = 7$).

First Order (u^+)	Second Order (k^+)
< 0.25%	< 1.0%

Table 4.1: Relative L^2 norm errors for velocity statistics compared to the reference data [37]

4.2. Convergence of statistical calculation

Based on the resolution analysis, a polynomial order of $N = 7$ has been established as optimal, providing the requisite balance between accuracy and computational efficiency for the pipe flow configuration. The temporal convergence analysis employs multiple characteristic time metrics, including the flow-through time (FTT), which represents the time required for fluid particles to traverse the computational domain, along with associated normalized time, eddy turnover time scales and wall-scaled as presented in Table 4.2.

FTT	$\frac{tU_b}{D}$	$\frac{tu_\tau}{R}$	$\frac{tu_\tau^2}{\nu}$
12	150	20.6	3710.5
24	300	41	7448
36	450	61.6	11,144
48	600	82	14,865
60	750	102.6	18,587

Table 4.2: Flow-through times (FTTs) and corresponding normalized time scales

4.2.1. Velocity Statistics

The convergence assessment was conducted by analysing first- and second-order statistics, utilizing spatial and temporal averaging over multiple averaging periods, as shown in Table 4.2. This systematic approach enables comprehensive characterization of the flow field evolution and ensures statistical reliability of the results.

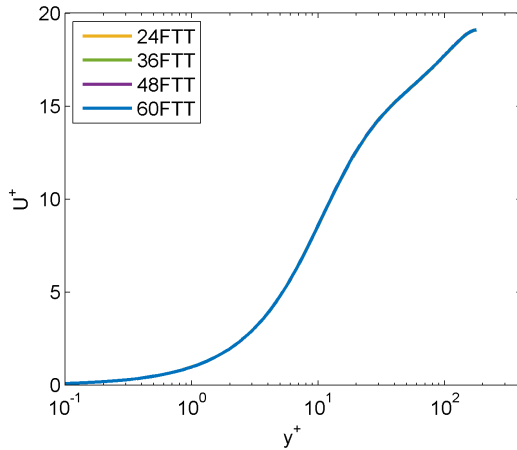


Figure 4.5: Axial velocity (u_z) plotted against y^+ for different averaging periods.

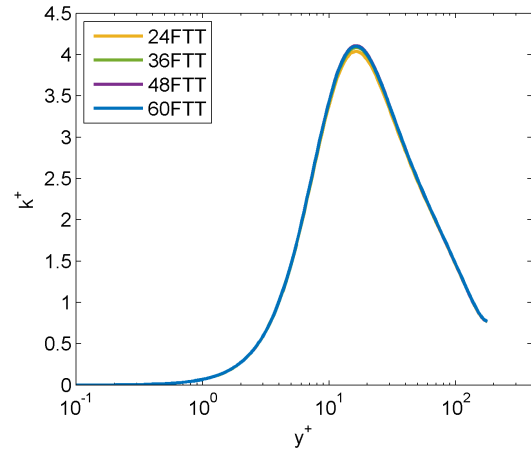


Figure 4.6: Kinetic Energy plotted against y^+ for different averaging periods.

Figure 4.5 presents the first-order statistics, precisely the mean axial flow velocity (U_z) normalized by the mean shear velocity (u_τ). The profiles are plotted against wall distance (y^+) for various averaging periods, demonstrating excellent agreement with established near-wall, log-law, and outer region velocity distributions. The L^2 norm error remained below 0.1% across all averaging periods, indicating robust convergence of first-order statistics.

Figure 4.6 illustrates the second-order statistics, characterized by the kinetic energy (k) normalized by the square of the shear velocity (u_τ^2), plotted against wall distance (y^+). As anticipated, second-order statistics exhibit longer convergence times compared to first-order quantities. Nevertheless, the L^2 norm error remained below 1% across all flow-through times, demonstrating satisfactory convergence. Additional convergence analyses, including temperature statistics, are presented in Appendix A (Figures 1, 2, and 3).

4.3. Validation

The preceding analyses have established optimal parameters for the numerical simulation: a polynomial order of $N = 7$ for adequate resolution of Kolmogorov microscales and averaging period of 60 FTTs for statistical convergence of quasi-steady state. The present section focuses on validation against the established DNS database by El Khoury [37] for pipe flow at $Re_b = 5300$.

4.3.1. Velocity Statistics

Figures 4.7 and 4.8 present the first-order and second-order statistics at an averaging period of 60 FTT compared with reference data. The results demonstrate exceptional agreement, exhibiting L^2 norm errors of less than 0.15% and 0.5% for first-order and second-order statistics, respectively.

Figure 4.9 presents the Turbulent kinetic energy (TKE) budget terms, encompassing production, dissipation, convection, and turbulent diffusion, evaluated at an averaging period of 60 FTTs across the wall-normal direction (y^+). Reference data is represented by dotted lines using consistent colour coding. The excellent agreement between computed and reference profiles provides comprehensive validation of statistical convergence and the numerical methodology employed.

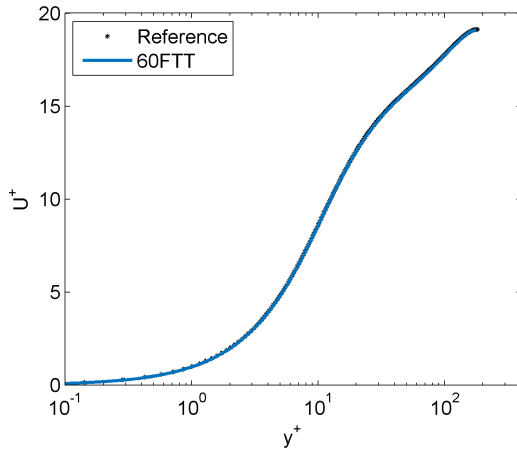


Figure 4.7: Axial velocity (u_z) plotted against y^+ for last averaging periods compared to reference [37].

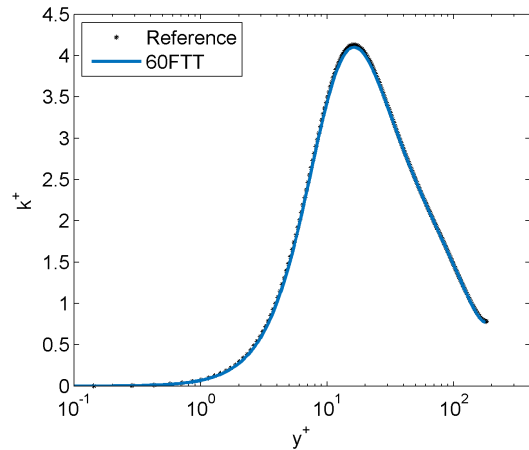


Figure 4.8: Kinetic Energy plotted against y^+ for last averaging periods compared to reference [37].

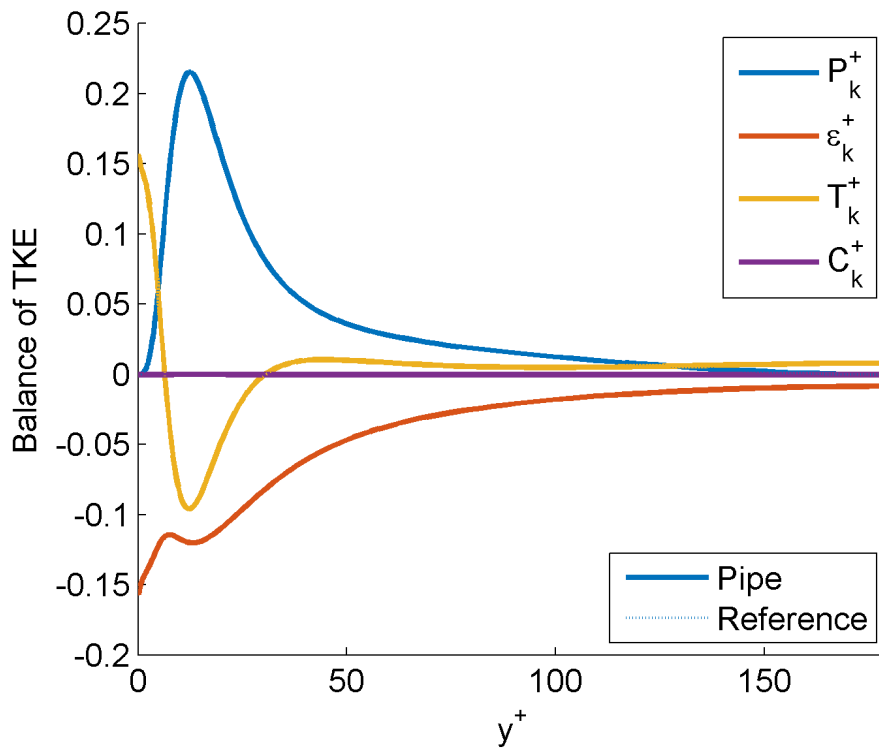


Figure 4.9: Turbulent Kinetic Energy (TKE) Budget terms at an averaging period of 60 FTTs plotted against wall distance (y^+) compared to the reference [37].

4.3.2. Temperature Statistics

Herein, a comprehensive methodology was employed to analyze the heat transfer characteristics through examination of first and second-order scalar temperature statistics. This analysis encompasses mean temperature, root-mean-square (RMS) temperature, and streamwise turbulent heat flux (THF).

The friction temperature, T_τ , is a characteristic temperature scale frequently employed in the study of wall-bounded turbulent flows, particularly in thermal and fluid dynamics analyses. It is defined in terms of

the wall heat flux (q_w), the fluid density ($\rho = 1$), the specific heat at constant pressure (c_p), and the friction velocity (u_τ), as follows:

$$T_\tau = \frac{q_w}{\rho c_p u_\tau}$$

Where:

- q_w : Wall heat flux
- ρ : Fluid density
- c_p : Specific heat at constant pressure
- $u_\tau = \sqrt{\frac{\tau_w}{\rho}}$: Friction velocity, where τ_w is the wall shear stress

In turbulent flow studies, T_τ provides a normalization scale for temperature differences, analogous to the role of u_τ in velocity normalization. Its usage simplifies the analysis of temperature fields in turbulent systems by scaling temperature variations relative to the flow's inherent thermal and dynamic characteristics.

In wall-bounded flows, such as pipe flows or channel flows, the mean temperature is normalized using the "excess temperature" and analyzed as a function of the wall-normal distance in wall units ($y^+ = \frac{y u_\tau}{\nu}$).

The excess temperature is defined as:

$$\theta = \frac{T - T_w}{T_\tau}$$

Where:

- T : Local fluid temperature
- T_w : Wall temperature
- T_τ : Friction temperature

Excess temperature provides a universal framework to compare thermal behavior across different flow conditions (e.g., Reynolds number, Prandtl number). Normalizing temperature by T_τ removes dependencies on specific heat flux or material properties, enabling direct comparisons of thermal profiles.

Figures 4.10 and 4.11 depict the excess temperature (θ), normalized with friction temperature (T_τ), plotted against wall distance (y^+) for the final averaging period. Figure 4.10 illustrates the temperature distribution at Prandtl number (Pr) = 0.025, characterized by two boundary conditions: a Dirichlet condition (θ_1) prescribing constant wall temperature and a Neumann condition (θ_3) enforcing constant wall heat flux.

For $Pr = 0.025$, representative of liquid metals, thermal diffusivity significantly exceeds momentum diffusivity. This enhanced thermal transport manifests as reduced temperature gradients, with a distinctive minimum observed at the pipe's centerline. The superimposition of both boundary conditions reveals no discernible effect on first-order temperature statistics.

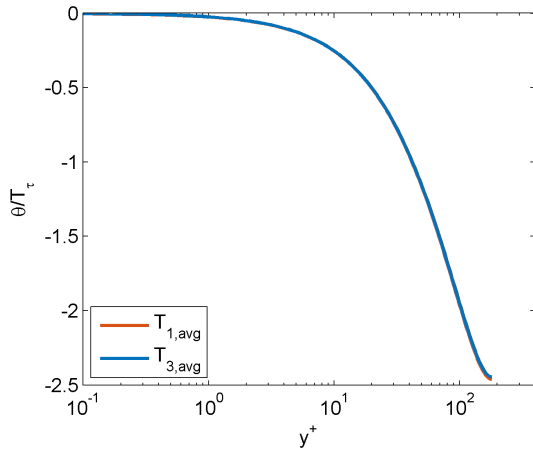


Figure 4.10: Excess temperature (mean temperature) distribution for $Pr = 0.025$ at 60 FTT, plotted against wall distance (y^+).

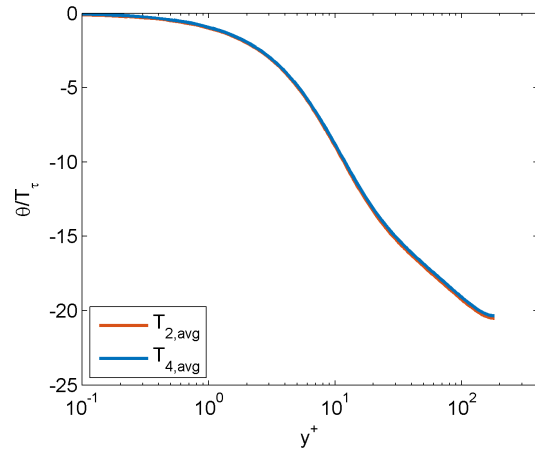


Figure 4.11: Excess temperature (mean temperature) distribution for $Pr = 1$ at 60 FTT, plotted against wall distance (y^+).

Figure 4.11 presents the excess temperature distribution for $Pr = 1$, demonstrating a temperature profile that closely tracks the axial velocity trend. This observation underscores the intrinsic coupling between thermal transport and fluid dynamics. Again, the superimposition of boundary conditions indicates no significant variation in first-order temperature statistics across different thermal boundary conditions for both Prandtl numbers.

The temperature fluctuations (T_{rms}), normalized with frictional temperature, are illustrated in Figures 4.12 and 4.13. These plots provide insights into thermal turbulence characteristics, with larger rms indicating regions of heightened thermal fluctuations.

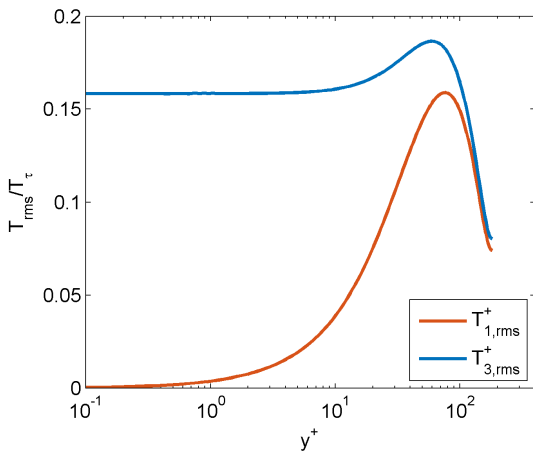


Figure 4.12: Temperature fluctuations for $Pr = 0.025$ at 60 FTT, plotted against wall distance (y^+).

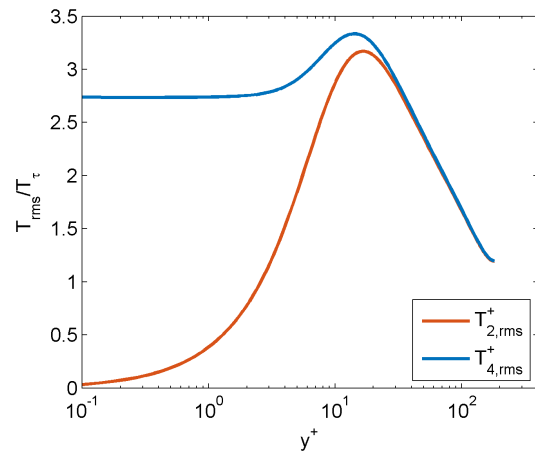


Figure 4.13: Temperature fluctuations for $Pr = 1$ at 60 FTT, plotted against wall distance (y^+).

For $Pr = 0.025$, the Dirichlet condition enforces zero temperature fluctuations at the wall. The maximum T_{rms} occurs near regions with the highest gradients of mean temperature – at $y^+ \sim 60$ for $Pr = 0.025$ and $y^+ \sim 15$ for $Pr = 1$. A gradual decrease towards the pipe centerline indicates minimal turbulence at the bulk.

An analogous observation is made for $Pr = 1$, where thermal diffusivity closely matches turbulence diffusivity, resulting in a trend similar to second-order velocity statistics.

Figures 4.14 and 4.15 present the streamwise turbulent heat flux ($w'T'$), normalized by bulk velocity (u_b) and temperature (T_b). For $Pr = 0.025$, near the walls with the no-slip boundary condition ($w' = 0$), $\langle w'T' \rangle$ naturally begins at zero, which is also observed for $Pr = 1$. As the distance from the wall increases, w' and T' interact more strongly, generating negative peak values.

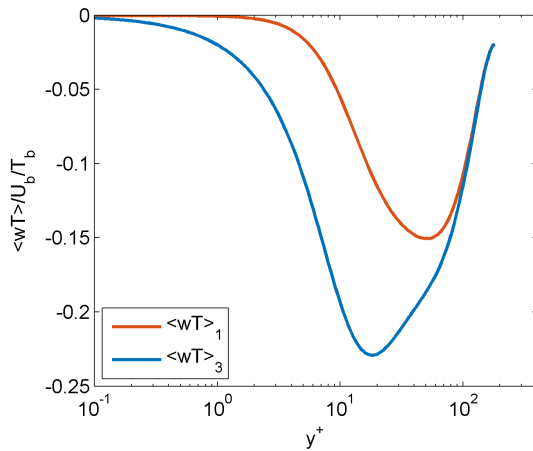


Figure 4.14: Streamwise turbulent heat flux ($w'T'$) at 60 FTT plotted against wall distance (y^+).

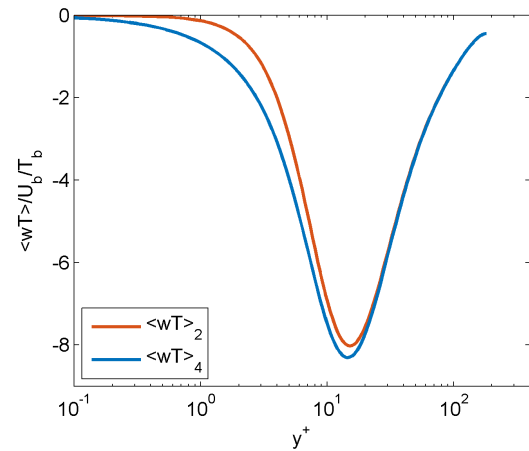


Figure 4.15: Streamwise turbulent heat flux ($w'T'$) at 60 FTT plotted against wall distance (y^+).

In the Neumann condition, the strong interaction of flow turbulence and thermal diffusion is evident. After the peak, the gradual decrease follows two distinct gradients, implying separate interactions of flow turbulence and thermal turbulence. The shifted peak and greater negative magnitude for the Neumann condition indicate suppressed heat flux where turbulent mixing is relatively low compared to the Dirichlet condition.

For $Pr = 1$, the trend closely follows velocity statistics due to equivalent thermal and momentum diffusivities. The Dirichlet condition demonstrates marginally enhanced thermal mixing.

Detailed temperature heat flux (THF) budget plots, including production, dissipation, convection, and turbulent diffusion terms, are provided in the Appendix (Figures A.1 -A.4) for comprehensive reference. These figures represent the final averaging period across the wall distance (y^+). While direct external validation is limited, the presented analysis draws confidence from the convergence of flow characteristics and the well-established interdependence between flow and heat transfer phenomena, suggesting statistical convergence of the scalar quantities.

4.3.3. Nusselt Number Analysis

The Nusselt number (Nu) quantifies heat transfer enhancement through convection, serving as a critical dimensionless parameter in thermal-hydraulic analysis. This section investigates Nusselt number characteristics for pipe flow, exploring interactions between fluid properties, boundary conditions, and heat transfer mechanisms. By examining Nusselt numbers across different Prandtl numbers, we aim to unravel fundamental heat transfer principles in pipe geometries, with emphasis on nuclear reactor thermal systems.

The key observations from the presented in Figure 4.16 are:

1. For the low Prandtl number ($Pr = 0.025$) fluid, representative of liquid metal coolants, the Nusselt numbers for both isothermal and isoflux boundary conditions lie significantly below the Dittus-Boelter and Gnielinski (generally used for higher Prandtl number) correlation, suggesting this widely used correlation may overestimate the heat transfer performance in such scenarios.
2. The thermal boundary condition (isothermal vs. isoflux) has a negligible impact on the Nusselt number for both $Pr = 0.025$ and $Pr = 1$ fluids, indicating that the heat transfer characteristics are primarily governed by the fluid properties and flow conditions.
3. The Nusselt numbers for the $Pr = 1$ fluid, corresponding to water at PWR conditions, closely follow the Dittus-Boelter Correlation, validating its applicability for near-unity Prandtl number coolants.

These observations highlight the importance of developing more accurate heat transfer models, particularly for low Prandtl number fluids, to ensure the reliable thermal-hydraulic design of PWR fuel assemblies. The insights gained from the pipe configuration presented here will be compared to the behaviour in a typical PWR subchannel geometry, providing a comprehensive understanding of the heat transfer characteristics in nuclear reactor systems.

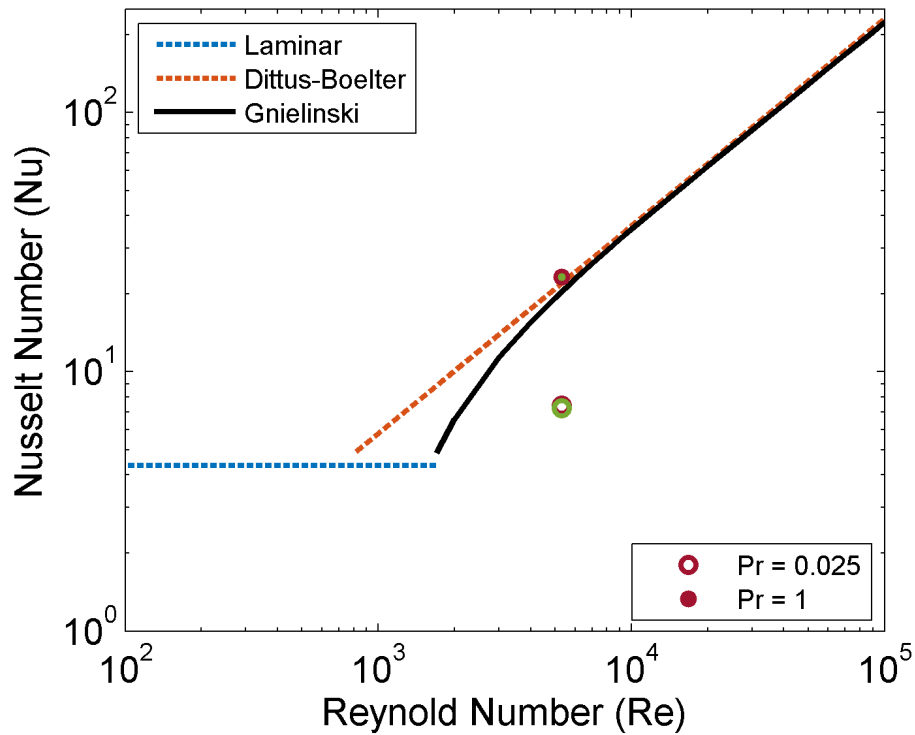


Figure 4.16: Nusselt number as a function of Reynolds number. Dotted markers represent $Pr = 0.025$, while hollow markers represent $Pr = 1$. Red indicates the isothermal condition, and green indicates the isoflux condition.

5

Subchannel

This chapter presents a rigorous analysis of subchannel flow simulations, focusing on convergence studies for square and 2x2 subchannel geometries. A comparative examination of these configurations will elucidate their distinct flow characteristics. The investigation encompasses:

- Computational setup for subchannel flow simulations
- Convergence analysis for square and 2x2 subchannel geometries
- Comparative assessment of flow dynamics between configurations
- Exploration of novel physical phenomena in subchannel flows
- Evaluation of computational challenges and their mitigation strategies

Through this analysis, we aim to advance the understanding of subchannel flow dynamics and refine computational methods for nuclear thermal-hydraulics simulations.

5.1. Flow and Heat Transfer Statistics Approach

In pipe flows, flow statistics are typically analyzed along the radius from the wall to the centre. However, the subchannel domain presents a more complex, non-axi-symmetric geometry. New approaches for analyzing flow and heat transfer statistics must be adopted to address this. A key concept in this study is the use of the "unit cell" (see Fig. 5.1a), which represents the smallest repetitive element that captures the essential flow and thermal characteristics of the subchannel. One can recreate the entire subchannel domain by mirroring or repeating these unit cells. Conceptually, the square subchannel can be folded twice across the x and y axes and further divided to isolate a single unit cell. Ideally, this unit cell accurately represents the entire flow field in a converged solution.

Despite two decades of research, there is no universally established methodology for evaluating flow and heat transfer statistics in subchannels. Researchers often adopt or modify existing techniques. This study employs two methods: the commonly used "Angle Method" and a novel "Circumferential Method." The "Angle Method" averages statistics of the domain to a unit cell and extracts values along lines from the centre of the rod to the domain wall at various angles, from 0° (representing flow at the gap) to 45° (closer to the bulk flow).

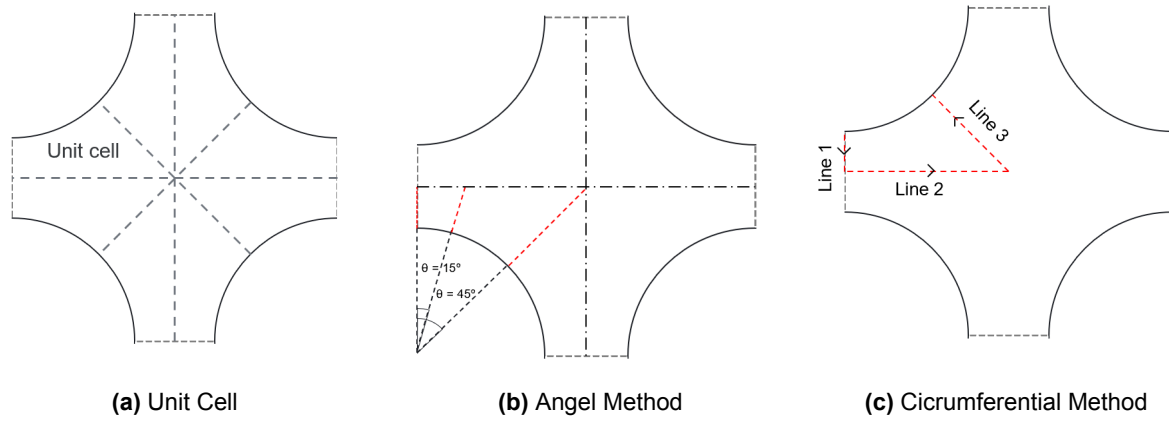


Figure 5.1: Unit cell and Statistical approaches for a Subchannel domain

The "Circumferential Method" examines flow along key lines at the unit cell boundary. Line 1 runs along the gap (analogous to the 0° line in the Angle Method), Line 2 traces the centerline from the gap to the subchannel centre, and Line 3 runs from the subchannel centre to the rod wall (comparable to the 45° line). These methods, named solely for reference in this thesis, provide the foundation for subsequent result plots and are used to systematically assess flow and heat transfer characteristics in the subchannel domain. It is also important to note that the direction of values along the line is crucial, especially for the "Circumferential method".

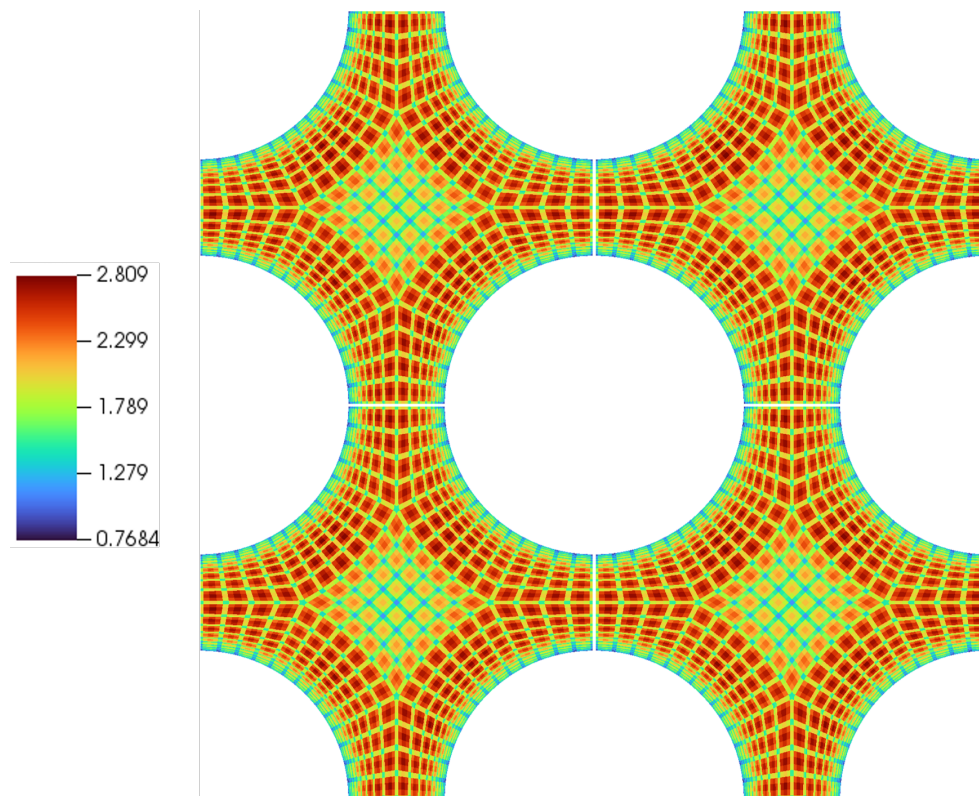


Figure 5.2: Distribution of cell size normalized by Kolmogorov length-scale ($\frac{\lambda}{\eta}$) for $N = 5$

5.2. Resolution

In Figure 5.2, the Kolmogorov length-scales, extracted from the resolved turbulent kinetic energy dissipation rate for a polynomial order 5 ($N = 5$), are depicted. The computational domain's resolution conforms to Pope's fundamental criterion [28], which mandates that the grid spacing must be commensurate with the local Kolmogorov length-scale (η) :

5.3. Square subchannel

As established in our geometric framework, the square subchannel configuration forms a fundamental unit of analysis in nuclear reactor thermal hydraulics. This subsection focuses on the detailed examination of flow characteristics within a single square subchannel, serving as a crucial baseline for understanding more complex subchannel arrangements.

Our investigation begins with a rigorous convergence study of the single square subchannel model. This study is essential for ensuring the numerical robustness and accuracy of the simulations, thereby validating the reliability of our results. By systematically refining our computational parameters, we aim to establish a solid foundation for characterizing the flow physics within this geometry.

The single square subchannel study encompasses several key aspects:

- First order and second order flow statistics
- Turbulent kinetic energy profiles

5.3.1. Convergence of statistical calculation

In alignment with the methodological approach employed in the pipe flow investigation, a comprehensive convergence study has been undertaken to elucidate flow physics in this thermal-hydraulic study. This section thoroughly examines first-order statistics, second-order moments and kinetic energy budget terms across various averaging periods. Statistical convergence is established when the L_2 norm error between successive averaging intervals remains below a threshold of 2% across all measured statistics. The present investigation utilizes fully resolved Direct Numerical Simulation (DNS) with polynomial order $N = 5$, conducted at a bulk Reynolds number (Re_b) of 5300. The temporal convergence study spans averaging periods from 20 to 35 FTTs, as detailed in Table 5.1.

The temporal scales crucial for this analysis are defined through three fundamental normalizations:

$$t^* = \frac{tU_b}{D_h} \quad (\text{Normalized time scale}) \quad (5.1)$$

$$t_\tau = \frac{tu_\tau}{R} = t^* \cdot \frac{Re_\tau}{Re_b} \quad (\text{Eddy turnover time}) \quad (5.2)$$

$$t^+ = \frac{tu_\tau^2}{\nu} = t^* \cdot \frac{Re_\tau^2}{Re_b} \quad (\text{Wall-scaled time}) \quad (5.3)$$

FTT	t^*	t_τ	t^+
20	960	72.2	26086
25	1200	90.3	32607
30	1440	108.3	39128
35	1680	126.4	45649

Table 5.1: Flow-through times (FTTs) and corresponding normalized time scales

Velocity Statistics

Figure 5.6 illustrates the first-order statistics, precisely the mean axial flow velocity (U_z) normalized by friction velocity (u_τ). The axial velocity assessment employed the circumferential method, extracting values

from the subchannel gap through the centerline to the flow centre and back to the rod at a 45-degree angle. In this square subchannel configuration, the analysis traverses the shortest gap, along the boundary, and diagonally towards the rod centre; these trajectories are designated as sections 1-2-3 to avoid nomenclature ambiguity in the subsequent plots. This path is characterized by a novel distance term ξ , normalized with respect to the Hydraulic diameter (D_h).

Figure 5.3 demonstrates that the velocity magnitude reaches its minimum proximate to the wall due to surface friction, as evidenced in sections one and three. Section two exhibits quasi-uniform behaviour, which is characteristic of bulk flow. The first-order statistics demonstrate robust convergence prior to the averaging period of 35FTTs, as evidenced by the superposition of temporal data, yielding a relative L^2 norm error below 0.03%.

Figure 5.4 delineates the second-order flow statistics, specifically three velocity fluctuation components— u_{rms} , v_{rms} , and w_{rms} —normalized by friction velocity (u_τ). These statistics were analyzed utilizing the aforementioned circumferential methodology. Distinct averaging periods are differentiated through varying line styles, in contrast to the colour-based representation employed in Figure 5.6. As anticipated, second-order statistics exhibit extended convergence periods, particularly evident in the w_{rms}^+ term. All three velocity components converged at 35 FTTs, maintaining an L^2 norm below 0.6% relative error. The dual peaks observed in w_{rms}^+ within sections 1 and 3 are attributed to near-wall turbulence production. The disparity between u_{rms}^+ and v_{rms}^+ in section 1 primarily stems from the gap distance constraining v_{rms}^+ fluctuations, while u_{rms}^+ experiences comparatively greater spatial freedom. Supplementary verification of second-order statistics is provided in Appendix A (Figures 1, 2, and 3).

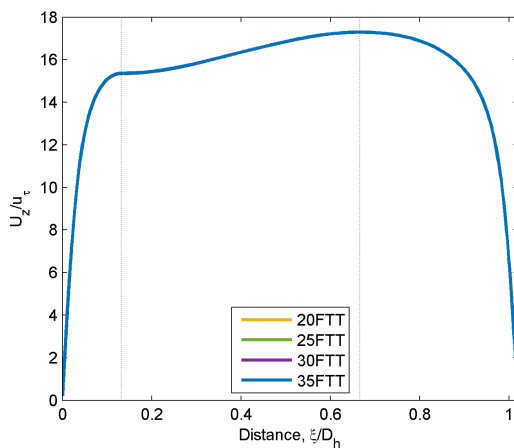


Figure 5.3: Axial velocity (u_z) plotted using the circumferential method for different averaging periods

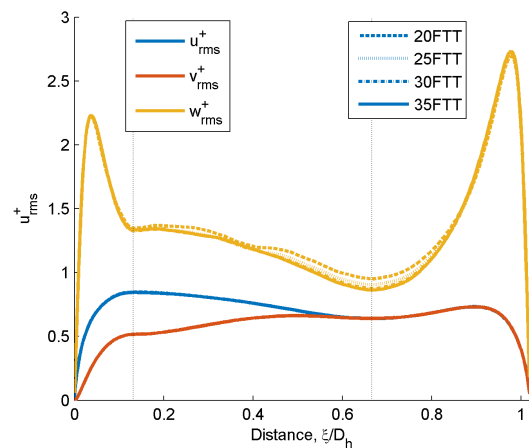


Figure 5.4: Velocity fluctuations along 3 axes plotted using the circumferential method for different averaging periods

Figure 5.5 presents the TKE budget terms, analyzed via the circumferential method. The analysis focuses exclusively on production and dissipation terms to examine convergence characteristics. Both parameters converged at an averaging period of 35FTT, exhibiting an L^2 norm below 0.4% relative error. The aforementioned dual production term peaks manifest in sections 1 and 3, accompanied by corresponding dissipation patterns representing the decay of turbulent energy into viscous heat energy near the wall. Despite the generally satisfactory results, section 2 of the dissipation terms exhibits minor anomalous troughs. These artifacts are attributed to mesh imprints, which are anomalies present in Nek5000-SEM discretisation. Given that these perturbations are minimal and the resolution satisfies Kolmogorov length scale criteria, they do not significantly impact subsequent analyses, presenting merely as a minor data quality consideration.

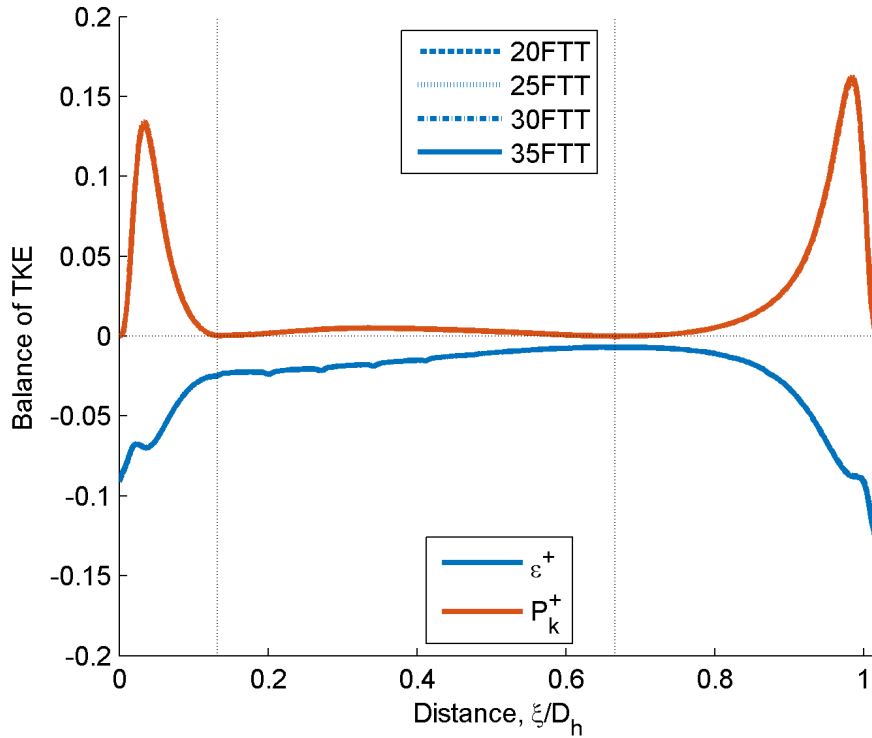


Figure 5.5: Turbulent Kinetic Energy (TKE) Budget terms plotted using the circumferential method for different averaging periods

Table 5.4 summarises the quantitative convergence metrics.

First Order	Second Order	TKE budget terms
<0.03%	<0.6%	<0.4%

Table 5.2: Relative L^2 norm error analysis at 35FTT

5.4. 2x2 subchannel

Building upon the convergence study of the single square subchannel, this section focuses on the detailed investigation of flow characteristics within the 2x2 subchannel configuration. The key aspects examined include:

- First and second-order flow statistics
- Turbulent kinetic energy profiles

The study begins with a rigorous convergence analysis to ensure the numerical robustness and accuracy of the simulations, establishing a reliable foundation for the flow physics characterization.

5.4.1. Convergence of Statistical Calculations

The study presented here employs identical quantities and approaches in alignment with the methodology applied in the square subchannel case. The 2x2 subchannel configuration effectively represents a composite of four single subchannels, thereby maintaining geometric equivalence to the single square subchannel case but on an extended mesh and spatial scale. Given this scalability, characteristic times are expected to scale proportionally with the cross-sectional area or volume ratios, leading us to anticipate a converged solution around 9FTT—given the established convergence at 35FTT for the square subchannel.

It is crucial to acknowledge that this estimate serves as an initial guideline for convergence in flow and heat transfer statistics. The scalability assumption inherently introduces approximation, with convergence rates

potentially impacted by subtle differences in boundary and initial conditions. The study spans averaging periods of 5, 7, 9, and 10 FTTs, represented in normalised time, eddy turnover time and wall-scaled units as documented in Table 5.3. Simulations were executed using fully resolved direct Numerical Simulation (DNS) at a polynomial order of 5 ($N = 5$). The Bulk Reynolds (R_b) was 5300.

FTT	t^*	t_τ	t^+
5	240	18.0	6522
7	336	25.3	9131
9	432	32.5	11739
10	480	36.1	13044

Table 5.3: Flow-through times (FTTs) and corresponding normalized time scales

Velocity Statistics

Consistent with the observations in the square subchannel, Figure 5.6 illustrates the mean axial velocity (U_z) normalized by the friction velocity (u_τ) and plotted using circumferential method across various averaging periods of (5, 7, 9, and 10 FTTs). The results reveal a convergence as early as 5FTT, where all plotted lines exhibit superposition, indicating a solution convergence with an L^2 norm relative error under 0.02%. This demonstrates that the fundamental flow physics observed in the square subchannel is transferable to the 2x2 subchannel for first-order statistics.

Figure 5.7 presents the normalised circumferential plots of the three velocity fluctuations components. The superposition of these curves—including the w_{rms} component—illustrates consistency with the square subchannel data, likely due to the scaling effects on averaging. In the 2x2 subchannel, statistics are effectively averaged fourfold over the square subchannel, enhancing the stability of convergence metrics. This is corroborated by the L^2 norm error for second-order statistics, converging at 10FTT with a relative error below 0.06%—ten times lower than in the square subchannel scenario. Again, the dominant flow characteristics and symmetry observed in the square subchannel hold true in this expanded configuration.

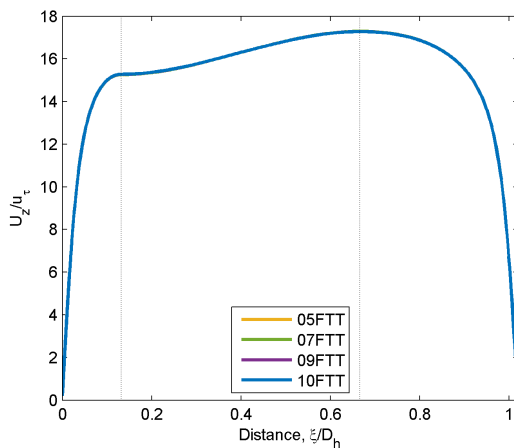


Figure 5.6: Axial velocity (u_z) plotted using the circumferential method for different FTT values.

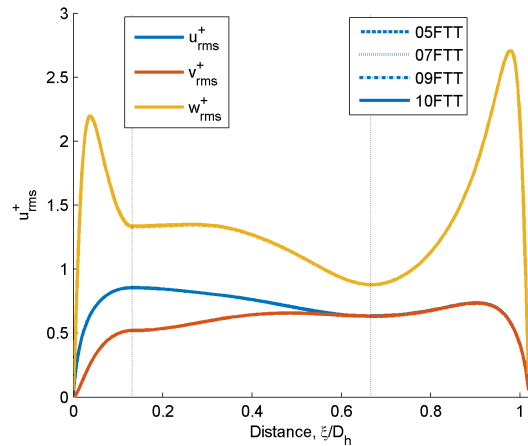


Figure 5.7: Velocity fluctuations along three axes using the circumferential method for different FTT values.

Figure 5.8 illustrates the Turbulent kinetic energy (TKE) budget terms (production and dissipation) as plotted via the circumferential method. Both terms achieve convergence at 10 FTTs, aligning with the findings of the second-order statistics, and display an L^2 norm relative error below 0.12%. The dominant flow characteristics and the residual mesh effects observed in the square subchannel remain applicable.

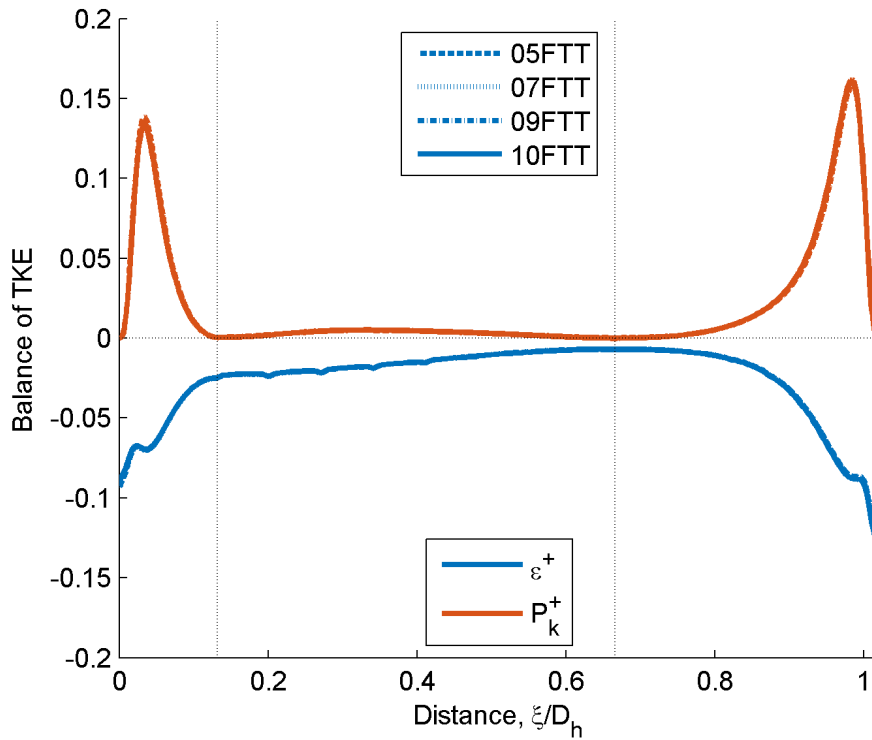


Figure 5.8: Turbulent Kinetic Energy (TKE) budget terms at 10 FTT using the circumferential method

A summary of the convergence metrics is provided in Table 5.4.

First Order	Second Order	TKE budget terms
<0.02%	<0.06%	<0.12%

Table 5.4: Relative L^2 norm error analysis at 10 FTT

5.5. Comparison between Square and 2x2 Subchannel

This section presents a comparative study between the square subchannel and 2x2 subchannel cases to validate the underlying assumption that a single subchannel can faithfully represent the flow field in a bundle rod arrangement. This analysis will employ advanced statistical techniques, such as autocorrelation, to identify and understand flow trends and statistics covered in the preceding convergence study.

5.5.1. Higher order statistics

This section presents a comprehensive analysis of higher-order statistics to elucidate the distinctions in flow physics and thermal characteristics between square subchannel and 2x2 subchannel configurations. The statistical analysis predominantly employs the circumferential method to facilitate systematic comparison between both cases. Based on the convergence analysis, it has been established that averaging periods of 35FTT and 10FTT achieved converged solutions for square and 2x2 subchannels, respectively, as evidenced by the TKE budget terms and higher-order velocity statistics. Subsequently, these respective averaging periods serve as the basis for comparative analysis.

Velocity Statistics

Figure 6.3 illustrates the first-order statistics, precisely the axial flow velocity (u_z) normalized by shear velocity (u_τ) for the last averaging periods of each configuration. The superimposed plots demonstrate remarkable consistency in mean flow velocity profiles across the unit cell boundary. A marginal deviation is observed in the central gap region, where the 2x2 subchannel exhibits a slightly diminished magnitude compared to the square subchannel configuration. However, this discrepancy may be attributed to the averaging methodology employed in the 2x2 subchannel analysis.

Figure 5.10 presents the angular distribution of wall shear stress (τ_w) from $0^\circ - 45^\circ$. The study reveals peak τ_w at 20° and minimum at 45° , contrasting with conventional pipe flow theory, which predicts maxima at 45° (bulk flow proximity) and minima at 0° (gap region). This deviation can be attributed to the complex interplay between secondary flow phenomena (detailed in Section 1.5.1) and gap vortex street.

Ninokanta's [38] DNS investigation of staggered pin arrangements ($P/D = 1.2$) at $Re = 9,120$ and $24,300$, validated against experimental data, provides crucial insights. The higher Reynolds number case exhibits a more uniform distribution, characterized by enhanced wall-to-bulk pressure gradients along the 45° line. This intensified pressure gradient induces more substantial secondary flows ($\sim 1 - 2\%$ of bulk flow), which is counterbalanced by wall friction dissipation. At elevated Reynolds numbers, the mechanism manifests through increased wall adherence and stretched secondary flow vortices, evidenced by enhanced wall shear stress at lower angles and reduced values at higher angles where pressure gradients induce bulk-ward flow migration.

The observed flattening effect correlates with intensified secondary flows, promoting enhanced eddy transport between open and narrow gap regions with increasing Re_{bulk} [38]. The subchannel geometry significantly modulates this behaviour; increased P/D ratios favour vortex relaxation over stretching at equivalent Reynolds numbers. While theoretical considerations suggest identical wall shear stress distributions for 2x2 and square subchannel configurations, observed disparities may stem from variations in gap street vortex capture capabilities, particularly regarding the rod bundle vortex network. However, definitive conclusions are constrained by the absence of comparable geometric studies and experimental validation data.

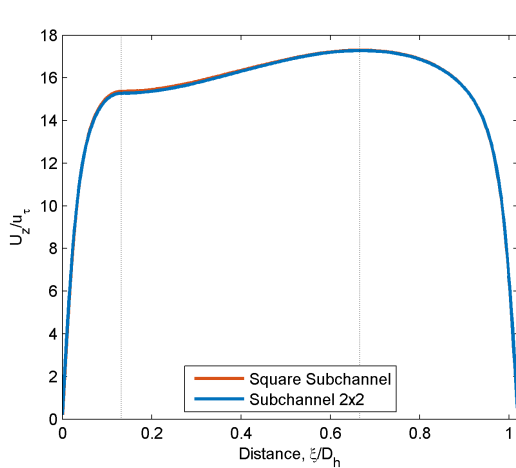


Figure 5.9: Axial velocity (u_z) comparison between configurations, plotted using the circumferential method at converged FTT.

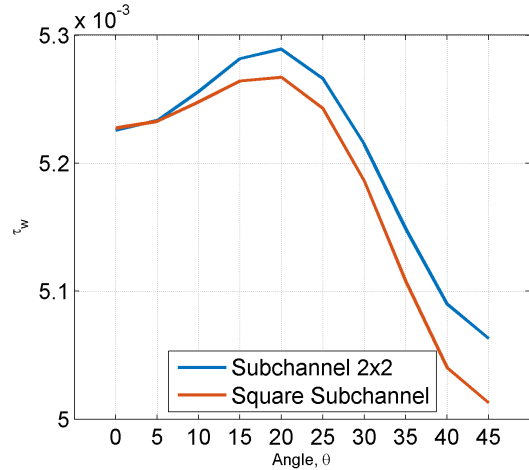


Figure 5.10: Wall shear stress (τ_w) distribution comparison, plotted using the angle method at converged FTT.

Figures 5.11 and 5.12 present a comparison of second-order statistics, explicitly examining the Normal stresses and Reynolds stresses for both square and 2x2 subchannel configurations. The study is conducted along each case's unit cell boundary at the last averaging periods, with dashed and solid lines representing the square and 2x2 subchannel configurations, respectively.

The normal stress distributions (Figure 5.11) reveals notable characteristics. The components of the $\langle u'u' \rangle$ and $\langle v'v' \rangle$ demonstrate remarkable congruence between configurations, exhibiting virtually identical profiles. However, the $\langle w'w' \rangle$ component displays subtle variations across the unit cell boundary. While these variations appear systematic, their magnitude is likely attributable to the averaging methodology employed in the 2x2 subchannel analysis rather than representing physically significant differences. A particularly noteworthy observation is the diminished rms peaks in the $\langle w'w' \rangle$ component for the 2x2 subchannel configuration relative to its square subchannel counterpart.

The Reynolds stress distributions (Figure 5.12) exhibit more pronounced disparities, particularly evident in section 3 (along the 45° line) of the plot, for the $\langle u'w' \rangle$ and $\langle u'v' \rangle$ components. The 2x2 subchannel configuration demonstrates significantly attenuated peak magnitudes compared to the square subchannel. This disparity may be attributed to limitations in capturing the rod bundle vortex network within the square subchannel configuration, potentially resulting in an overestimation of Reynolds stress components.

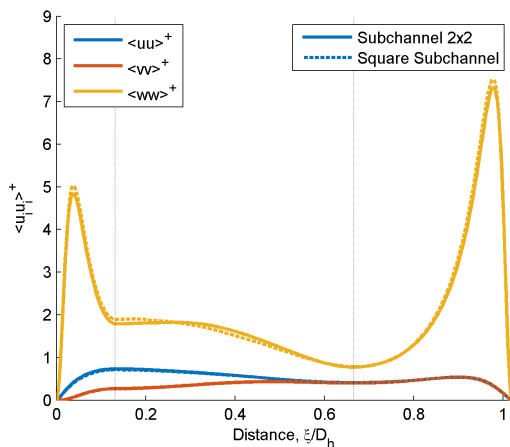


Figure 5.11: Normal stress distributions as a function of wall distance (y^+) at converged FTT for both configurations.

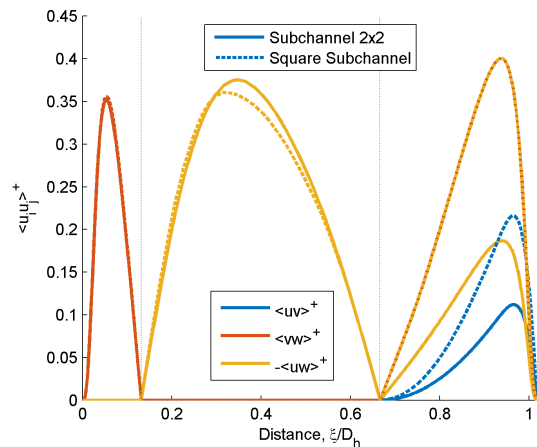


Figure 5.12: Reynolds stress distributions as a function of wall distance (y^+) at converged FTT for both configurations.

The Turbulent kinetic energy (TKE) budget analysis, presented in Figure 5.13, demonstrates remarkable consistency between the square and 2x2 subchannel configurations. The profiles exhibit near-perfect superposition, with only minor deviations that fall within the uncertainty bounds attributable to the aforementioned averaging methodology. This convergence in TKE distributions suggests fundamental similarities in the energetic characteristics of turbulent structures between the two configurations despite the geometric differences in their respective domains.

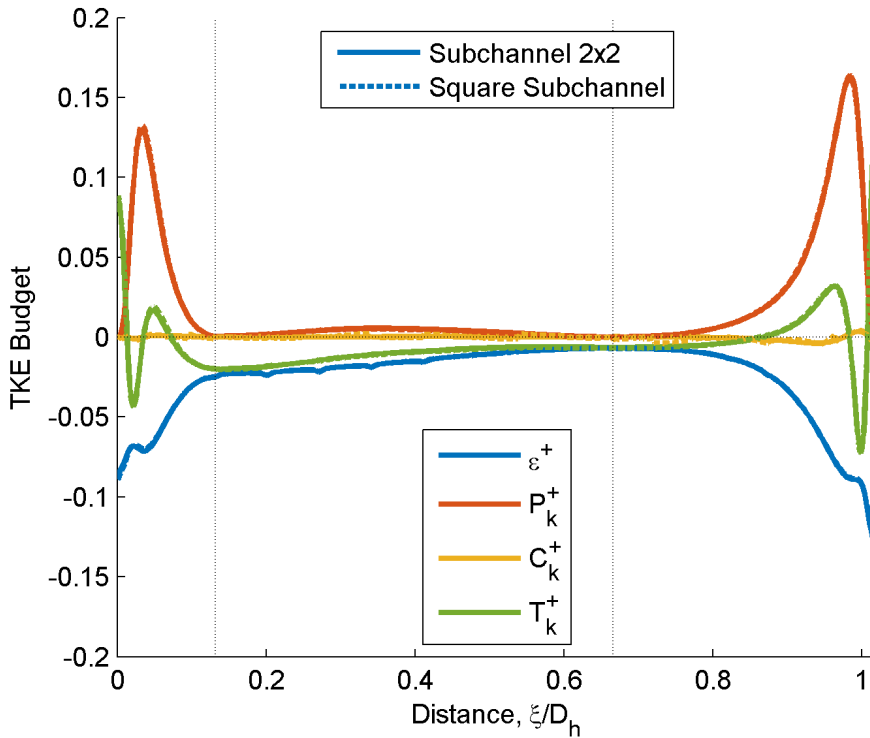


Figure 5.13: Turbulent Kinetic Energy (TKE) budget distributions as a function of wall distance (y^+) at converged FFT for both configurations.

Temperature Statistics

Figures 5.14 and 5.15 present the first-order temperature statistics, where scalar excess temperatures (θ) are normalized by friction temperature (T_τ) for the final averaging period of each configuration. The analysis considers two distinct boundary conditions at different Prandtl numbers.

Figure 5.14 illustrates the temperature distribution at $Pr = 0.025$ under two boundary conditions: a Dirichlet condition (θ_1) prescribing constant wall temperature, and a Neumann condition (θ_3) enforcing constant heat flux. For the Dirichlet condition, the heated rod maintains a constant temperature ($T = T_w$), resulting in zero excess temperature ($\theta = 0$) at the boundaries. The Neumann condition, conversely, constrains the temperature gradient ($\partial\theta/\partial y$) rather than the absolute temperature values. For $Pr = 0.025$, the characteristic of liquid metals is that thermal diffusivity significantly exceeds momentum diffusivity. This enhanced thermal transport leads to efficient heat distribution across the domain, manifesting as reduced temperature gradients and a distinct minimum at the subchannel centre.

Figure 5.15 presents the excess temperature distribution along the unit cell boundary at $Pr = 1$, comparing Dirichlet (θ_2) and Neumann (θ_4) conditions. The temperature profile under the Dirichlet condition closely follows the axial velocity trend, demonstrating a strong coupling between thermal transport and fluid motion. The temperature variation exhibits pronounced peaks and troughs, correlating with velocity-induced convective cooling effects. Near the isothermal boundaries, where $\theta = 0$, the profile shows characteristic conduction-dominated behaviour transitioning to convection-dominated transport in the bulk flow.

The first-order temperature statistics exhibit nearly identical profiles when comparing the 2×2 and square subchannel configurations. The overlapping temperature distributions suggest that the basic thermal transport mechanisms remain unaffected.

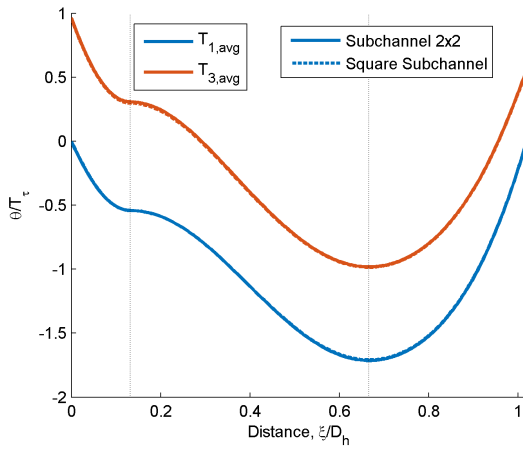


Figure 5.14: Mean temperature distribution for $Pr = 0.025$.

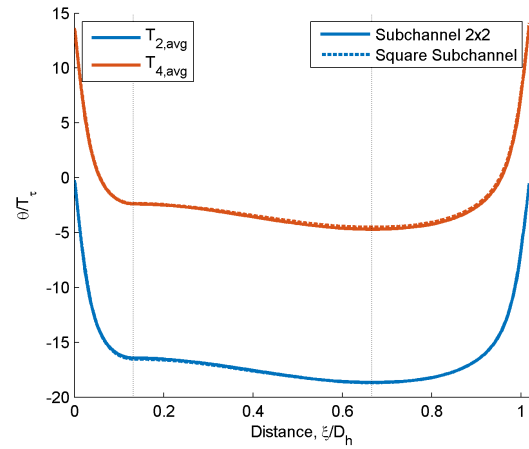


Figure 5.15: Mean temperature distribution for $Pr = 1$.

In Figure 5.16 and 5.17, Temperature fluctuations (T_{rms}), normalised with frictional temperature (T_τ), were plotted across the boundary of the unit cell. T_{rms} is the root mean square of temperature fluctuations in the domain. It quantifies the magnitude of deviations of local temperature from its mean value. T_{rms} gives a measure of the thermal turbulence or intensity of temperature fluctuations caused by fluid flow (convection) and heat transfer interactions. Larger T_{rms} indicates regions with high thermal turbulence, while smaller T_{rms} corresponds to smoother, more uniform temperature distributions.

In figure 5.16 both lines, $T_{1,rms}$ representing Isothermal and $T_{3,rms}$ representing isoflux exhibit oscillatory behaviour with hills (peaks) and valleys (troughs) in the subchannel domain. The hills (peaks) represent regions of enhanced thermal turbulence, while the valleys (troughs) indicate dampened fluctuations. For $Pr=0.025$, thermal diffusivity is much higher than momentum diffusivity ($\alpha \gg \nu$); this allows heat to diffuse faster across the domain, reducing the sharpness of temperature gradients and smoothing out the fluctuations. However, in regions of strong convective flow (from subchannel gap to bulk), turbulence increases, amplifying the temperature fluctuations and forming the hills. Turbulence (w_{rms}) is the lowest at the centre of the subchannel, which is reflected in T_{rms} as the lowest (minima) point. For $T_{1,rms}$, a fixed temperature at the wall suppresses fluctuations at the boundaries, resulting in $T_{rms} = 0$ there. For $T_{3,rms}$, fixed heat flux at the boundary, T_{rms} does not vanish at the walls. The constant flux allows some fluctuations to persist even near the walls, especially if the local velocity gradients drive turbulent behaviour. High thermal diffusivity results in smoother T_{rms} variations but retains oscillatory trends due to underlying turbulence interaction.

From previous figures 5.15 for θ_2 and θ_4 , it was evident that the temperature profile followed the velocity distribution. Since T_{rms} represents deviations from the mean temperature, the rms trend follows the spatial variation in velocity fluctuations (w_{rms}), which is evident in figure 5.17. The implication of different boundary conditions applies here as well.

Statistical analysis of the second-order temperature reveals negligible variations between the 2×2 and square subchannel configurations. The observed deviations fall within the bounds of statistical uncertainty. Therefore, the second-order temperature statistics can be considered effectively equivalent for both configurations within the present parameter space.

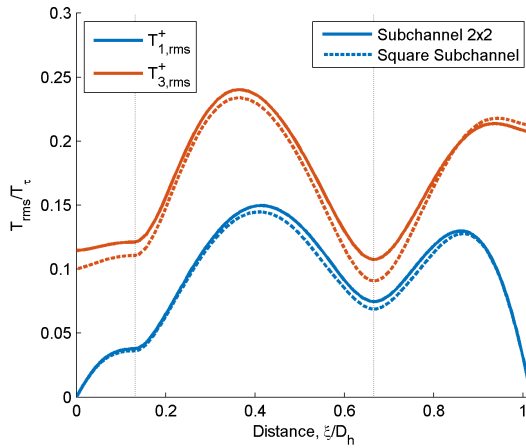


Figure 5.16: Temperature fluctuations for $Pr = 0.025$.

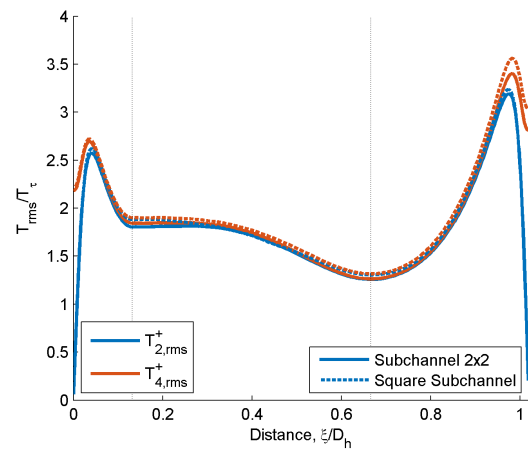


Figure 5.17: Temperature fluctuations for $Pr = 1$.

Figures 5.18 and 5.19 present the streamwise turbulent heat flux ($w'T'$), normalized by bulk velocity (u_b) and temperature (T_b). Streamwise THF ($\langle w'T' \rangle$) represents the turbulent heat flux in the axial direction. The quantity captures the contribution of turbulent eddies to the convective transport of heat in the flow, where positive or negative peaks of $\langle w'T' \rangle$ indicate regions of enhanced or suppressed heat flux, respectively, highlighting areas where turbulent mixing is most effective.

In Figure 5.18, Near the walls, where the no-slip boundary condition ensures $w' = 0$, $\langle w'T' \rangle$ naturally starts at zero. However, as the distance from the wall increases, w' and T' begin to interact strongly, leading to negative peak values. These negative peaks correspond to regions of maximum production of turbulent energy and heat transfer. Negative peaks in $\langle w'T' \rangle$ often coincide with regions where w_{rms} and T_{rms} are significant. At the subchannel centre, where turbulent thermal mixing is most effective, $\langle w'T' \rangle$ tends to be more relatively positive.

In Figure 5.19 for $Pr = 1$, the heat flux profile closely follows the w_{rms} distribution, reflecting the equipartition of momentum and thermal diffusivities. The nearly identical responses of T_2' and T_4' demonstrate comparable behaviour between isothermal and isoflux conditions under matched diffusivity conditions. For $Pr = 0.025$, thermal diffusion dominates momentum transport, resulting in attenuated coupling between velocity and temperature fluctuations. This manifests as reduced $w'T'$ magnitudes compared to the $Pr = 1$ case, evident in the differing ranges between Figures 5.18 and 5.19.

Negligible variations between the 2x2 and square subchannel configurations. The observed deviations fall within the bounds of statistical uncertainty.

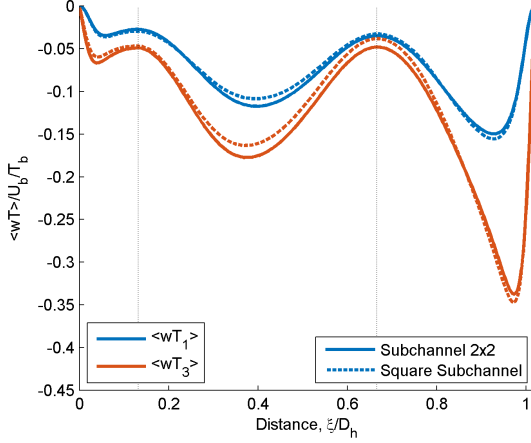


Figure 5.18: Turbulent heat flux for $Pr = 0.025$.

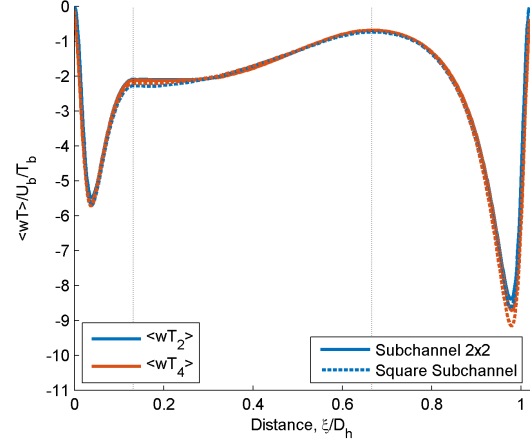


Figure 5.19: Turbulent heat flux for $Pr = 1$.

Detailed temperature heat flux (THF) budget plots for the subchannel 2x2 and square subchannel configurations, encompassing production, dissipation, convection, and turbulent diffusion terms, are presented in the Appendix (Figures A.5-A.8). These comprehensive figures capture the final averaging period across the boundary of the unit cell.

5.5.2. Autocorrelation

Autocorrelation quantifies the correlation between observations of a variable with either its spatially or temporally shifted variant. In the temporal domain, it measures the similarity between time-series data points separated by a specific time lag, while spatial autocorrelation evaluates the correlation between observations at different spatial locations. More formally, it represents the statistical correlation between the original signal and its delayed or displaced copy as a function of the lag (temporal) or displacement (spatial) parameter.

For analyzing velocity fluctuations in a subchannel DNS simulation, the normalized two-point space-time autocorrelation function can be expressed as:

$$R(\mathbf{r}, \tau) = \frac{\overline{u'(\mathbf{x}, t)u'(\mathbf{x} + \mathbf{r}, t + \tau)}}{u'^2} \quad (5.4)$$

where:

- R represents the autocorrelation coefficient
- \mathbf{x} is the reference position vector
- \mathbf{r} is the spatial separation vector
- t is the reference time
- τ is the time lag
- u' represents velocity fluctuation (either spanwise u' , wall-normal v' , or axial w')

This formulation can be applied independently to the three velocity components to understand their distinct correlation behaviours along the subchannel walls. For spatial analysis along the wall boundaries, the correlation can be evaluated at different spatial separations while maintaining $\tau = 0$:

$$R(r) = \frac{\overline{u'(\mathbf{x}, t)u'(\mathbf{x} + r, t)}}{u'^2} \quad (5.5)$$

Since a direct comparison is employed to assess the 2x2 subchannel and square subchannel, we will focus our analysis on the spatial autocorrelation.

Square Subchannel

For the square subchannel case, the boundary walls will be used for this assessment, where the vertical boundary walls will be termed X-normal (X_n), and horizontal boundary walls will be called Y-normal (Y_n). Spatial autocorrelation is applied at the boundary of a two-dimensional slice in the x-y plane, either along the y-axis for X_n or the x-axis for Y_n . This process is carried out for multiple slices in the z-direction with a slice interval of Δr_z , and the results are averaged in the z-direction to attain a spatially averaged autocorrelation. This is then further averaged in time by reiterating the process for the last 10 timesteps to produce a spatio-temporal averaged autocorrelation of the velocity fluctuations. Figure 5.20 & 5.21 presents the time-averaged autocorrelation of the x-velocity fluctuations (u') plotted across the width/height of the domain. The 10 semi-transparent grey lines represent the individual autocorrelation lines at different timesteps, while the coloured line depicts the temporally averaged autocorrelation. Ideally, the first and last points should be unity since the corner points in the domain are highly correlated due to the periodic boundary conditions. Although slightly less than one, this slight deviation is likely due to the influence of the near-wall turbulence structures.

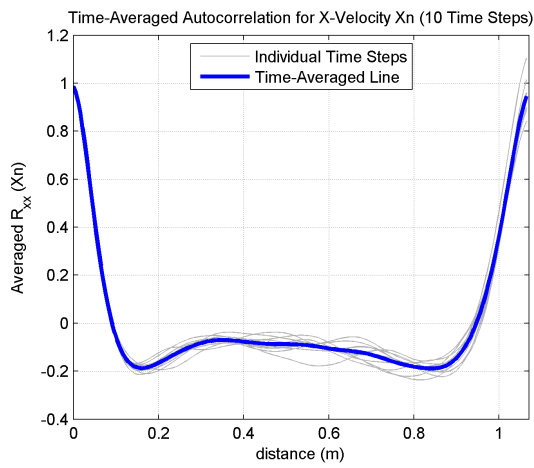


Figure 5.20: Time-averaged autocorrelation of x-velocity (u') fluctuations in the X normal plane of the square subchannel.

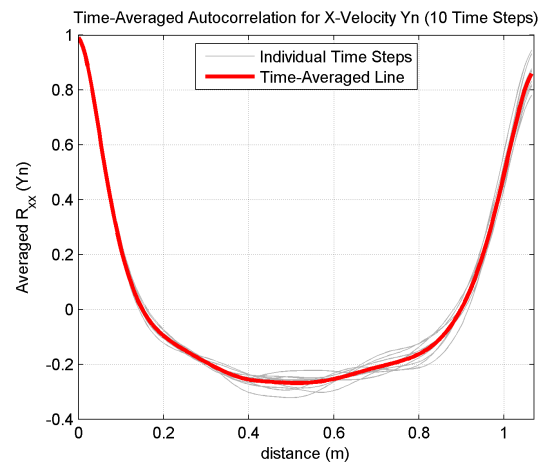


Figure 5.21: Time-averaged autocorrelation of x-velocity (u') fluctuations in the Y normal plane of the square subchannel.

The same trend is observed for the y-velocity (v') fluctuations in Figure 5.22 & 5.23, where the plots appear interchanged. This is because the X_n u' fluctuations represent the fluctuations normal to the boundary, which is observed in the Y_n v' fluctuations, and vice versa.

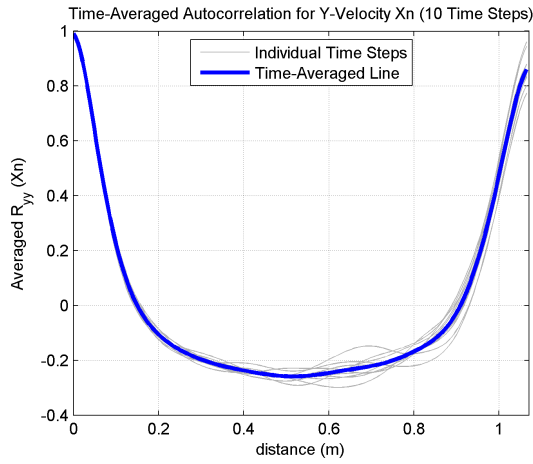


Figure 5.22: Time-averaged autocorrelation of y -velocity (v') fluctuations in the X normal plane of the square subchannel.

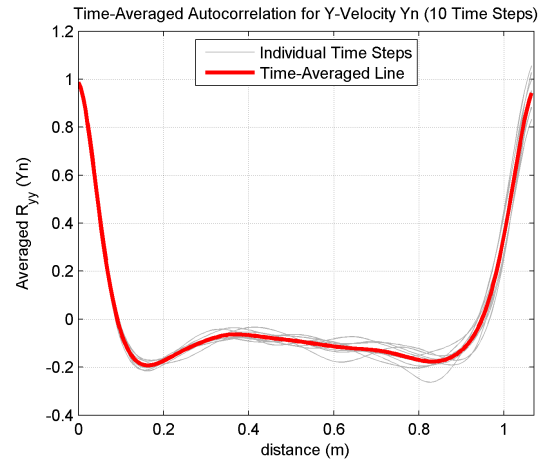


Figure 5.23: Time-averaged autocorrelation of y -velocity (v') fluctuations in the Y normal plane of the square subchannel.

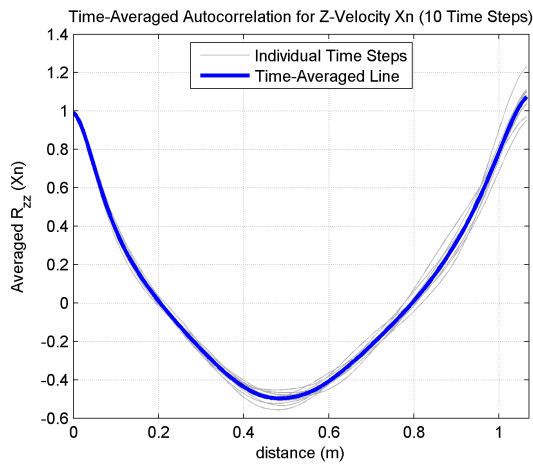


Figure 5.24: Time-averaged autocorrelation of z -velocity (w') fluctuations in the X normal plane of the square subchannel.

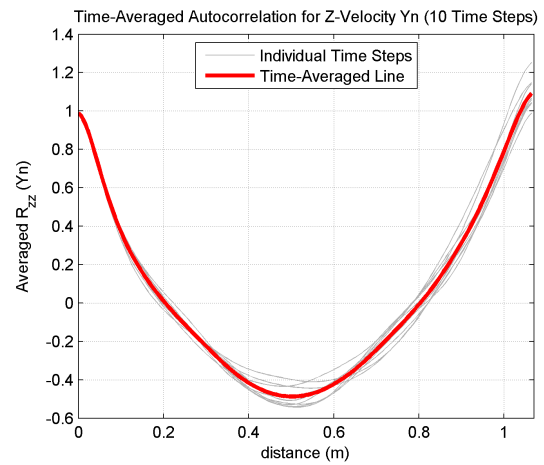


Figure 5.25: Time-averaged autocorrelation of z -velocity (w') fluctuations in the Y normal plane of the square subchannel.

Figure 5.24 & 5.25, representing the w' (axial) fluctuations in the X_n and Y_n directions, exhibits a markedly different trend compared to the spanwise and wall-normal components. The high correlation at the corner points validates the accuracy of the boundary conditions, and the perfect overlap of the temporally averaged autocorrelation for w' fluctuations across both axes further confirms the consistency of the flow field.

Parameter	Value
Number of divisions in X norm	200
Number of divisions in Y norm	200
Number of slices in Z direction	480
Timestep for square subchannel	0.4 FTT
Timestep for 2x2 subchannel	0.5 FTT

Table 5.5: Auto correlation parameters

2x2 Subchannel

The same autocorrelation analysis approach is applied to the 2x2 subchannel case, but for a direct comparison, only the centre section of the 2x2 subchannel is considered, which represents the square subchannel case. The X_n is defined from the centre of one subchannel to the centre of the adjacent subchannel in the vertical direction, and Y_n is defined from the centre of one subchannel to the centre of the adjacent subchannel along the y-axis.

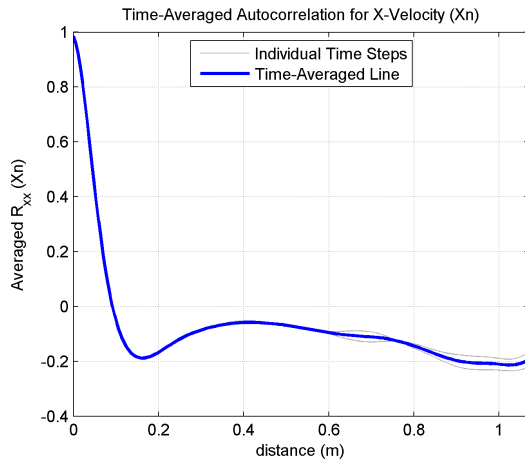


Figure 5.26: Time-averaged autocorrelation of x-velocity (u') fluctuations in the X normal plane of the 2x2 subchannel.

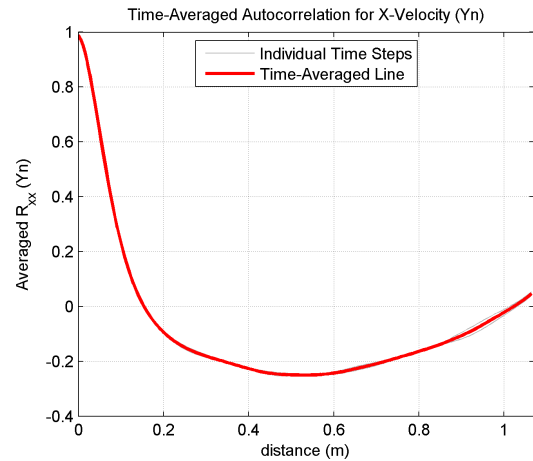


Figure 5.27: Time-averaged autocorrelation of x-velocity (u') fluctuations in the Y normal plane of the 2x2 subchannel.

Figures 5.26 - 5.27 and 5.28 - 5.29 show the autocorrelation plots for u' and v' fluctuations, respectively, along the X_n and Y_n directions. The semi-transparent grey lines represent the individual timesteps, and the coloured line depicts the time-averaged autocorrelation. In contrast to the square subchannel, where the first and last points were close to unity, this is not the case for the 2x2 subchannel, signifying that the interactions between subchannels play a significant role in the flow dynamics.

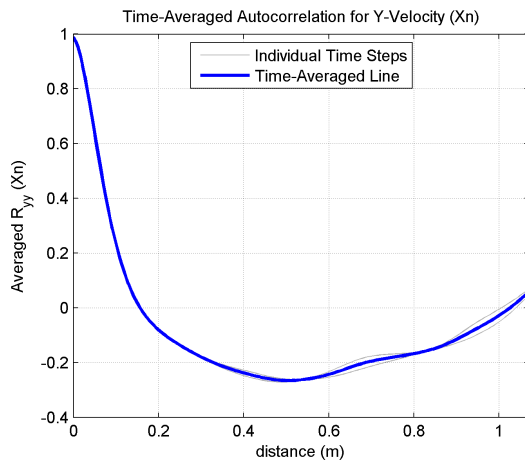


Figure 5.28: Time-averaged autocorrelation of y-velocity (v') fluctuations in the X normal plane of the 2x2 subchannel.

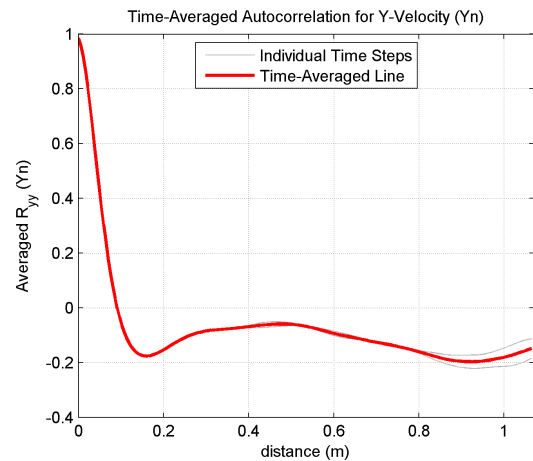


Figure 5.29: Time-averaged autocorrelation of y-velocity (v') fluctuations in the Y normal plane of the 2x2 subchannel.

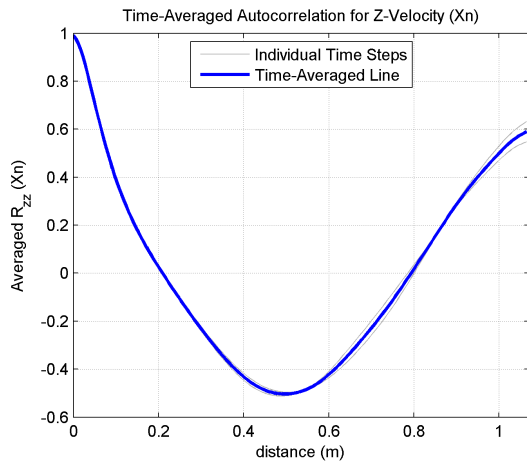


Figure 5.30: Time-averaged autocorrelation of z-velocity (w') fluctuations in the X normal plane of the 2x2 subchannel.

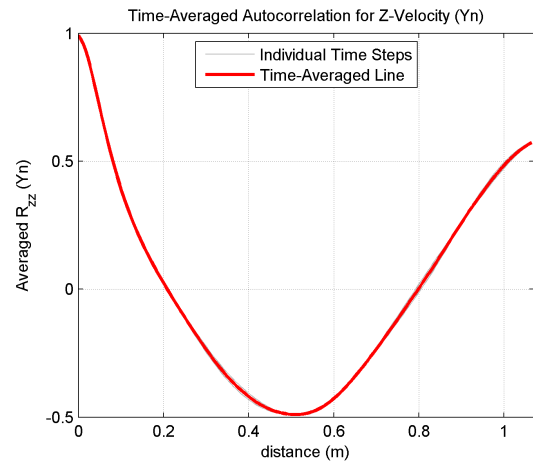


Figure 5.31: Time-averaged autocorrelation of z-velocity (w') fluctuations in the Y normal plane of the 2x2 subchannel.

The same observation holds true for the w' (axial) fluctuations, as shown in Figure 5.30 - 5.31, where the high correlation at the boundaries is no longer present.

When analyzing the 2X2 subchannel from the centre of one subchannel to the centre of the adjacent subchannel, it did not exhibit the same high degree of correlation as the square subchannel case. This observation suggests that although a single square subchannel is capable of capturing the gap street vortex, it fails to account for the effects of the coupling between multiple gap street vortices originating from the neighboring rods, a phenomenon referred to as the rod bundle vortex network. These large-scale vortical structure interactions spanning multiple planes play a crucial role in shaping the flow field within a rod bundle arrangement and enhancing the thermal-hydraulic properties, as evidenced by the temperature statistics. This finding implies that the interplay between subchannels is of significant importance and that a single subchannel domain may not adequately represent the true flow field characteristics of a rod bundle configuration.

5.6. Conclusion

This section aims to summarize the key inferences and complete the investigation of the sub-research question regarding which geometric representation most accurately captures the thermal-hydraulic properties of a rod bundle arrangement. The analysis indicates that the 2X2 subchannel configuration appears to better represent the rod bundle arrangement when compared to the square subchannel approach. This conclusion is drawn from the examination of the autocorrelation plots of velocity fluctuations, which reveal that in the 2X2 subchannel case, the centres of two adjacent subchannel domains exhibit negligible correlation, suggesting the presence of inter-subchannel interactions that are not captured within a single subchannel domain. The rod bundle vortex network plays a crucial role in the eddy-driven transport of thermal momentum, effectively enhancing the overall thermal mixing within the system.

These statements are corroborated by the previously presented comparisons of velocity and temperature statistics between the 2X2 subchannel and square subchannel configurations. The observed differences in the Reynolds stress tensor between the two geometries serve as evidence of the contrasting flow physics. However, these distinctions are not reflected in the Turbulent kinetic energy (TKE) budget terms, as they can be considered the cumulative effect of the normal stress components. The key differences are manifested in the covariance of the u and v velocity components. Notably, no significant disparities were detected in the first-order mean statistics for both velocity and temperature.

Having answered the sub-research question by establishing the 2X2 subchannel as the more representative geometry for capturing the thermal-hydraulic characteristics of a rod bundle arrangement, this configuration will be employed in the next phase of the study. The aim is to understand the differences in heat transfer and flow characteristics between the 2X2 subchannel and the conventional pipe configuration. This investigation will shed light on the adequacy of the existing design methodologies adopted for Pressurized Water Reactors (PWRs) and will potentially necessitate the development of novel Nusselt number (Nu) correlations specific to rod bundle geometries, as opposed to relying solely on the pipe-based correlations.

Comparative Study

This chapter presents a comprehensive comparative analysis of flow and thermal characteristics between conventional pipe and 2×2 subchannel configurations, critical for understanding thermal-hydraulic performance in nuclear reactor systems. The investigation encompasses a multifaceted examination of these geometries to elucidate their distinctive flow physics and heat transfer mechanisms.

The study focuses on a rigorous comparative framework that includes:

- Detailed velocity statistics and turbulent kinetic energy analysis
- Comprehensive temperature statistics and thermal transport characteristics
- Qualitative visualization of velocity vectors and temperature interactions
- Nusselt number correlation studies for varying Prandtl number regimes
- Exploration of geometric influences on heat transfer efficiency and flow dynamics

By conducting an in-depth comparative study across multiple analytical dimensions, this research aims to advance the understanding of thermal-hydraulic performance in different geometrical domains, with particular relevance to Pressurized Water Reactor (PWR) thermal systems design and optimization.

6.1. Comparison Approach

Since the geometry of the pipe and 2×2 subchannel configurations are evidently different, direct comparison of the statistics poses significant challenges. To address this, a novel approach is introduced, as no prior research has tackled this specific comparison methodology.

For the pipe, statistics are extracted from temporally and spatially averaged values along the radial direction (R), as shown in Figure 6.1. For the 2×2 subchannel configuration, the statistics are extracted along the largest wall-normal distance, denoted as L_3 , which passes through the bulk center. This distance also corresponds to the 45° line or one of the unit cell boundaries, as explained in previous sections. The comparative framework ensures a consistent basis for evaluating geometric influences on flow and heat transfer characteristics.

6.2. Higher Order Statistics

This section presents a comprehensive analysis of higher-order statistics to elucidate the distinctions in flow physics and thermal characteristics between the pipe and 2×2 subchannel configurations. The Nusselt number (Nu) correlation critically motivates the investigation, which plays a pivotal role in designing and optimizing Pressurized Water Reactor (PWR) thermal systems. Understanding the nuanced differences and similarities in velocity and temperature statistics becomes essential for comprehensive thermal-hydraulic modelling.

Both configurations were scaled to their respective characteristic lengths: the pipe case was normalized by radial distance (r/R), while the 2×2 subchannel configuration was scaled along the shortest distance from rod to bulk (along the 45° line) by the total length (d/L_3). This normalization ensures a comparative framework that accounts for geometric variations.

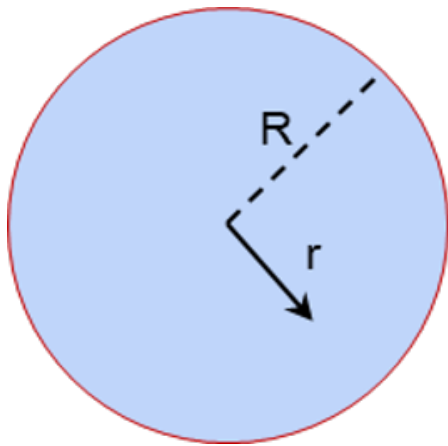


Figure 6.1: Radial distance (R) in the pipe configuration

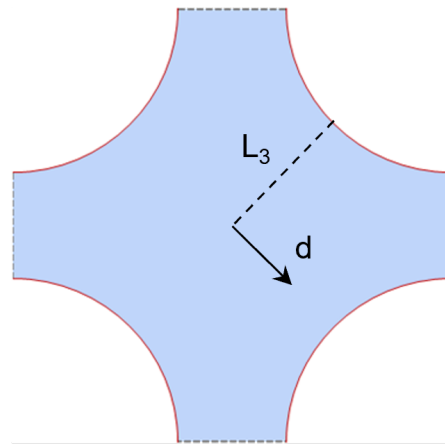


Figure 6.2: Wall-Normal Distance (L_3) in the single subchannel configuration

6.2.1. Velocity Statistics

Figure 6.3 presents a comparative analysis of normalized axial velocity (U_z^+) between pipe and 2×2 subchannel configurations. The velocity profile reveals subtle yet significant geometric influences. Notably, the subchannel 2×2 configuration demonstrates slightly reduced velocities compared to the pipe case. This variation can be attributed to complex flow characteristics inherent in subchannel domains, including secondary flows and intricate rod bundle network vortices discussed in previous investigations.

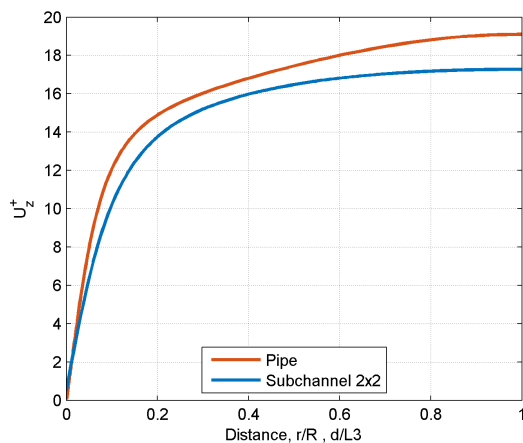


Figure 6.3: Normalized Axial Velocity Distribution Comparing Pipe and 2×2 Subchannel Flow Configurations

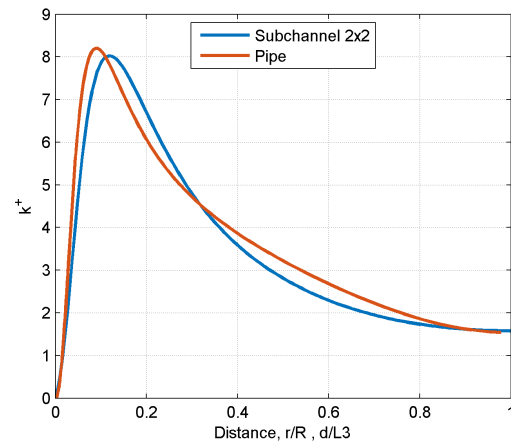


Figure 6.4: Turbulent Kinetic Energy Profiles Revealing Geometric Flow Variations

The turbulent kinetic energy (k^+), normalized by friction velocity (u_τ), reveals profound insights into the flow dynamics. In the subchannel 2×2 configuration, the kinetic energy peak exhibits distinctive characteristics: it shifts slightly away from the wall and demonstrates a marginally reduced intensity. This spatial shift indicates a modified turbulent energy production mechanism compared to the pipe configuration.

The pipe geometry, characterized by a more uniform boundary condition along its circular cross-section, promotes a consistent shear layer near the wall. Consequently, this results in higher turbulence production in the near-wall region, explaining the peak's proximity to the wall. The subchannel geometry, by contrast, experiences complex interactions such as gap street vortices and secondary flows that redistribute turbulent energy.

An intriguing observation is the slope of the k^+ curve post-peak. The subchannel configuration demonstrates

a steeper kinetic energy decay than the pipe. Despite these local variations, both configurations converge towards similar k^+ values in the central (bulk) region, indicating that core flow dynamics are predominantly governed by lower-intensity, quasi-isotropic turbulence.

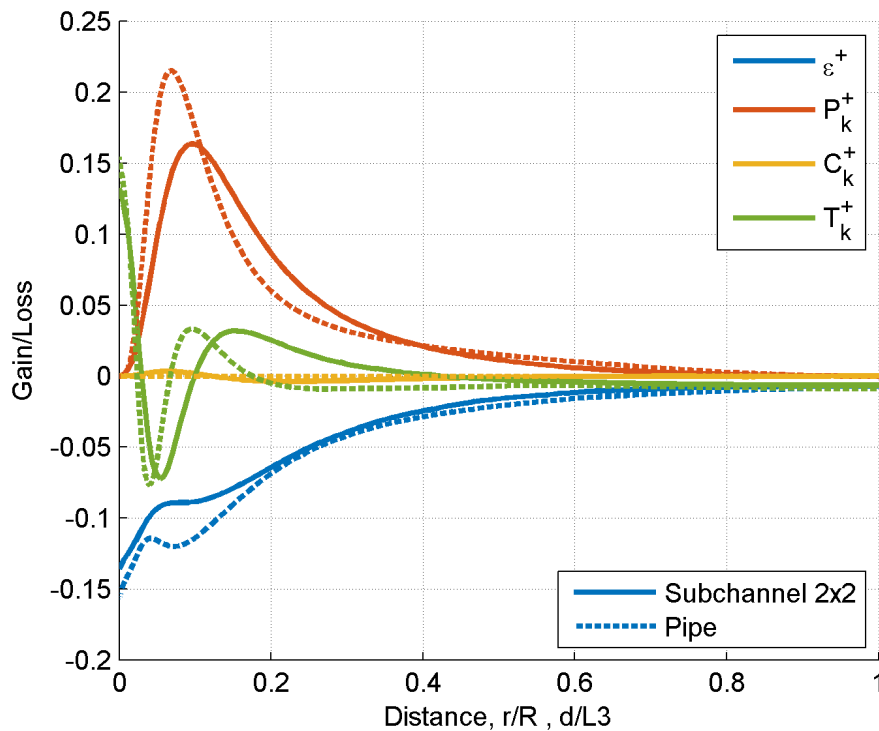


Figure 6.5: Comprehensive Turbulent Kinetic Energy Budget Analysis

Figure 6.5 provides a detailed examination of the Turbulent kinetic energy (TKE) budget terms, including production (P_k^+), dissipation (ϵ_k^+), convective term (C_k^+), and diffusion terms (T_k^+)—comprising pressure, viscous, and turbulent contributions.

For the subchannel 2×2 configuration, the production trend mirrors observations from previous kinetic energy analysis. The dissipation characteristics are particularly noteworthy: relatively lower in magnitude and positioned further from the wall compared to the pipe case. While the diffusion terms demonstrate similar peak values, their spatial distribution reveals subtle geometric influences.

6.2.2. Temperature Statistics

The first-order temperature statistics, represented in Figures 6.6 and 6.7, provide insights into mean thermal transport for Prandtl numbers (Pr) of 0.025 and 1.0, examining both isothermal (θ_1) and isoflux (θ_3) boundary conditions.

For $Pr = 0.025$, the temperature gradient exhibits a more relaxed profile, suggesting enhanced thermal mixing. This enhanced thermal transport could be attributed to the improved flow characteristics observed in velocity statistics. The isothermal condition (θ_1) demonstrates a particularly smooth temperature distribution, indicating efficient heat transfer mechanisms.

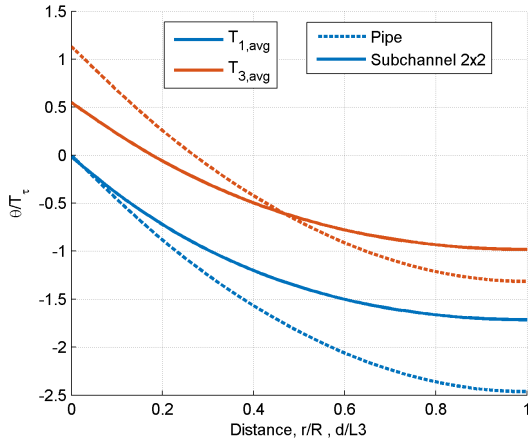


Figure 6.6: Mean Temperature Distribution for Low Prandtl Number Isothermal Condition

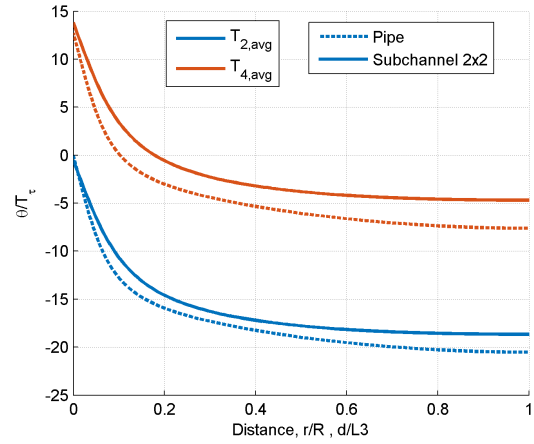


Figure 6.7: Mean Temperature Distribution for Unity Prandtl Number

For $Pr = 1.0$, the temperature statistics closely mirror the velocity profile characteristics. Notably, the subchannel 2×2 configuration exhibits lower excess temperature values compared to the pipe configuration for both rod wall boundary conditions. This observation implies enhanced thermal transport efficiency, even under conditions of matched momentum and thermal diffusivities.

The temperature fluctuation analysis, illustrated in Figures 6.8 and 6.9, reveals nuanced thermal mixing behaviors. For $Pr = 0.025$, the subchannel 2×2 configuration's $T_{1,rms}$ (representing the Dirichlet condition) demonstrates a smaller peak compared to the pipe case, corresponding to smoother and more uniform temperature distributions.

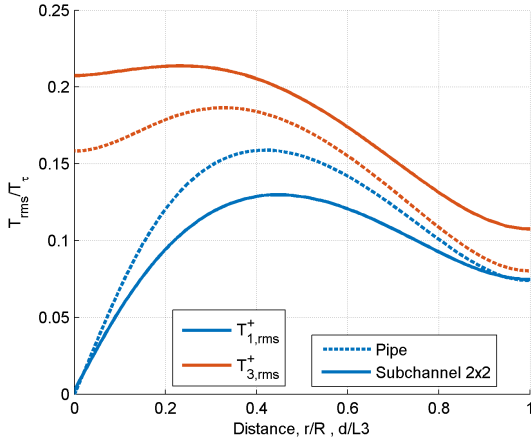


Figure 6.8: Temperature Fluctuation Intensity for Low Prandtl Number

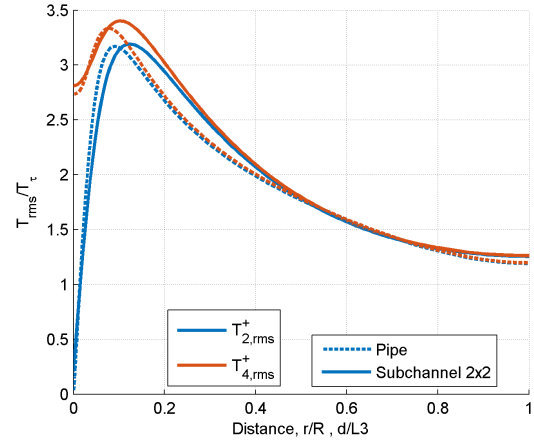


Figure 6.9: Temperature Fluctuation Intensity for Unity Prandtl Number

For $Pr = 1.0$, the temperature fluctuation trends closely follow the second-order velocity statistics. Although the peaks are slightly elevated compared to the pipe configuration, this indicates heightened thermal turbulence characteristic of the subchannel geometry.

The streamwise turbulent heat flux ($[w'T']$) comparison between pipe and subchannel 2×2 configurations, presented in Figures 6.10 and 6.11, further illuminates thermal transport mechanisms.

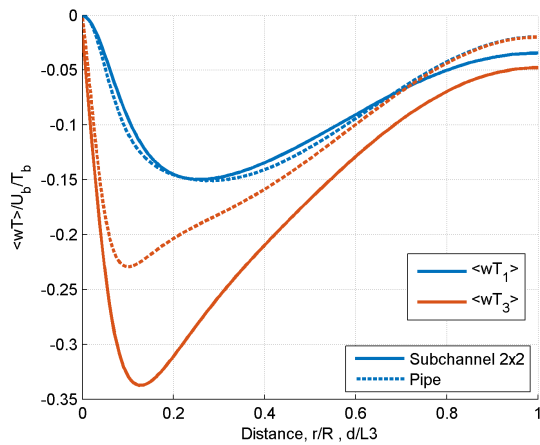


Figure 6.10: Streamwise Turbulent Heat Flux for Low Prandtl Number

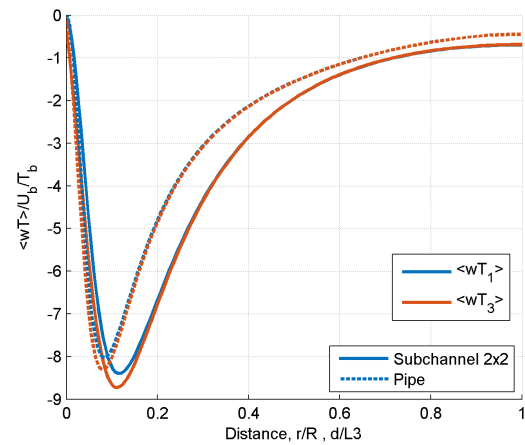


Figure 6.11: Streamwise Turbulent Heat Flux for Unity Prandtl Number

For $Pr = 0.025$, the Dirichlet condition ($w'T_1'$) reveals negligible differences between pipe and subchannel configurations. Conversely, the isoflux condition ($w'T_3'$) demonstrates enhanced turbulent energy production and heat transfer relative to the pipe configuration.

For $Pr = 1.0$, the trends closely align with velocity statistics. The subchannel 2×2 configuration exhibits a more pronounced negative peak, signifying increased turbulent thermal mixing compared to the pipe configuration.

Detailed temperature heat flux (THF) budget plots comparing pipe and 2x2 subchannel configurations, encompassing production, dissipation, convection, and turbulent diffusion terms, are presented in the Appendix (Figures A.9-A.12). These comprehensive figures enable a comparative analysis of thermal transport mechanisms between the two geometrical configurations.

6.3. Velocity vectors coloured by temperature

This section delves into the velocity vector representation of the pipe and 2x2 subchannel configuration. Understanding the qualitative behaviour of such turbulent structures and their role in heat transport is critical for designing and optimizing thermal systems; the statistics explored in earlier sections combined with the velocity vector aid in visualising the effects of thermal transport of momentum and heat from the boundary wall to the bulk flow.

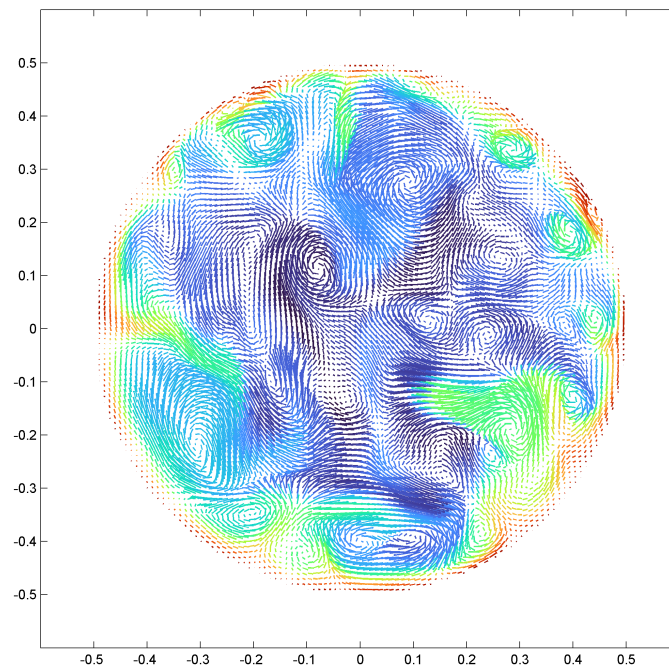


Figure 6.12: Instantaneous velocity vectors in pipe flow colored by temperature, illustrating turbulent heat transport.

Figure 6.12 showcases the represent the instantaneous velocity vectors, indicating both the direction and magnitude of the fluid's motion. The distribution of velocity vectors shows complex flow structures, including localized swirls and vortices, which are characteristic of turbulent flows in pipes. The colour of the vectors corresponds to the fluid temperature, transitioning from warmer tones (red/yellow) near the pipe walls to cooler tones (blue/green) towards the core of the pipe. The isothermal boundary condition ensures that the temperature at the wall is held constant, leading to the development of a steep thermal gradient in the near-wall region.

The swirling structures (vortices) visible in the plot illustrate how turbulent eddies act as a transport mechanism for heat. These vortices carry higher-temperature fluid near the walls into the bulk region, facilitating convective heat transfer across the cross-section. The plot highlights the instantaneous mixing effect of turbulent flows, where chaotic velocity fields enhance heat and momentum transport.

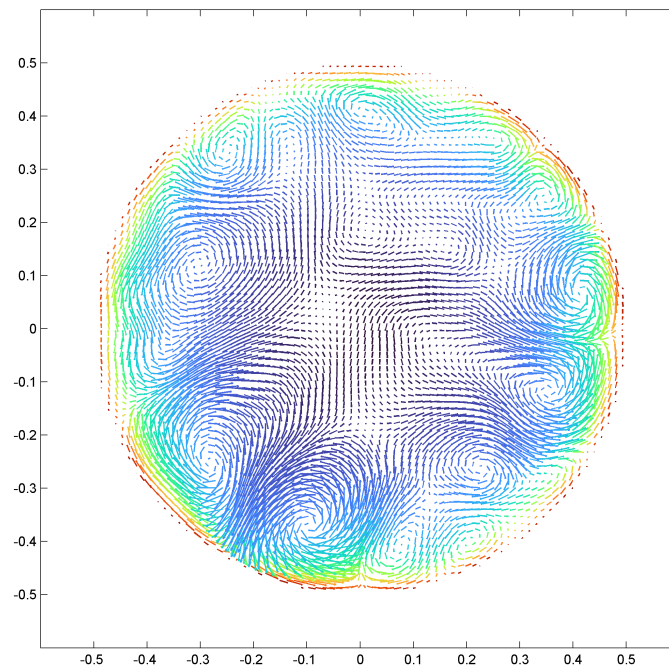


Figure 6.13: Averaged velocity vectors in pipe flow colored by temperature, illustrating turbulent heat transport.

Figure 6.13 showcases the time-averaged (space and time) velocity vector for pipe configuration. The arrows in the plot now represent time-averaged velocity vectors, providing insight into the dominant, large-scale flow patterns rather than instantaneous turbulence. The magnitude of the vectors diminishes closer to the pipe centre, suggesting reduced secondary motion in the bulk region when turbulent fluctuations are averaged out. The color coding of the vectors still represents the temperature distribution, transitioning from higher temperatures (red/yellow) near the walls to lower temperatures (blue/green) toward the pipe core. The averaged plot highlights a more uniform temperature field in the bulk region due to sustained turbulent mixing.

The average velocity vectors show how the bulk fluid motion works in conjunction with residual secondary flows to transport heat from the wall toward the pipe core, though less efficiently compared to the instantaneous case. The averaged flow reveals the dominant secondary flow structures, with residual vortices visible near the walls. These structures are weaker than in subchannel geometries, where geometric constraints amplify secondary flows and improve heat transport. The plot also emphasizes the slower rate of heat transport in the pipe core, where the absence of strong secondary vortices results in more uniform but less efficient mixing compared to the near-wall regions.

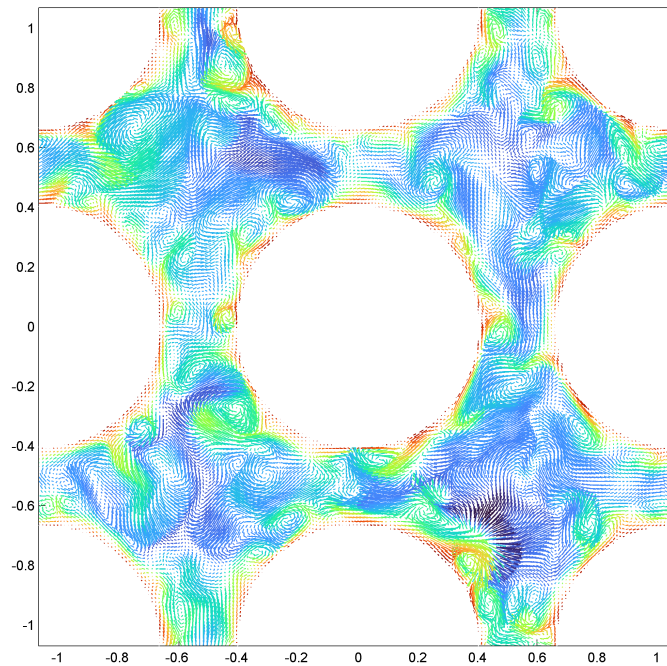


Figure 6.14: Instantaneous velocity vectors in 2x2 subchannel flow colored by temperature, illustrating turbulent heat transport.

Figure 6.14 showcases an instantaneous velocity vector flow field for a 2x2 subchannel for isothermal boundary condition ($Pr = 1$). Instantaneous velocity vectors reveal a turbulent flow characterized by localized vortices and swirling patterns distributed across the cross-section. These structures are essential for convective heat transport, actively carrying high-temperature fluid away from the walls and distributing it toward the bulk flow. The colour-coded temperature variation indicates the efficiency of this transport, as regions near the walls exhibit steep thermal gradients, while the core region shows relatively uniform mixing.

The rod wall and bulk interaction enhance secondary flows in the subchannel domain. These flows are particularly prominent in the intersections of adjacent subchannels, where they interact to form organized vortex structures. The swirling eddies seen in the figure exemplify how turbulent flow enhances mixing by breaking down large-scale structures into smaller scales, thereby increasing heat transfer efficiency. These structures are especially effective in redistributing thermal energy from high-temperature regions near the walls into the cooler bulk. The secondary flows in subchannels are stronger and more efficient compared to pipe geometries, where the lack of geometric constraints results in weaker secondary vortices and slower mixing.

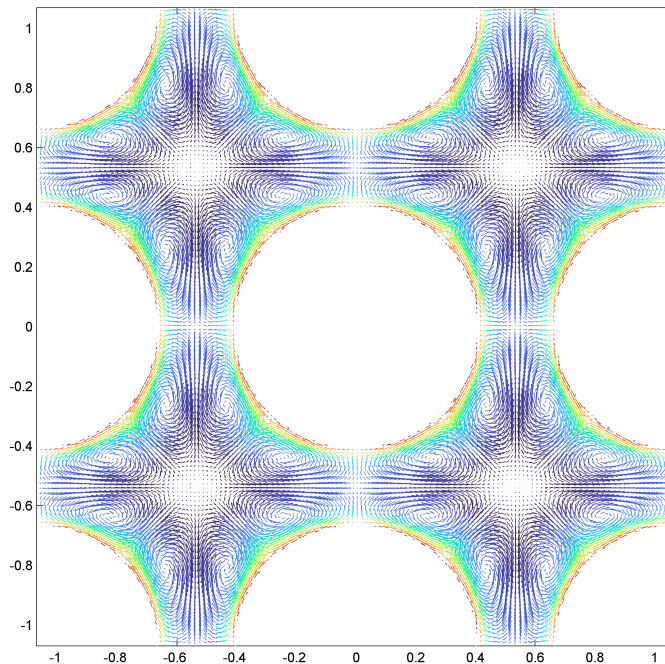


Figure 6.15: Averaged velocity vectors in 2x2 subchannel flow colored by temperature, illustrating turbulent heat transport.

Figure 6.15 showcases the time-averaged (space and time) velocity vector for the 2x2 subchannel configuration. Compared to the instantaneous velocity field, the averaged field reveals the dominant, large-scale flow patterns while suppressing smaller turbulent fluctuations. The vectors show a clear organization of secondary flows in the subchannel domain, forming symmetrical vortices in each unit cell. The colour gradient in the plot demonstrates the efficiency of mixing. The high-temperature fluid near the walls is transported inward by the secondary vortices, while cooler bulk fluid is directed toward the walls.

The time- and space-averaged velocity field in pipe geometries shows weaker and less uniform secondary flows, resulting in lower heat transfer efficiency. Conversely, subchannels leverage their geometry to sustain strong, organized secondary flows that facilitate better mixing and heat transport. With the combination of gap street vortex, the coupling of these gap street vortices and secondary flows significantly reduces thermal gradients across the domain, resulting in a more uniform temperature distribution than the pipe configuration.

While both configurations exhibit the turbulent mechanisms necessary for heat transport, the subchannel geometry is qualitatively and quantitatively better for thermal-hydraulic applications. The combination of instantaneous turbulent structures and sustained secondary vortices in subchannels results in faster and more uniform thermal mixing, making it a preferred choice over pipes for systems requiring enhanced heat transfer and hydraulic performance.

6.4. Nusselts number

This investigation scrutinizes the Nusselt number (Nu) characteristics of two distinct geometrical configurations: a conventional circular pipe and a representative 2x2 subchannel arrangement, characteristic of Pressurized Water Reactor (PWR) fuel assemblies. Building upon the comprehensive flow physics and heat transfer analysis presented in preceding sections, this research evaluates the thermal-hydraulic performance across two distinct Prandtl number regimes: $Pr = 1$ and $Pr = 0.025$. By conducting a comparative analysis, the study aims to elucidate the inherent limitations of existing heat transfer correlations derived from idealized geometrical representations and underscore the critical necessity for geometry-specific Nusselt number correlations in nuclear thermal-hydraulic design.

Key observations for $Pr = 1$ (Water at PWR Conditions) presented in Figure 6.16 are:

1. **Subchannel 2x2 vs Pipe Configuration:** The subchannel 2x2 configuration shows higher Nusselt numbers ~ 25.8 than the pipe configuration ~ 23.2 for the same Reynolds number ($Re_b = 5300$). The relative increase in Nusselt number is approximately 11.5%, not a large difference given the low Reynolds number.

A higher Nusselt number indicates enhanced convective heat transfer efficiency. The subchannel 2x2 configuration facilitates greater mixing or turbulence in the flow, reducing thermal resistance and enhancing heat transfer compared to the pipe configuration. This is likely due to differences in geometry influencing flow patterns, turbulence levels, and thermal boundary layer development, as observed in earlier sections.

2. **Boundary Conditions - Isothermal vs Isoflux:** Both isothermal and isoflux conditions produce nearly identical Nusselt numbers for each configuration, with a slight difference in the subchannel 2x2. This indicates that the overall heat transfer is not highly sensitive to these boundary condition variations under the given conditions, demonstrating robust thermal performance, which is also observed in the previous chapter for pipe configuration.

This similarity arises because both boundary conditions achieve similar average heat transfer characteristics, which dominate at these Re and Pr values.

3. **Comparison with Correlations:** The Nusselt number for subchannel 2x2 configurations lies slightly above the Dittus-Boelter correlation, which is also observed in the pipe configuration. This suggests the subchannel's heat transfer performance exceeds these classical correlations' expectations.

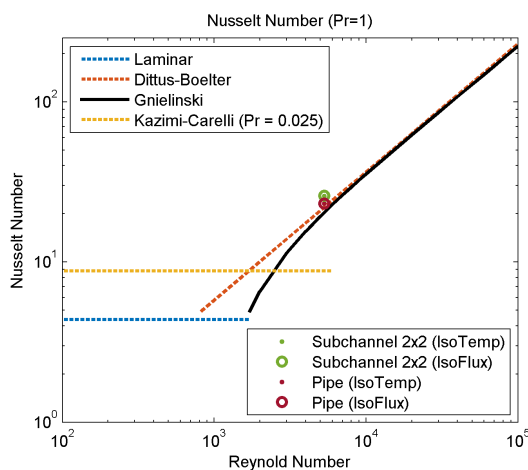


Figure 6.16: Nusselt number (Nu) for Prandtl number $Pr = 1$ compared with Reynolds number (Re) between pipe and 2x2 subchannel cases.

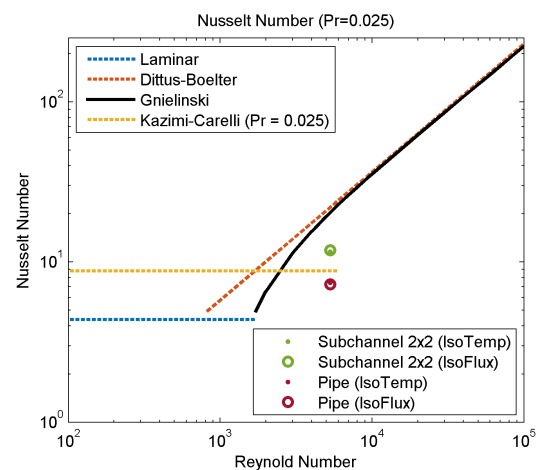


Figure 6.17: Nusselt number (Nu) for Prandtl number $Pr = 0.025$ compared with Reynolds number (Re) between pipe and 2x2 subchannel cases.

Key Observations for $Pr = 0.025$ (Liquid metal at PWR Conditions) presented in Figure 6.17 are:

1. **Subchannel 2x2 vs Pipe Configuration:** The subchannel 2x2 yields a mean Nusselt number (~ 11.7). In contrast, the pipe configuration results in lower Nusselt numbers (~ 7.43). The relative increase in the Nusselt number is approximately 59.7%, a more pronounced difference compared to $Pr=1$ (11.5%).

Subchannel 2x2 provides significantly enhanced heat transfer compared to the pipe configuration, with the difference amplified at lower Pr . This phenomenon is particularly relevant for liquid metals, where high thermal conductivity and low Pr rely more on convection over conduction, heavily influenced by flow geometry.

The slight differences between isothermal and isoflux conditions are more pronounced than those observed for $Pr=1$.

At $Pr=0.025$, thermal diffusivity dominates over momentum diffusivity, rendering heat transfer more dependent on the thermal boundary layer's interaction with the flow. Boundary condition changes (isothermal vs. isoflux) significantly affect the temperature gradient, leading to increased sensitivity.

2. **Comparison with Correlations:**

For the 2x2 subchannel configuration, Nusselt values lie slightly above the Kazimi-Carelli correlation (specific to $Pr=0.025$) but below Dittus-Boelter and Gnielinski, which are traditionally calibrated for higher Pr . This suggests the subchannel performs slightly better than expected based on Kazimi-Carelli but aligns with the physics of lower Pr .

For the pipe configuration, Nusselt numbers are significantly below all three correlations, indicating that standard models underpredict thermal transport for pipe flow at $Pr=0.025$.

The discrepancies observed between subchannel and pipe configurations at varying Prandtl numbers underscore a critical limitation in existing Nusselt number correlations. The study reveal that:

- **Geometric Dependency:** Conventional correlations derived from simplified pipe geometries fail to capture the nuanced heat transfer mechanisms in complex subchannel configurations, particularly at low Prandtl numbers.
- **Correlation Inadequacy:** Existing empirical models systematically underpredict thermal transport, highlighting the urgent need for geometry-specific correlation development.
- **Prandtl Number Sensitivity:** The pronounced differences in Nusselt numbers across Pr ranges demand a more sophisticated approach to thermal-hydraulic modelling, especially for applications involving liquid metals or low- Pr fluids.

Conclusion and Future Scope

This chapter synthesizes the key findings from our comprehensive investigation of thermal-hydraulic characteristics in pipe and subchannel configurations. By examining flow dynamics, heat transfer mechanisms, and Nusselt number correlations across different geometries and Prandtl numbers, the study provides critical insights into the complex thermal transport phenomena in nuclear reactor systems. The conclusion reflects on the research outcomes, highlighting the limitations of existing correlations and proposing pathways for future research in thermal-hydraulic modeling.

7.1. Conclusion

A numerical study of subchannel with comparison to the conventional pipe configuration, using DNS, was conducted to evaluate the boundary conditions as well as the thermal-hydraulic properties. The pipe configuration was conducted for a Reynolds number of 5300 and was validated using reference data (El Khoury). Flow characteristics and heat transfer characteristics were evaluated and validated. The Nusselt number for the 4 temperature scalars was plotted against the Reynolds number, and it was observed that the Nusselt number is more sensitive to lower Prandtl numbers, even though the difference is negligible. Newer empirical correlations are required to model for lower Prandtl numbers.

Subchannel configurations consisted of 2 geometric configurations: a square subchannel and a 2x2 subchannel. The subchannel configurations was conducted for a Reynolds number of 5300. The square subchannel domain represented the heat transfer characteristics around a single rod, while the 2x2 subchannel domain extended the single interior subchannel to a composite of four single subchannels, representing the flow around the rod as well as the partial effects of the neighbouring rods. Both geometries were considered to understand which one accurately represented the rod bundle. The study revealed that the heat transfer characteristics in a 2x2 subchannel is a better representation of the rod bundle domain. This was elucidated through the autocorrelation plots, which were taken from the subchannel centre to the subchannel centre to compare with the autocorrelation of a square subchannel along the boundary. It was inferred that the square subchannel was not able to capture the coupling of the gap street vortex, also referred to as the rod bundle vortex network, as showcased in the difference in Reynolds stress between both geometric configurations.

The subchannel 2x2 was selected and evaluated side by side with the pipe configuration to understand the difference in heat transfer characteristics. Due to the complex geometry of the subchannel domain, the anticipated flow physics in the domain was better than the pipe configuration in terms of thermal-hydraulic mixing. The Nusselt number was evaluated for the subchannel domain with a comparison to the pipe configuration, and it was observed that for a unity Prandtl number, there was a minimal difference between both geometries, while the difference was more significant for a low Prandtl number ($Pr = 0.025$).

This study answers the initially proposed research question and sub-research questions. The effects of the rod bundle vortex network proved to be of greater importance, and the larger computational domain proved to capture the neighbouring rods' combined flow and heat transfer characteristics observed in a rod bundle arrangement. The study also addresses the main research question and research objective of the necessity for empirical Nusselt number correlations specific to subchannel geometry, and the conventional approach of using pipe geometry is deemed to be outdated and over-predicting. Although the difference is

negligible at low Reynolds numbers (10^4), this is not the case for a PWR, where Reynolds numbers range between 10^5 and 10^6 .

7.2. Recommendations

- **Improved Averaging Techniques:** This study has focused solely on averaging along the unit cell boundary (one-dimensional). While this approach has provided valuable insights into the Reynolds stress and other statistics, extending the averaging to include the interior of the unit cell (a second dimension) would offer a more comprehensive understanding of flow physics and heat transport. Such an approach can help capture the spatial variations and intricate flow behaviors within the subchannels. Additionally, exploring alternative averaging techniques, comparing them with those used in this study, and validating their outcomes can further refine the accuracy of statistical analyses and improve our interpretation of the results.
- **Expanded Domain Sizes:** Investigating larger domains such as 3×3 and 4×4 subchannel configurations can help better represent the rod bundle geometry and capture the coupling effects of gap street vortices (rod bundle vortex networks). These extended configurations allow for a more realistic depiction of the interaction between adjacent subchannels, potentially leading to more accurate conclusions regarding flow dynamics and thermal performance in rod bundles.
- **Analysis of 2×1 and 1×1 Subchannel Configurations:** The 2×1 subchannel configuration serves as a valuable intermediate step, isolating (to some extent) the coupling of gap street vortices and focusing on flow dynamics across a single gap. This can provide key insights into the behavior of gap vortex streets between adjacent subchannels. Additionally, analyzing the interior 1×1 subchannel can help establish a baseline comparison with the square subchannel configuration. While these configurations should ideally show similar results, subtle variations in certain statistics, such as autocorrelation, could highlight unique aspects of flow dynamics, provided these statistics are implemented appropriately.

7.3. Future Scope

- **Variation in Prandtl Numbers:** This study has been limited to low Prandtl numbers and unity Prandtl number (representing water). Extending the investigation to higher Prandtl numbers ($Pr > 1$) is critical, as the effects on flow physics and heat transfer can vary drastically. Fluids with higher Prandtl numbers exhibit different thermal diffusivities, which influence boundary layer behavior and heat transfer characteristics significantly.
- **Higher Reynolds Numbers:** The bulk Reynolds number in Pressurized Water Reactors (PWRs) typically ranges in the millions. Due to computational constraints, this study was limited to a Reynolds number of 5300. Future studies should explore higher Reynolds numbers, such as 11,000 and 50,000, to understand their impact on flow instabilities, turbulence, and heat transfer efficiency. Higher Reynolds numbers are expected to play a significant role in improving thermal performance and enhancing design optimization.
- **Alternative Rod Bundle Configurations:** The commonly used rod bundle arrangement in PWRs is square; however, liquid metal reactors often utilize hexagonal configurations. Exploring alternative geometries, such as hexagonal and circular arrangements, is essential to understand the completely different flow physics in these configurations compared to square bundles. This exploration can provide insights into their unique turbulence structures and heat transfer behaviors, helping design fuel assemblies tailored to specific reactor applications.
- **Wall Effects and Corner Subchannels:** This study did not consider the effects of walls or corners in the rod bundle geometry. Investigating these aspects in future studies would complete the understanding of flow physics in square configurations. Wall effects, in particular, can significantly influence flow distribution, secondary flows, and heat transfer, especially near the peripheral rods.
- **Integration of Advanced Effects:** To achieve a more realistic simulation of reactor conditions, future studies should implement fluid-structure interaction (FSI) and surface roughness in subchannel domains. These factors are critical for assessing flow-induced vibrations, structural stresses, and their influence on turbulence and heat transfer. The inclusion of these effects would enable the design of optimized PWR fuel assemblies with enhanced safety and efficiency.

References

- [1] Wikipedia Contributors. *Pressurized Water Reactor*. Accessed: 2024-12-15. 2024. URL: https://en.wikipedia.org/wiki/Pressurized_water_reactor.
- [2] IAEA Nuclear statistics. URL: <https://pris.iaea.org/PRIS/WorldStatistics/OperationalReactorsByType.aspx>.
- [3] NCE Nuclear statistics. URL: <https://wna.origindigital.co/images/articles/performance-report-2023-final.pdf>.
- [4] World Nuclear Association. *Global Nuclear Industry Performance Report*. Accessed: 2024-11-05. World Nuclear Association. 2024. URL: <https://world-nuclear.org/our-association/publications/world-nuclear-performance-report/global-nuclear-industry-performance>.
- [5] Ronald A. Knief. "Nuclear Power Reactors". In: *Encyclopedia of Physical Science and Technology*. Ed. by Editor Name. Third Edition. Accessed: 2024-11-05. Albuquerque, New Mexico, USA: Academic Press, 2003, pp. 739–761. DOI: 10.1016/B0-12-227410-5/00495-6.
- [6] S. Gurunath. "Numerical Investigations of Coherent Structures in Axial Flow in Single Rod-Channel Geometry". Available at: <https://resolver.tudelft.nl/uuid:b7877dd3-3b11-4016-914f-488feec88bfc>. Master's thesis. Delft, The Netherlands: Delft University of Technology, 2012.
- [7] S. Wong et al. *Analysis of the FLECHT SEASET Unblocked Bundle Steam Cooling and Boiloff Tests*. Tech. rep. NUREG/CR-1533, EPRI NP-1460, WCAP-9729. Westinghouse Electric Corporation, Jan. 1981. URL: <https://www.nrc.gov/docs/ML0707/ML070750048.pdf>.
- [8] J. Nikuradse. "Untersuchung über die Geschwindigkeitsverteilung in turbulenten Strömungen". In: *V.D.I. Forschungsheft 70* (1926), pp. 1229–1230.
- [9] L. Prandtl. "Über die ausgebildete Turbulenz". In: *Proceedings of the 2nd International Congress for Technical Mechanics*. Zurich, Switzerland, 1926.
- [10] L. C. Hoagland. "Fully Developed Turbulent Flow in Straight Rectangular Ducts — Secondary Flow, Its Cause and Effect on the Primary Flow". PhD thesis. Massachusetts Institute of Technology, Department of Mechanical Engineering, 1960.
- [11] A. Einstein. "Ursache der Meanderbildung der Flussläufe und des sogenannten Baerschen Gesetzes". In: *Die Naturwissenschaften* 14.11 (1926), pp. 223–224.
- [12] Nikolay Nikitin. "Secondary Flows of Prandtl's Second Kind: Mechanism of Formation and Methods of Prediction". In: *Theoretical and Applied Mechanics* 50.2 (2023), pp. 145–157. DOI: 10.2298/TAM231005008N.
- [13] Pijush K. Kundu et al. *Fluid Mechanics*. 6th. Academic Press, 2016. Chap. 11 - Instability.
- [14] Stavros Tavoularis. "Rod bundle vortex networks, gap vortex streets, and gap instability: A nomenclature and some comments on available methodologies". In: *Nuclear Engineering and Design* 241 (2011), pp. 2624–2626.
- [15] A. Mathur et al. "Direct numerical simulation of flow and heat transport in a closely-spaced bare rod bundle". In: *International Journal of Heat and Mass Transfer* 211 (Sept. 2023), p. 124226.
- [16] L. Meyer. "A review of large-scale structures in rod bundle flows". In: *Nuclear Engineering and Design* 240 (2010), pp. 1575–1585.
- [17] A. Gosset et al. "Laminar flow instability in a rectangular channel with a cylindrical rod". In: *Journal of Fluid Mechanics* 530 (2006), pp. 291–324.

- [18] E. Merzari et al. "Numerical simulation of flows in tight-lattice fuel bundles". In: *Nuclear Engineering and Design* 238 (2008), pp. 1703–1719.
- [19] E. Piot et al. "Gap instability of laminar flows in eccentric annular channels". In: *Nuclear Engineering and Design* 241 (2011), pp. 4615–4620.
- [20] J.J. Derksen. "Flow-induced forces in sphere arrays". In: *Journal of Fluid Mechanics* 657 (2010), pp. 1–34.
- [21] L. Meyer et al. "Large-scale turbulence structures in compound rectangular channels". In: *Experimental Thermal and Fluid Science* 29 (2005), pp. 947–956.
- [22] F. Baratto. "Subchannel Analysis of Rod Bundle Flows: Numerical and Experimental Studies". In: *Nuclear Technology* 154 (2006), pp. 83–97.
- [23] D. Chang et al. "Numerical simulation of turbulent flow in a 37-rod bundle". In: *Nuclear Engineering and Design* 241 (2011), pp. 4152–4166.
- [24] S. Tavoularis. "Rod bundle vortex networks, gap vortex streets, and gap instability: A nomenclature". In: *Nuclear Engineering and Design* 241 (2011), pp. 2338–2342.
- [25] J. De Ridder. "Fluid-elastic instability in heat exchanger tube bundles: A numerical analysis". PhD thesis. Ghent University, 2015.
- [26] SimScale Blog. *Understanding Turbulence in CFD Analysis*. Accessed: 2024-12-15. 2024. URL: <https://www.simscale.com/blog/turbulence-cfd-analysis/>.
- [27] Embry-Riddle Aeronautical University. *Turbulent Flows*. Accessed: 2024-12-15. 2024. URL: <https://eaglepubs.erau.edu/introductiontoaerospaceflightvehicles/chapter/turbulent-flows/>.
- [28] Stephen B. Pope. *Turbulent Flows*. Cambridge: Cambridge University Press, 2000.
- [29] BL Smith et al. "Report of the OECD/NEA KAERI rod bundle CFD benchmark exercise". In: *Paris, France: NEA/CSNI (2013) 5* (2013).
- [30] "LES analysis of the flow in a simplified PWR assembly with mixing grid". In: *Progress in Nuclear Energy* 75 (2014), pp. 15–24. DOI: <https://doi.org/10.1016/j.pnucene.2014.03.014>.
- [31] K. Podila et al. "A CFD simulation of 5 × 5 rod bundles with split-type spacers". In: *Progress in Nuclear Energy* 70 (2014), pp. 167–175. DOI: <https://doi.org/10.1016/j.pnucene.2013.08.012>.
- [32] Blaž Mikuž et al. "URANS prediction of flow fluctuations in rod bundle with split-type spacer grid". In: *International Journal of Heat and Fluid Flow* 64 (2017), pp. 10–22. DOI: <https://doi.org/10.1016/j.ijheatfluidflow.2017.01.008>.
- [33] Djamel Lakehal. "Highly-resolved LES of turbulent convective flow along a PWR rod bundle". In: *International Journal of Heat and Mass Transfer* 122 (2018), pp. 785–794. DOI: <https://doi.org/10.1016/j.ijheatmasstransfer.2018.01.099>.
- [34] Argonne National Laboratory. *NEK5000 Version X.Y*. Available: <https://nek5000.mcs.anl.gov>. Release date.
- [35] C. Chin et al. "The influence of pipe length in direct numerical simulation". In: *17th Australasian Fluid Mechanics Conference*. Department of Mechanical Engineering, University of Melbourne, Department of Mechanical, and Aerospace Engineering, Monash University. Auckland, New Zealand, 2010.
- [36] A. V. Nero Jr. *A Guidebook to Nuclear Reactors*. Berkeley, CA: University of California Press, 1979.
- [37] George K. El Khoury et al. "Direct Numerical Simulation of Turbulent Pipe Flow at Moderately High Reynolds Numbers". In: *Flow, Turbulence and Combustion* 91.3 (2013), pp. 475–495. DOI: [10.1007/s10494-013-9482-8](https://doi.org/10.1007/s10494-013-9482-8).
- [38] H. Ninokata et al. "Analysis of low Reynolds number turbulent flow phenomena in nuclear fuel pin subassemblies of tight lattice configuration". In: *Nuclear Engineering and Design* 239 (2009), pp. 945–953.



Appendix A

A.1. Pipe THF Budget terms

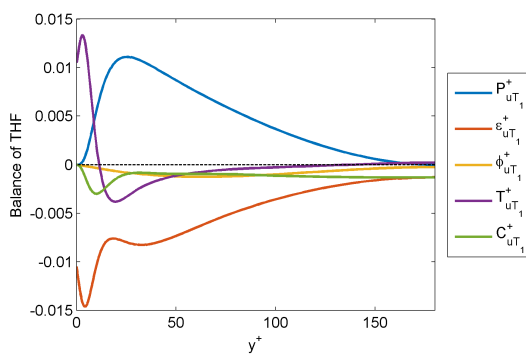


Figure A.1: THF Budget terms for scalar Temperature T_1 at 60 FTT plotted against wall distance (y^+).

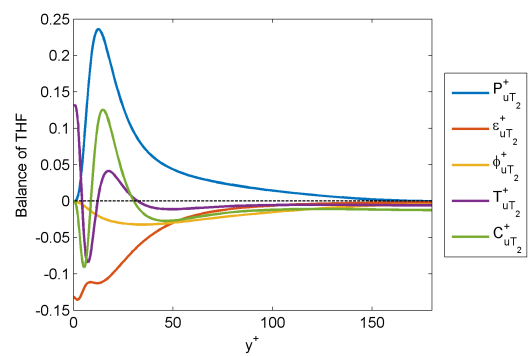


Figure A.2: THF Budget terms for scalar Temperature T_2 at 60 FTT plotted against wall distance (y^+).

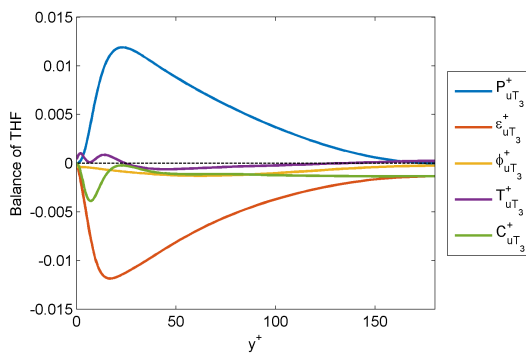


Figure A.3: THF Budget terms for scalar Temperature T_3 at 60 FTT plotted against wall distance (y^+).

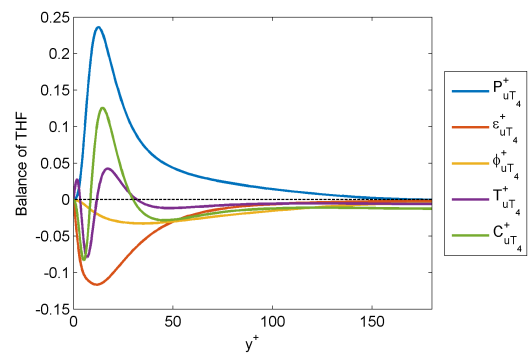


Figure A.4: THF Budget terms for scalar Temperature T_4 at 60 FTT plotted against wall distance (y^+).

A.2. Subchannel: Comparison of its THF budget

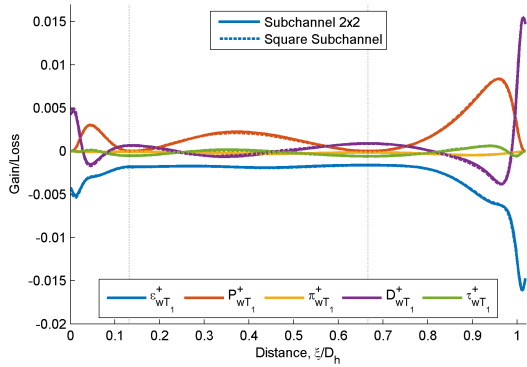


Figure A.5: Thermal Heat Flux (THF) budget for scalar temperature T_1 , comparing square and 2x2 subchannel cases, plotted against distance.

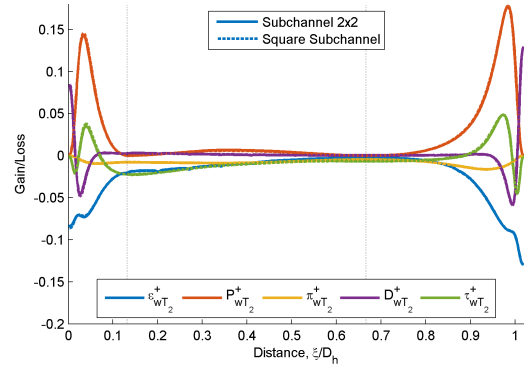


Figure A.6: Thermal Heat Flux (THF) budget for scalar temperature T_2 , comparing square and 2x2 subchannel cases, plotted against distance.

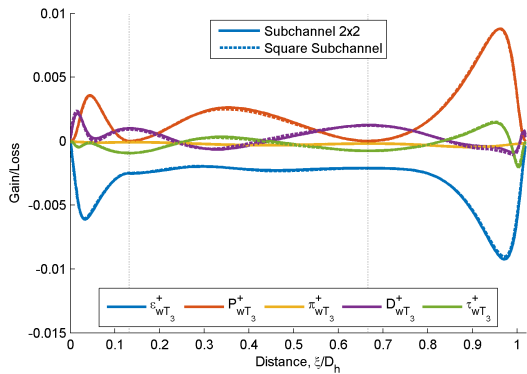


Figure A.7: Thermal Heat Flux (THF) budget for scalar temperature T_3 , comparing square and 2x2 subchannel cases, plotted against distance.

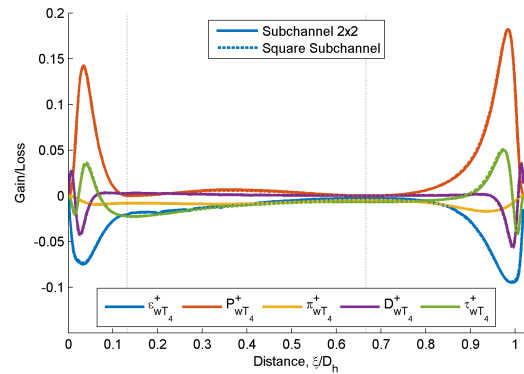


Figure A.8: Thermal Heat Flux (THF) budget for scalar temperature T_4 , comparing square and 2x2 subchannel cases, plotted against distance.

A.3. Comparative study: Pipe and 2x2 Subchannel

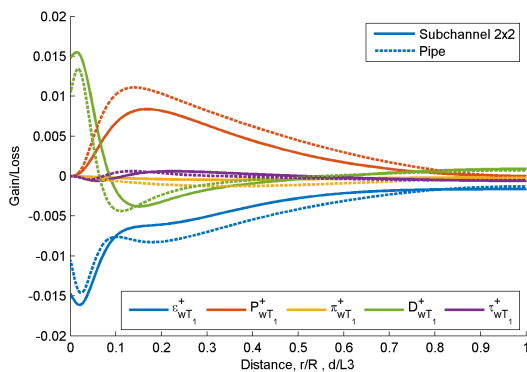


Figure A.9: Thermal Heat Flux (THF) budget for scalar temperature T_1 , comparing pipe and 2x2 subchannel cases, plotted against distance.

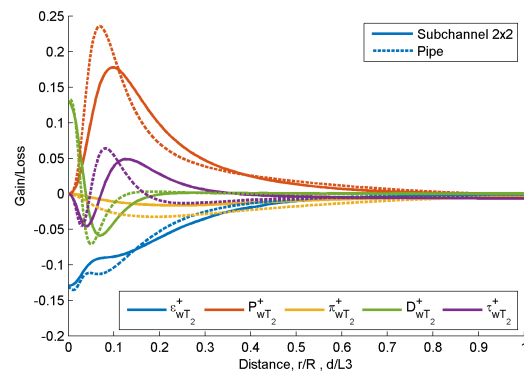


Figure A.10: THF budget for scalar temperature T_2 , comparing pipe and 2x2 subchannel cases, plotted against distance.

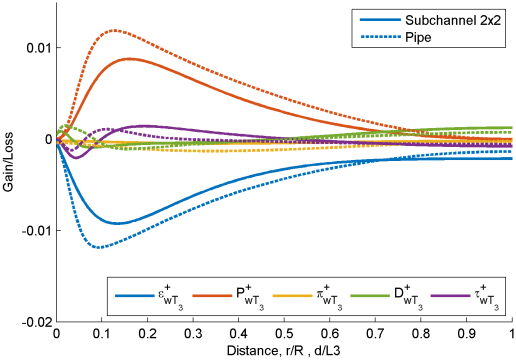


Figure A.11: Thermal Heat Flux (THF) budget for scalar temperature T_3 , comparing pipe and 2x2 subchannel cases, plotted against distance.

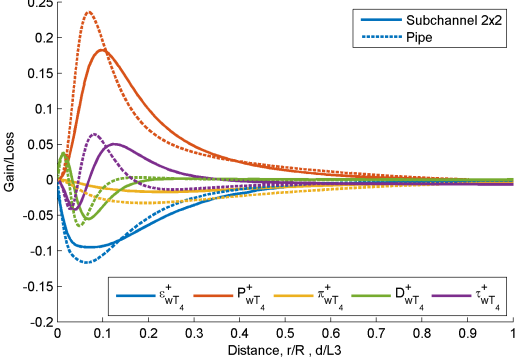


Figure A.12: THF budget for scalar temperature T_4 , comparing pipe and 2x2 subchannel cases, plotted against distance.